NTNU
Norwegian University of
Science and Technology

# Uncertainty modelling of pore pressure by using Monte-Carlo approach in the Hammerfest Basin, Barents Sea

Ravana Karimova

Petroleum Geosciences
Submission date: June 2017
Supervisor: Stephen John Lippard, IGP
Co-supervisor: Ane Ane Elisabet Lothe, SINTEF Petroleum Research
Arnt Grøver, SINTEF Petroleum Research

Norwegian University of Science and Technology
Department of Geoscience and Petroleum

# Preface

This thesis is submitted for the partial fulfilment of a Master Degree (MSc) in petroleum Geosciences, specializing in Petroleum Geology during the spring semester of 2017 at the Norwegian University of Science and Technology. It mainly addresses the overpressure and leakage history of the Hammerfest Basin, Barents Sea.

Trondheim, 19 June 2016

Ravana Karimova

# Acknowledgement

*First, I thank God for giving me the ability to finish this work.*

I first want to express my deep appreciation to the Department of Geoscience and Petroleum, at NTNU. I have been given a life-changing opportunity. This research is highly motivated and supported by my supervisors Ane Lothe and Arnt Grøver from SINTEF and Professor Stephen Lippard from Norwegian University of Science and Technology (NTNU) for valuable discussions and feedback. Their continued involvement maintained throughout the whole semester.

My profound gratitude to SINTEF research organization for giving me opportunity to work with them collaboratively and providing me with all the relevant technical support and an office for implementing the tasks of the project.

My study was funded by the Norwegian Quota Program, I am grateful to Lånekassen for giving me such an invaluable opportunity to study my master degree at the NTNU.

Finally, I wish to thank my parents and brother for their support and encouragement throughout my study at the university. Special thanks to my mother for being the best motivator during my stay in Norway.

I also appreciate the collaboration with my study mates during the past two years and I thank my best friends Veronica Torres and Radmila Mandzhieva for their support in my stressful times. It was a great pleasure to be around them.

# Abstract

Hammerfest Basin in the western Barents Sea, offshore Norway is a well-known oil and gas province which has been influenced by uplift and erosion events during the Cenozoic time. It is assumed that these events has led to pressure build up, induced cap rock failure and leakage. Uncertainty in timing and magnitude of these erosion events has led to an increase in exploration risks reflected by the relatively high number of dry exploration wells. The aim of this work is to evaluate the role of the minimum horizontal stress, seal permeability, erosion magnitude and burial history on the overpressure and leakage history of the basin, identify the possible leakage zones.

The water fluid pressure modelling is carried out using a basin software tool named Pressim that models pressure generation and dissipation over geological time scale. Interpreted fault traces are used to compartmentalize surface map of the reservoir Jurassic Stø Formation in order to model the dynamic overpressure history within the Hammerfest Basin. The failure criteria used for the leakage of the seal formation is a Mohr-Coulomb and friction sliding criteria. Quality check has been done by calibrating the simulated overpressure and measured overpressure in wells from the study area. The input model for minimum horizontal stress is calibrated with measured Leak-Off-Tests from wells in the basin.

The results of this study suggest that: 1) The present Hammerfest Basin is neither affected by large amount of overpressure, nor there is an ongoing leakage detected, 2) the present overpressure distribution in the basin can be modelled with low deviation 2) overpressure history expands from late Jurassic until present day 3) the timing and location of hydraulic leakage are modelled.

The number of leaking compartment increases as the magnitude of the simulated minimum horizontal stress decreases. Variation of shale permeability is affecting the leakage by making the overlying shale formation either too tight causing the hydraulic leakage, or too open causing the early release of the generated overpressure. Slight difference in the magnitude of the two different tested erosion maps lead to the large difference in the simulation results. Variation in burial history has an immense influence on the timing of the leakage for the compartments, where net erosion from Henriksen et al. (2011), gave the lowest deviation from measured pressure (+/- 5 bar). The Monte Carlo approach showed that the Grauls number should be <1.14.

# Contents

# Table of Figures

# Table of Tables

# 1. Introduction

Understanding the variations in subsurface pressure is important for many parts of oil and gas operations. In exploration, it is very important to have a good understanding of the possible overpressures that may occur in the reservoir or in the overburden. The pressure magnitude and distribution will have effect on possible top seal failure and leakages over geological time scale. This impact is related to the preservation of petroleum reserves in traps as well as their timing and direction which are all influenced by pressure (Borge,2002). For drilling campaign, it has a critical importance to know the subsurface pressure in order to maintain the pressure equilibrium with drilling fluid, avoid kicks or blowout, and secure safe drilling processes. But there is a less known impact of pressure on prospect appraisal than the problem it may cause for safety and well design (Giles et al., 1998). In this master thesis, the focus will be to fully understand how pressure distribution and magnitude varies in time in the search for oil and gas accumulations.

A pore fluid is overpressured if its pressure exceeds the hydrostatic pressure at a specific depth (Grauls, 1999). Pore pressure usually lies between lithostatic and hydrostatic pressure (Hantschel and Kauerauf, 2009). Overpressure can be released or dissipated though the creation or reactivation of fractures and faults. These fractures occur once the reservoir pore pressure exceeds the least principal stress plus the tensile strength of the cap rock (Bolås and Hermanrud, 2003). A natural leakage of the formation following its fracturing can lead to the loss of hydrocarbon amounts. Main triggering mechanisms for the leakage in the Barents Sea are related to the complex geological evolution history that it has experienced over geological time (Duran et al., 2013; Nyland et al., 1992; Ostanin et al., 2012). Several studies have been done regarding the leakage dynamics of the Barents Sea (Duran et al., 2013; Ostanin et al., 2017; Vadakkepuliyambatta et al., 2013).

This study aims to predict and quantify the uncertainties regarding the timing and amount of leakage from overpressured areas in the Hammerfest Basin (Figure 1.1). Pressure measured in the wells today can be used for calibration to estimate the uncertainties related to the timing and amount of leakage for different compartments. This uncertainty in the estimates can be used as guidelines for possible hydrocarbon leakage risks. The outcomes are to be applied in basin modelling estimates of undrilled prospects. It has a big importance to model the amount and timing of leakage to be used in the future secondary migration analysis as well.

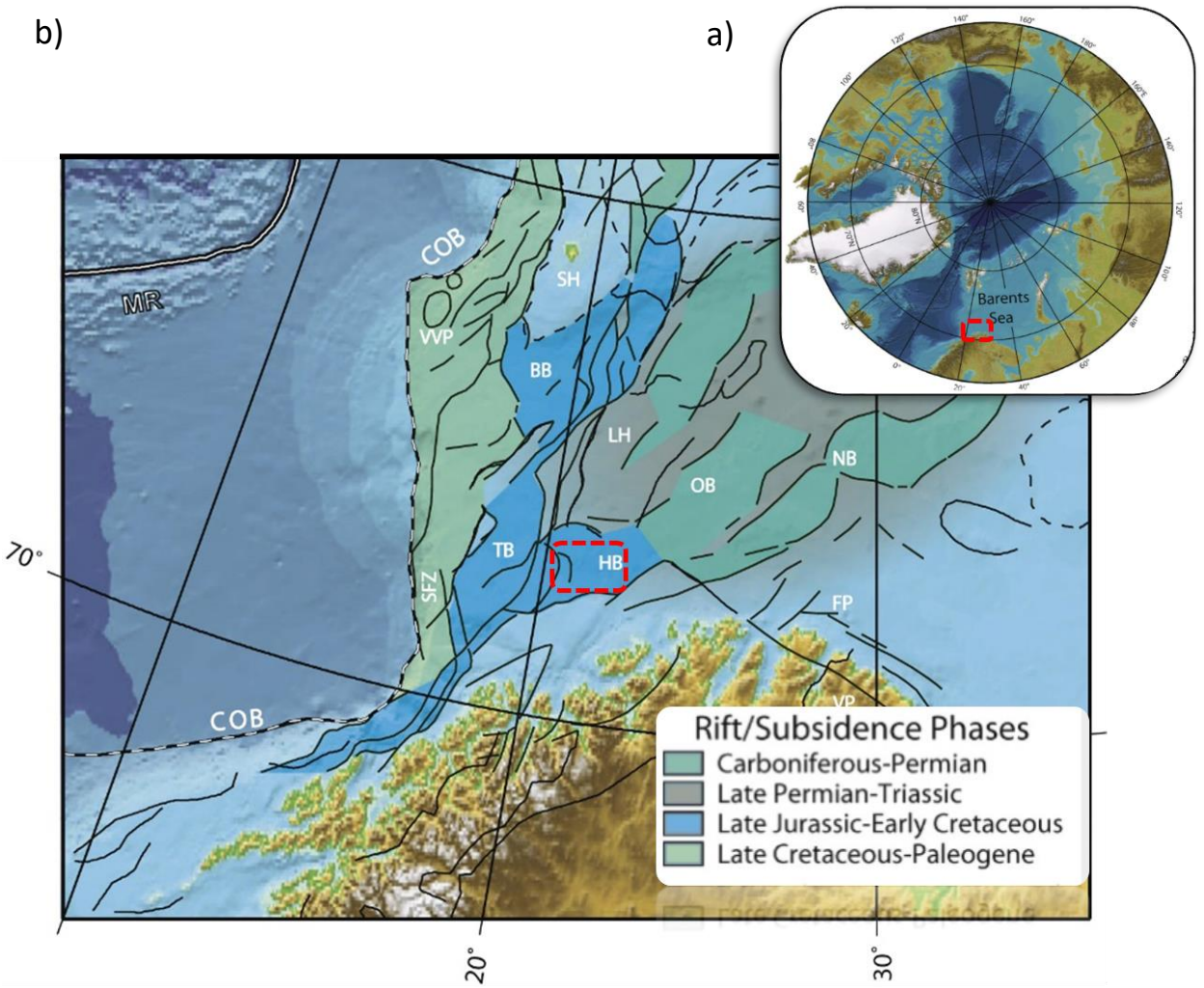


**Figure 1.1:** (a) Regional map of the Arctic (Jakobsson et al., 2008) with study area outlined in red and (b) base map of the southwestern Barents Sea. Major faults shown as black lines (Faleide et al., 2008). Local highs shown as dashed black lines. COB: continent–ocean boundary, SFZ: Senja Fracture Zone, VVP: Vestbakken Volcanic Province, BB: Bjørnøya Basin, LH: Loppa High/Selis Ridge, SH: Stappen High, TB: Tromsø Basin, OB: Ottar Basin, HB: Hammerfest Basin, NB: Nordkapp Basin, FP: Finnmark Platform, VP: Varanger Peninsula. The red dotted box highlights the study area. Modified from Clark et al., (2013).

## 1.1 Objective of the Project

The study is concentrated in south-western part of the Hammerfest Basin (Figure 1.1). The objective is to simulate water fluid pressure build up, overpressure evolution and possible fracturing and leakage for the reservoir rock, the middle Jurassic Stø Formation. Modelling the fluid pressure distribution over geological time to present day can contribute to reduce exploration risks and avoid dry wells. In order to model the fluid flow over geological timescales, several

geological factors need to be incorporated into the model such as timing and amount of erosion and uplift. The work will consider the influence of shale permeability, erosion, burial history and horizontal stress on the overpressure. Modelling results are evaluated considering the uncertainty range of these parameters and a Monte-Carlo approach has been used to describe their probability distributions. Overpressure and leakage histories are modelled on a geological time scale using software called Pressim (in-house SINTEF software).

The aims of this project are briefly listed in Figure 1.2 as bullets.

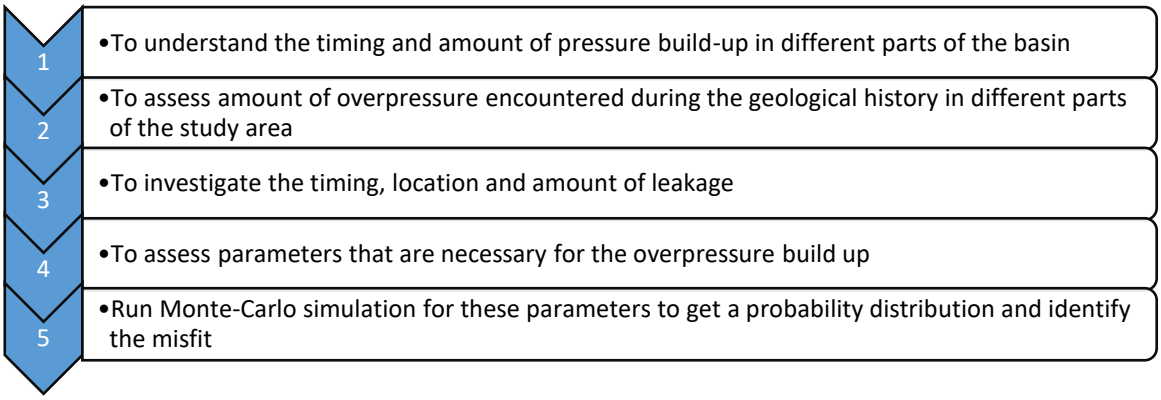


**Figure 1.2**: Objectives of the study

## 1.2 Components of the subsurface pressures

Pressure is the force per unit area acting on a surface. It is typically expressed in SI (international system) units as Pascal (Pa), where 1Pa=$\frac{kg}{m*s^2}$ and 1Pa is 10 bar. The stresses are represented by the weight of the overburden (lithostatic pressure) in the vertical direction and lateral components (represented by a maximum and minimum horizontal stress). These stresses are counteracted by fluid pressure within the pore space. The actual stresses the rock experience are termed effective stresses which often are represented as the total stress minus the pore pressure (Terzaghi, 1923).

$$\boldsymbol{\sigma_z = \int_{z_w}^{z}(1-\phi)\rho_s g dz + \int_0^z \phi\rho_w g dz} \qquad (1.1)$$

Figure 1.3 summarizes the relationship between lithostatic and fluid pressure change along the depth in an offshore environment and their approximate gradients.

Lithostatic pressure is the pressure generated due to the weight of overburden, or overlying rock, on a formation, also called geostatic pressure. This pressure gets transmitted through the subsurface by grain-to-grain contacts in the rocks, and its magnitude depends on the depth it is measured, density of the overlying rocks and acceleration due to the gravity. Hydrostatic pressure is exerted as a result of overlying water column within the pores. Pore pressure, on the other hand is exerted due to the part of this overlying column of water that contributes to the water flow. In a normally pressured environment, measured pore pressure would correspond to the hydrostatic pressure gradient (Hantschel and Kauerauf, 2009). Pore pressures in most deep sedimentary formations are overpressured, and in some areas with magnitudes double of the hydrostatic pressure (Zhang, 2011).

Abnormal pore pressure (overpressure) results when the fluid communication with the surface is inhibited by rocks of low permeability usually functioning as a seal. Common lithological barriers are evaporates and shales. Structural barriers can be provided by faults, though some faults seal and others do not seal.

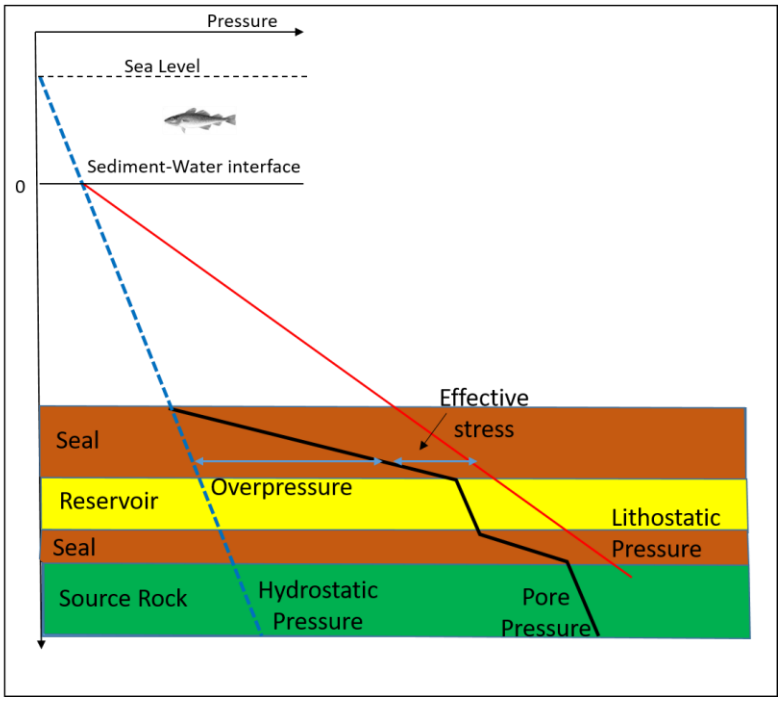


**Figure 1.3:** Definition of pressure and stress in an offshore environment. Redrawn from (Hantschel and Kauerauf, 2009).

The magnitudes of the greatest, intermediate, and least principal stress at depth ($S_1$, $S_2$, and $S_3$) in terms of $S_v$ (vertical stress), $S_{Hmax}$ (maximum horizontal stress) and $S_{hmin}$ (minimum horizontal stress) varies in different part of world, depending on the large-scale stress regimes. Three main stress regimes are classified by Anderson (1951), characterized by normal, strike-slip or reverse faults (Figure 1.4 and Table 1.1).

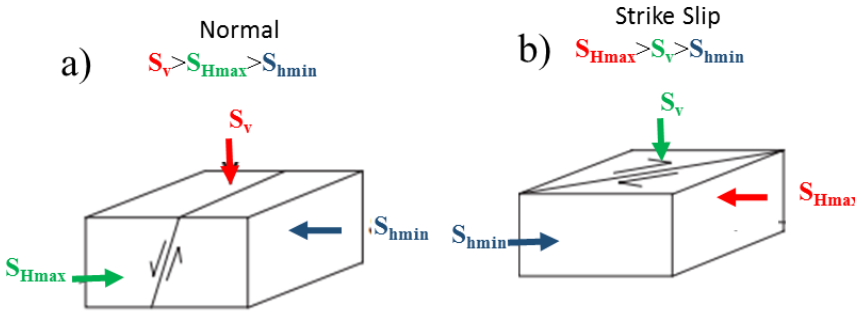


**Figure 1.4:** Anderson's classification scheme for relative stress magnitudes in (a) normal, (b) strike-slip. Redrawn from Zoback (2010).

**Table 1.1**: Relative stress magnitudes and faulting regimes (Zoback, 2010).

| Regime | Stress | | |
|---|---|---|---|
| | $S_1$ | $S_2$ | $S_3$ |
| Normal | $S_v$ | $S_{Hmax}$ | $S_{hmin}$ |
| Strike-Slip | $S_{Hmax}$ | $S_v$ | $S_{hmin}$ |
| Reverse | $S_{Hmax}$ | $S_{hmin}$ | $S_v$ |

## 1.3 Location of the study area

The Hammerfest Basin is a complex sedimentary basin, 70 km wide and 150 km long with an ENE-WSW trending axis (Figure 1.5a). It is the shallowest basin among the neighbouring basins such as the Nordkapp and Tromsø Basins. It is it separated from the Finnmark Platform to the south by Troms– Finnmark Fault Complex and from the Loppa High to the north by the Asterias Fault Complex and from the Tromsø Basin to the west by the southern segment of Ringvassøy-Loppa Fault Complex (Gabrielsen et al., 1990).

The study area covers the south-western part of the Hammerfest Basin which is well known for its oil and gas discoveries such as Snøhvit, Albatross, Askeladd and Alke.

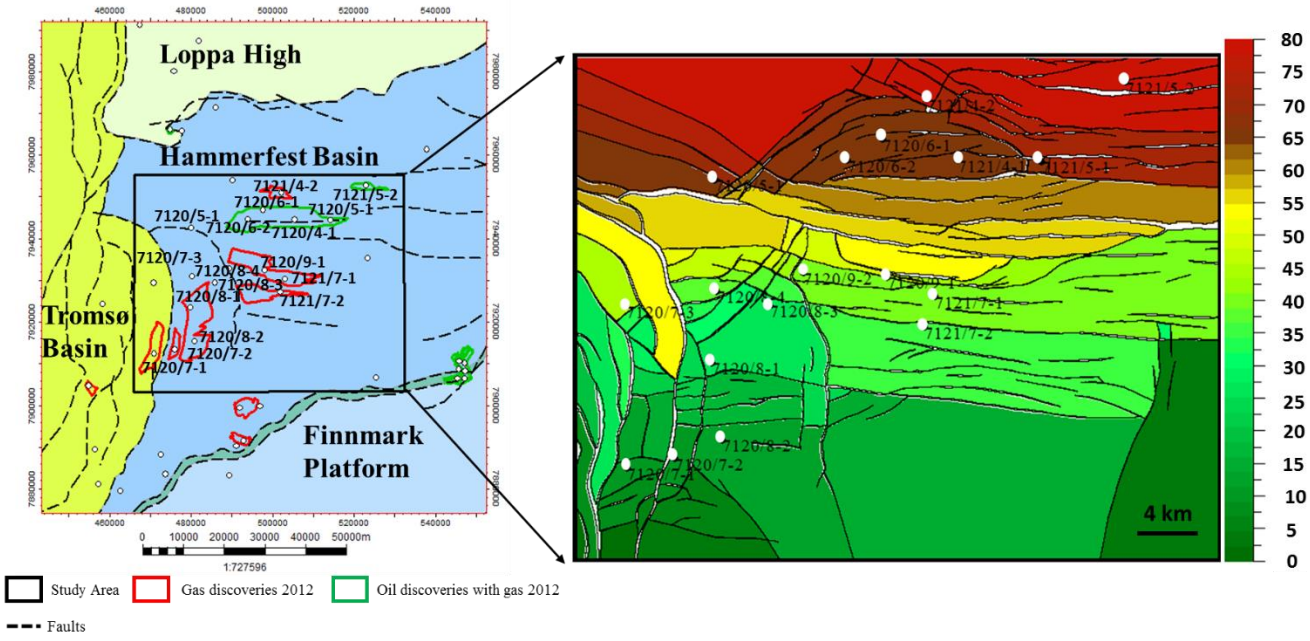


**Figure 1.5.** Outline of the study area (left). The compartmentalized map of Stø Formation imported into Pressim (right), the colours indicate the number of the compartments. Both figures have the locations of the wells used in the study highlighted.

## 1.4 Structure of the thesis

This thesis is divided into nine chapters, the last one being the references. The content of each chapter is given briefly in Table 1.2.

**Table 1.2:** The content of the chapters written as parts of the thesis work.

| | |
|---|---|
| Chapter 1 | ❖ Introductory knowledge about the thesis by providing the problem statement and intended aim<br>❖ Highlights of the study area. |
| Chapter 2 | ❖ Summary of the regional geology of Barents Sea<br>❖ Tectonic evolution of the Hammerfest Basin and its stratigraphy.<br>❖ Short description of the reservoir and seal rock in the study area based on the published literature study |
| Chapter 3 | ❖ What is overpressure modelling?<br>❖ Overpressure and its sources<br>❖ Mapping of high-amplitude anomalies |
| Chapter 4 | ❖ Input data<br>❖ Well data for pressure calibration<br>❖ Other data types to define the uncertainty ranges of the simulated pressure |
| Chapter 5 | In this chapter sensitivity analysis is performed for different parameters separately<br>❖ Minimum horizontal stress (Grauls number)<br>❖ Shale permeability<br>❖ Erosion scenarios<br>❖ Burial history |
| Chapter 6 & 7 & 8 | Monte-Carlo simulation results are showing the change of overpressure along the depth and probabilistic overpressure distribution. Discussion of how the input parameters used and remarks on the conclusion are made. |

# 2. Geological setting

## 2.1 Regional geology and geodynamic evolution of Barents Sea.

The continental margin offshore Norway and the western Barents Sea-Svalbard, between 62–82°N, evolved in response to the Cenozoic opening of the Norwegian-Greenland Sea as a mainly rifted and sheared margin (Faleide et al., 2008).

Late Paleozoic rift basins formed in the western Barents Sea along the NE-SW Caledonian trend. However a shift in the extensional stress direction from NE-SW to NW-SE is recorded by the prominent NE Atlantic-Arctic late Middle Jurassic–earliest Cretaceous rift episode, an event associated with northward propagation of Atlantic rifting (Faleide et al., 1993), see Figure 2.1. Considerable crustal extension and thinning led to the development of major Cretaceous basins off mid-Norway (Møre and Vøring basins) and East Greenland, and in the SW Barents Sea. These basins underwent rapid differential subsidence and segmentation into sub-basins and highs (Faleide et al., 2008).

The Barents Sea region is an intracratonic setting. Caledonian orogenic movements terminated in Early Devonian times and since then it has been affected by several episodes of tectonism (Gabrielsen et al., 1990). The main phases of lithospheric stretching include Devonian-Carboniferous (375-325 Ma), Early Triassic (245-241 Ma), Late Jurassic – Early Cretaceous (157-97 Ma), and Paleocene-Early Eocene (60-50 Ma) (Reemst et al., 1994; Skogseid et al., 2000). Duran et al, (2013) excluded the Triassic for its broad regional subsidence (Figure 2.1).

The post-Caledonian history of the western Barents Sea is comprised of three major extensional phases (Faleide et al., 1993). The Late Paleozoic extension dominated by Devonian collapse of the newly formed Caledonian orogenic belt, which was followed by widespread rifting during the Carboniferous. At a later stage of the geological history this led to the development of half grabens in the western Barents Sea (Faleide et al., 1993; Hendriks and Andriessen, 2002; Henriksen et al., 2011). Deep basins in the west separated from the shallow basins in the east, as a result of renewed rifting phase that occurred during the Late Jurassic to Early Cretaceous (Gabrielsen et al., 1997). The focus of rifting has moved westward and rifting terminated with the opening of the Norwegian-Greenland Sea during the Paleocene-Eocene (Faleide et al., 1993; Henriksen et al., 2011).

Suggested mechanisms for the uplift periods had been summarized by (Doré and Jensen, 1996) which include pre-opening Atlantic margin elevation (Ghazi, 1992; Torske, 1972), mantle phase changes (Riis and Fjeldskaar, 1992), flexural response to sediment loading (Ghazi, 1992; Sales, 1992), intraplate stresses (Cloetingh et al., 1990), isostatic response to sedimentary unloading (Riis and Fjeldskaar, 1992) or a combination of several of these mechanisms (e.g. (Dengo and Røssland, 2013; Jensen and Schmidt, 1993; Reemst et al., 1994). After breakup, the passive margin evolved in response to subsidence and sediment loading during the widening and deepening of the Norwegian-Greenland Sea. Sedimentation was modest until the Late Pliocene when the glaciation led to rapid progradation and greatly increased sedimentation rates forming huge, regional depocenters near the shelf edge offshore Mid-Norway and in front of bathymetric troughs in the northern North Sea and western Barents Sea (Faleide et al., 2008).

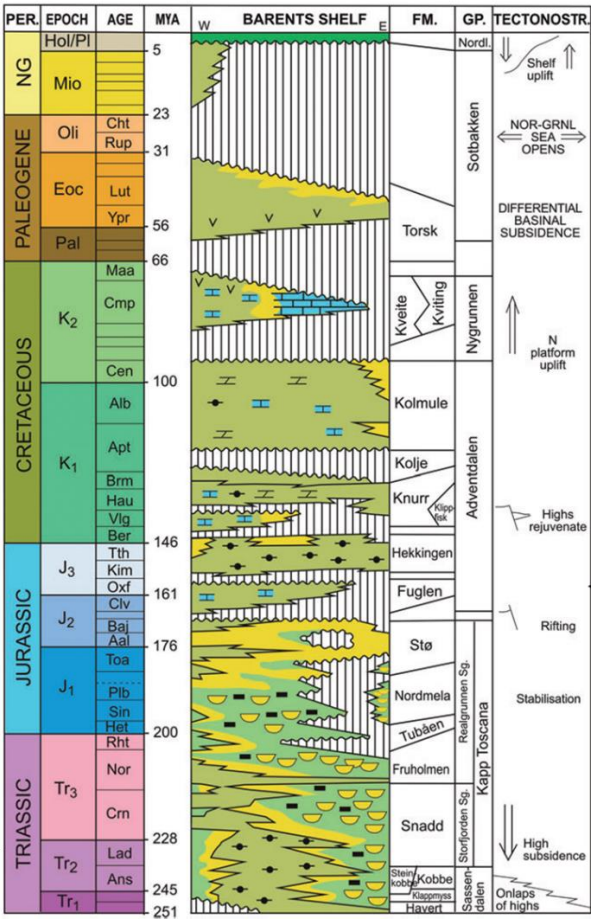


**Figure 2.1**: A generalized stratigraphic succession of the Barents Sea. The main tectonic events are shown to the right. Reworked from Worsley (2008), Nøttvedt et al,(1993) , time scale; Gradstein et al, (2004).

## 2.2 Evolution of the Hammerfest Basin

Interpretation of the Hammerfest Basin is a failed rift in a triple junction (Gabrielsen et al., 1990; Talleraas, 1979). The Hammerfest Basin is bounded on the south by the Troms-Finnmark Fault complex and on the north by a combination of faults and a flexure. Transition to the Tromsø Basin in the west has been marked by north trending zone of rotated fault blocks (Ringvassøy-Loppa Fault Complex) (Faleide et al., 2008). As the basin gets narrower and shallower, structural relief dies out towards the east. Maximum subsidence in the basin has been observed along the northern and southern margins. The central part of the basin is dominated by E-W trending fault system formed by flexural extension related to the doming (Sund et al., 1986). All of these processes mirror the late Jurassic tectonism.

The shift of stress-field vector in the Late Jurassic-Early Cretaceous is responsible for the creation of the Hammerfest Basin.

❖ Intra-cratonic basin form was evident on the area occupied by the present Hammerfest Basin starting from the late Paleozoic until the end of Jurassic times. E-W extensional regime in the Late Carboniferous and Permian times followed the Late Devonian and Carboniferous tectonic style.

❖ Following the creation of the Hammerfest Basin in the Early Cretaceous time, thick Cretaceous and Tertiary clastic deposits covered the Jurassic and Triassic sequences in the basin. The Tertiary overburden, in places in excess of 1 km in addition to the present thickness, adversely affected the porosity development by favouring quartz dissolution and cementation (Berglund et al., 1986). In Late Pliocene, the area again was submerged and covered by a thin blanket of Upper Pliocene to Pleistocene sediments.

The uplift and erosion of the Norwegian Barents Shelf, associated with the opening of the Norwegian-Greenland Sea since earliest Eocene and with the Late Pliocene-Pleistocene glaciations, spans over several million years. The precise timing of uplift and erosion is difficult to constrain due to the missing sections from Eocene to Pliocene below the upper regional unconformity in the entire Barents Sea, except in the western margin basins where a nearly complete Cenozoic succession is present (Ryseth et al., 2003).

## 2.3 Stratigraphic development of the study area

Generalized lithostratigraphy and the main tectonic events influencing the southwestern Barents Sea are depicted in Figure 2.1. This subchapter will give the major information regarding the sediment deposition during each stratigraphic age period.

The half-grabens formed during the initial phase of crustal extension filled with the oldest Late Devonian-Early Carboniferous aged alluvial sediments (Dengo and Røssland, 2013).

Basin subsidence was dominant during Permian times (Berglund et al., 1986), while in the Late Permian-Early Triassic crustal warping was followed by cyclic infill of shales and sandstones (Ørret Formation) over the carbonate platform developed in the Carboniferous-Permian time. During the Early-Middle Triassic, there was a deposition of three progradational units namely Havert, Klappmys and Kobbe formations (Nøttvedt et al., 1993).

The Late Triassic was characterized by regional subsidence and deposition of the large sediment volumes of the Snadd and Fruholmen Formations, which are mainly recognized as possible source rocks, alongside the Kobbe Formation (Faleide et al., 2008; Nøttvedt et al., 1993). The Fruholmen Formation has also thick sand bodies (up to 30 m) in some parts which are interpreted as distributary channels, probably of anastomosing or meandering rivers (Berglund et al., 1986).

Tubåen, Nordmela and Stø Formations represent deltaic sediments of the Lower and Middle Jurassic (Nøttvedt et al., 1993). The Nordmela Formation has a major alternating characteristic of fine-grained sandstones, siltstones and mudstones. There is a well-defined sharp conglomeratic contact at the base of the overlying thick sandstone unit of the Stø Formation (Berglund et al., 1986).

Middle to Upper Jurassic marine sediments of the Fuglen Formation and the organic-rich shales of the Hekkingen Formation were deposited as a result of a global sea level rise. Among these two, the latter is considered as the main oil-prone source rock of the study area (Berglund et al., 1986; Nøttvedt et al., 1993).

Tectonic activity during the Paleogene started related to the opening of the North Atlantic and Arctic oceans after the deposition of the Cretaceous Knurr, Kolmule and Kvite Formations (Dengo and Røssland, 2013).

The final lithospheric break-up of the Norwegian margin approximately marked the deposition transition of a thick Palaeocene to Eocene sequence (Torsk Formation) over a broad area of the western Barents Sea. This break-up is assumed to occur near the Palaeocene-Eocene boundary at 55 Ma (Faleide et al., 2008). Following this, sediment deposition development on the passive margin took place along the western Barents Shelf. During Mid-Oligocene, when the eastern areas of the basin were subjected to deep erosion due to tectonic uplift, the final phase of separation took place in the western area (Berglund et al., 1986; Duran et al., 2013). Northern hemisphere climate deteriorated considerably approximately 2.5 Ma ago due to the formation of large ice-caps From this time onward, the Barents Sea evolution was characterized by alternation of these two major effects: the erosion of sediments and loading of the lithosphere due to the large ice-caps followed by unloading and uplift during deglaciation (Reemst et al., 1994)

## 2.4 Petroleum System Elements of the basin

A petroleum system is a geologic system that encompasses the hydrocarbon source rocks and all related oil and gas accumulations and which includes all of the geologic elements and processes that are essential for a hydrocarbon accumulation to exist (Magoon and Dow, 1994). In this thesis, the focus will be on the reservoir and the cap rocks and hydrocarbon preservation.

### 2.4.1 Reservoir and seal rocks.

The Middle Jurassic Stø Formation is a well-known reservoir rock of the basin (Duran et al., 2013). It is mainly charged with gas and has a thin oil leg in the Snøhvit field. It contains hydrocarbon not only in the Snøhvit field but also many other fields of the Barents Sea.

Jurassic strata contains the largest proportion of hydrocarbon resources proven to date, in terms of the reservoirs. The major discoveries are in the Middle Jurassic sandstones of the Stø Formation, which contain about 85% of all the Norwegian Barents Sea reserves (Doré and Jensen, 1996; Duran et al., 2013). Sands of the Stø Formation were deposited in prograding coastal regimes, and a variety of linear clastic coast lithofacies are represented (Dalland et al., 1988). The thickness map of the Stø Formation shows an increase in thickness from east towards the west, see Figure 4.2 (Dalland et al., 1988; Halland et al., 2013). The best reservoir rocks of the Stø Formation exhibits porosities up to 17% and core permeabilities ranging from 150 mD to 500 mD based on the measurements carried out in the Snøvit field (Linjordet and Olsen, 1992).

The Stø Formation is overlain by the Fuglen Formation. Hekkingen Formation shales were deposited in an offshore setting, and conformably overlie the interbedded lower-delta-plain sandstones, siltstones, and shales of the Lower Jurassic Nordmela Formation and underlie the Fuglen Formation (Walderhaug and Bjørkum, 2003).

The Upper Jurassic Fuglen and Hekkingen Formations are the two well-known seal rocks of the basin (Duran et al., 2013; Linjordet and Olsen, 1992). The Fuglen Formation has a thickness of 7 to 30 m, whereas the Hekkingen Formation ranges from 80 to more than 100 m thick in a northward direction near the Snøhvit field (Linjordet and Olsen, 1992). Referring to the work published by Duran et al, (2013) hydrocarbons are predicted to start filling the reservoir (Stø Formation) from 80 Ma onward. By this time the main sealing units were already deposited and to a large degree consolidated when one of the main filling pulses into the Stø Formation took place, at approximately 55 Ma. This is indicated by porosity values below 15%, specifically 11.6% for the Fuglen Formation and 7.5% for the Hekkingen Formation (Duran et al., 2013). The Jurassic Hekkingen Formation is considered as an oil prone source rock in the western part of the Hammerfest Basin. Ohm et al, (2008) suggested that Hekkingen Formation is generally early mature when the Triassic aged source rocks are oil mature, and it is oil mature when the Trassic source rocks are gas mature.

# 3. Methodology

## 3.1 Introduction

Overpressure prediction is one of the biggest challenges that petroleum industry is facing, as the companies move exploration into deep water zones (Swarbrick and Schneider, 1999). The ability to predict pressure is critically dependent upon including all processes relevant to pressure in the model and providing accurate values of the critical parameters (Waples, 1998). The Pressim simulator is built to describe the overpressure history for a basin. This simulator calculates the pressure distribution in a sedimentary basin though geological time, as presented in detail in Borge, (2002). The methodology and the simulator used in this thesis aims to take into account all relevant processes to quantify their effect on overpressure generation and dissipation through describing 3D fluid flow within the basin over a geological time. Modelling of the fluid pressure distribution can contribute to reduce exploration and technical risks.

The simulator is able to perform single- and multi-layer generation and dissipation of overpressures defined by pressure compartments. In this study, single-layer generation and dissipation is going to be implemented for the Stø Formation.

The fluid pressure distribution in a carrier or reservoir rock can influence the secondary migration of petroleum in a sedimentary basin.

## 3.2 What is being modelled?

The main idea behind the model developed is to predict overpressure distribution (map) over the study area. There are five main processes that are generating or dissipating pressure, that is modelled using Pressim. These processes are lateral fluid flow, shale drainage, shale compaction, quartz cementation and hydraulic leakage (Figure 3.1).

The main methodology here is based upon the assumption that sealing faults divides the basin into pressure compartments. Shales deposited above and below these compartments are the main delineating factors of pressure. In other words, a pressure compartment is bounded horizontally by the fault pattern at the top of the reservoir formation, and vertically by impermeable rocks (Lothe, 2004). These fault bounded pressure compartments are used in order to diminish the necessity for computation capacity and memory allocation (Lothe et al., 2009). Depth converted seismic horizon maps of the overlying sediments have been used as input for the decompaction.

Based on the work done by Lothe, (2004) and Borge, (2000), it has been proved that pressure and stress are interrelated and therefore need to be simulated simultaneously. Failure in the cap rock is controlled by pressure build up and differential stress. Both shear failure and tensile failure can be hydraulic driven (Figure 3.8) and they are dependent on the burial depth and overpressure. The timing and amount of hydraulic fracturing and leakage due to overpressure can be evaluated in different parts of the basin by using the simulator (Lothe, 2004). In Pressim, development of pressures and stresses are reported for a series of time steps. These time steps are correlated to the depositional ages of the stratigraphic horizons that are used to build the model, mainly younger than the Stø Formation. Mechanical compaction (Baldwin and Butler, 1985) is modelled by using the porosity-depth relation in the shales, and chemical compaction of the sands modelled by using kinetic model for quartz cementation (Walderhaug, 1996).

The following points highlight the outputs of the single simulation run which are going to be discussed in this study:

- Pressure distribution maps for each time step
- Hydraulic and cumulative leakage maps for each time step
- Statistical approach

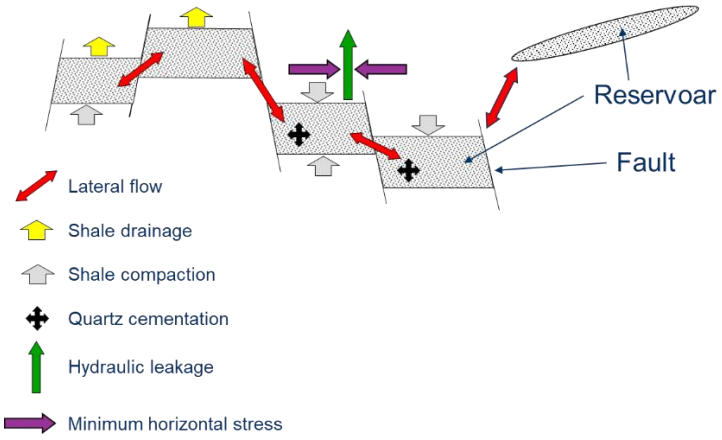


**Figure 3.1:** Pressim models all processes for pressure generation and dissipation

## 3.3 How do we model?

Pressim uses a forward Euler technique for solving the system of linear equations that describe the flow pattern in the basin. Since this simple numerical method is an unstable method, an automatic time step chopper is implemented to the dissipation algorithm in order to automatically stabilise the simulations (Borge, 2000).

In order to perform a reliable modelling procedure, it is important to understand the entire system, including both the reservoir and the cap rock. There are five processes that need to be evaluated for the basin prior to starting the simulation (Lothe, 2004).

1. **Overpressure and pressure generating mechanisms.**

There are several well-known mechanisms in literature triggering the overpressure generation: such as burial depth, tectonic hydrocarbon generation, mineral transformation and temperature increase. Based on the paper by Swarbrick et al., (2001) the most important factor for overpressure generation in young sediments is rapid sediment burial. Yassir and Addis, (2002) showed that there are two types of overpressure related to the stress. These are vertical loading and tectonic loading. The magnitude of tectonic loading is difficult to quantify back in time. Therefore, it is neglected in this model.

2. **Stress generating mechanisms at different scales.**

One of the important controlling mechanisms for the overpressure dissipation in sedimentary basins is the orientation, magnitude and lateral variations of the principal stresses in the basin through time. Fejerskov and Lindholm, (2000) and Lothe, (2004) divided the stresses into three different scales namely continental, regional and local and each of these contributes to the total stress pattern as pressure generating mechanisms (Table 3.1).

**Table 3.1**: Lithostratigraphic stress generation mechanisms (Fejerskov and Lindholm, 2000; Lothe, 2004)

| Stress field | 1st order Continental | 2nd order Regional | 3rd order Local |
|---|---|---|---|
| Lateral stress field extent | >1000 km | 100-1000 km | <100 km |
| Stress generation mechanism | Plate tectonic forces<br>Ridge push<br>Basal drag<br>Slab pull | Large-scale density inhomoginites;<br>• Continental margin<br>Flexural stresses;<br>• Sedimentary loading<br>• Deglaciations<br>Wide topographic loads. | Topography<br>Geological features;<br>• Faults<br>• Hard and soft inclusions |

3. **Geo-mechanical properties of the cap rock.**

Shales are usually considered to be effective seals. But the degree of sealing is dependent upon the extent of compaction. At shallow depths clay and shale material is permeable for the formation fluids due to high values of porosity. Mechanical compaction starts from the time of the burial of the sediments and is controlled by effective stress, grain size distribution and minerology (Bjørlykke, 1999). Increase in the effective stress reduces the permeability as the large pore spaces collapse progressively. Chemical compaction is controlled by the subsurface conditions (temperature, total vertical stress and pore pressure), the water flow and water chemistry (Hantschel and Kauerauf, 2009).

4. **Flow properties to pre-existing faults.**

Faults can act as conduits for fluid flow but they can also form pressure barriers between compartments. Burial history, fault reactivation, minerology and diagenesis can change the fault properties from sealing to open or vice versa. There is always a small-scale network of faults propagated around the main faults. The zone of these small-scale faults is known as the damage zone (Figure 3.2). There is a separate study done by (Lothe, 2004). in order to understand sub-seismic faults and their possible influence on overpressure and hydraulic leakage in the offshore Norway area. Large faults are likely to control the lateral fluid flow in the overpressured areas but sub-seismic faults can also be important pressure barriers in the basin.

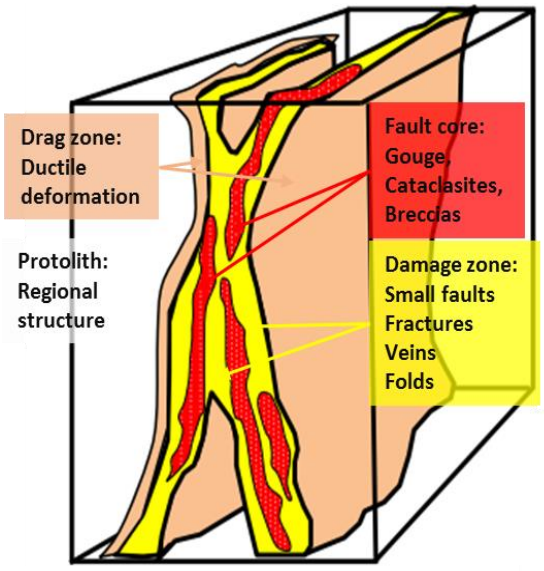


**Figure 3.2:** Fault zone architectural. Redrawn from (Caine et al., 1996)

5. **Initiation and mechanism for hydraulic fracturing and leakage**

Hydraulic fracturing and leakage is well understood as a result of the effort made in terms of reservoir optimization operations, but it is less understood as a natural phenomenon generated due to overpressure. The timing of the hydraulic failure and amount of the hydraulic leakage can be estimated from the top of each pressure compartment based on the incorporated failure criteria that is included in the pressure simulator (Chapter 3.5.3).

## 3.4 Pressure generating mechanisms

One can distinguish between three processes that generate pressure:

- Mechanical compaction
- Chemical compaction, for example: quartz cementation
- Fluid expansion (Osborne and Swarbrick, 1997; Swarbrick et al., 2002)

### 3.4.1. Mechanical compaction

Sedimentary compaction is the main process for overpressure generation. Compaction is the term that encompasses the rearrangement of the grains to denser packages with a reduction in pore space related to the decrease in pore throats and connectivity of the pore network (Hantschel and Kauerauf, 2009) (Figure 3.3).

Swarbrick et al., (2001) termed this mechanism as “disequilibrium compaction,” and explained physical manifestation in the bulk rock as excess pore pressure and a higher porosity relative to the normally pressured, fully compacted rocks at the same depth. The overburden load can act on the pore fluid and the rock grains according to their compressibilities. The compaction process itself is driven by incremental fluid outflow that leads to the difference between the rock stresses and pore pressure.

The main controls on overpressure from disequilibrium compaction have been demonstrated by Luo and Vasseur, (1992) as a loading rate, compaction coefficient (a method of expressing rock compressibility), temperature, and permeability, which controls the rate of fluid expulsion. Much of the published literature (Swarbrick et al., 2001; Wangen, 2000) agrees on the idea that mechanical compaction processes govern porosity reduction and fluid expansion.

The porosity reduction is directly related to the vertical overburden generated stress. There are several models that had been used to demonstrate this relation with a physical formula. The most well-known one is suggested by Athy, (1930). He found that the porosity observations made in sedimentary basins are a good fit to an exponential trend by decreasing porosity with depth and concluded that porosity can be related to the effective vertical stress in unlithified sediments taking into account Terzaghi’s observations. Finally, mechanical compaction is assumed to be an overpressure reducing mechanism. The remaining overpressure could be simply interpreted as a

result of incomplete compaction and therefore this process of overpressure formation is called undercompaction (Hantschel and Kauerauf, 2009).

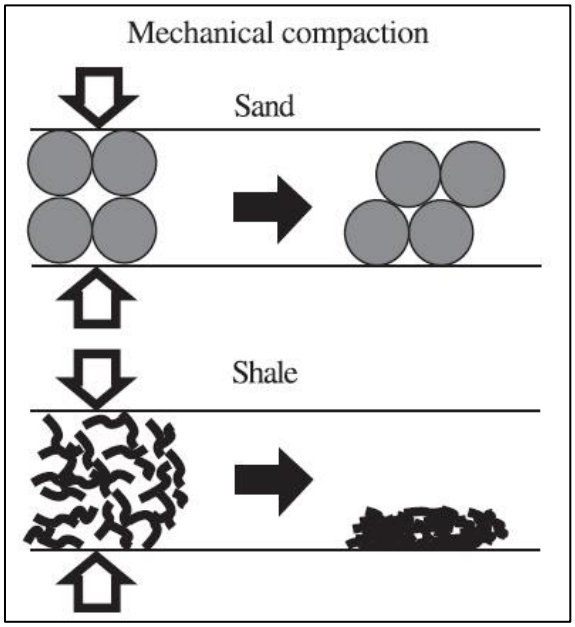


**Figure 3.3:** Schematic illustration of mechanical compaction

### 3.4.2 Quartz cementation

Mechanical compaction assumes that the main controlling factor for the reduction of porosity is limited to the vertical effective stress, but it is uncertain to what extent this is a good model for the porosity loss in lithified sediments. It has been the major focus point in several publications whether the porosity loss is controlled by chemical processes rather than by mechanical compaction in lithified rocks (Bjørlykke, 1999; Bjørlykke and Høeg, 1997). Chemical compaction is a result of the quartz and carbonate cementation. This reduces porosity and it is mainly responsible for porosity reduction at large depths (below 2.5 km), whereas below this cementation depth mechanical compaction is negligible (Hantschel and Kauerauf, 2009, p. 35; Walderhaug, 1994, 1996). The cementation process leads to the expulsion of fluids in the depth interval where overpressure is normally observed. In addition, cementation destroys permeability similar to mechanical compaction (Wangen, 2000).

Quartz cementation is strongly driven by temperature and the threshold temperature to initiate this cementation is above $80^0$ C. Stylolites in sandstones occur as fine structures at grain contacts. It is believed that they are the source of silica in precipitation of quartz cement. Bjørkum et al., (1998) suggested quartz-clay stylolitization and quartz reprecipitation as a principal cause of overpressure

in quartz-sandstone reservoirs. Quartz cementation can be regarded as a three step processes: dissolution of quartz at the grain-grain contacts, transportation of quartz though space and precipitation of silica on free quartz grain surfaces by taking up space from the porosity of the rock (Walderhaug, 1996). Temperature affects the diffusion constant and precipitation rate of the quartz cement. Mica minerals can act as a catalyst for dissolution of quartz.

Formation of quartz cement along the surface of the sediments is inhibited in the existence of the grain coating and microquartz elements (Walderhaug, 1996; Worden and Morad, 2000) (Figure 3.4).

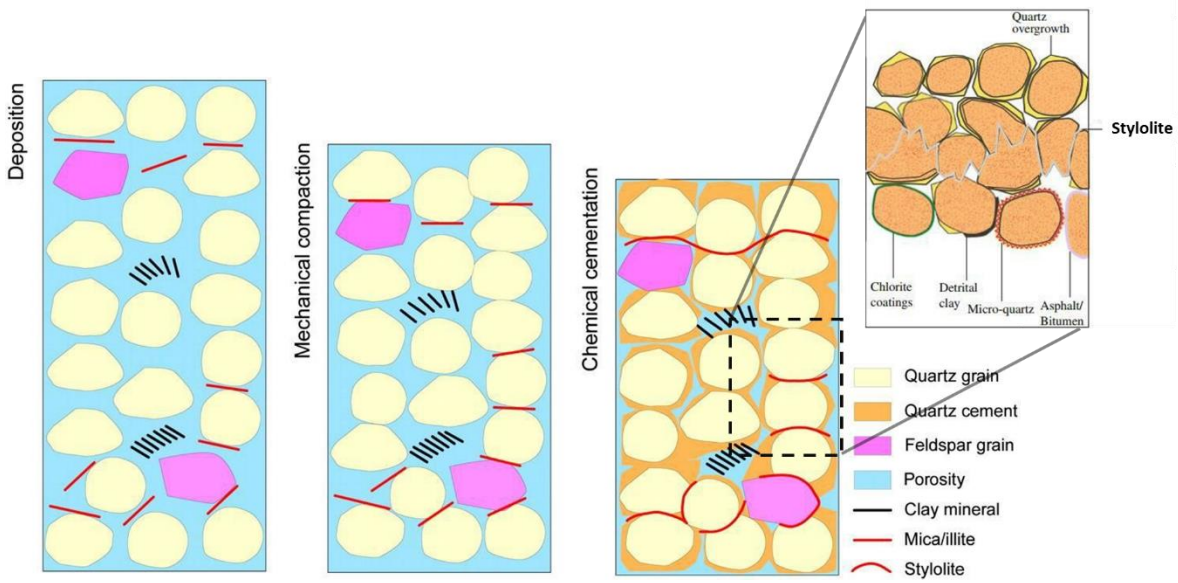


**Figure 3.4**: Illustration of the different overpressure mechanisms and stylolites together with surrounding grains. Note that quartz cement does not influence coated grains. Edited from Bjørlykke and Jahren (2010) and Nadeau (2011).

### 3.4.3 Secondary overpressure generating mechanisms

There are several types of mineral transformations that occur during burial which include feldspar to illite, smectite to illite, and anhydrite to gypsum. These processes involve a set of complex reactions that are largely kinetically controlled. Some of these related processes increase, some of them decrease the pore water volume with a general release of water into pore space and with a total increase of water relative volume up to the 5%. The increase in the volume of the matrix due to the ion exchange process in terms of mineral transformations can also be part of this mechanisms.

Fluid expansion mechanisms include oil and gas generation, oil to gas cracking and aquathermal expansion. The contribution to the overpressure as a result of fluid expansion is highly dependent on oil and gas compressibility due to the fact that mass or the density change yields fluid pressure increase controlled by compressibility (Hantschel and Kauerauf, 2009). In general, overpressure increase due to fluid expansion mechanisms is usually small compared to that of chemical and mechanical compaction (Wangen, 2001).

## 3.5 Modelling in Pressim

The three steps of overpressure modelling are explained in more detail in this chapter.

### 3.5.1 Pressure generation

Several different sources of overpressure generation have been explained in the previous subchapters. Not all of these mechanisms will be accounted in the overpressure modelling. Only two of them: compaction of the over- and underlying shale and quartz cementation will be considered.

The two different models for the generation of overpressure are implemented. There are several published porosity-depth curves for sandstone, shale and carbonate (Giles et al., 1998). Despite of the fact that these porosity curves may vary up to 35% at certain depths, the general trend is clear: porosities in all types of sedimentary rock are significantly reduced during subsidence, even below the depths at which overpressures starts to build up (Borge, 2002). In order to account for this porosity loss, which plays an important role in the modelling outputs, mechanical compaction and cementation of sands and an empirical compaction model of shales have been included in the Pressim model. The rate of change in porosity with depth model has been employed from Sclater and Christie, (1980) (Figure 3.5). The model takes into account only the mean porosity reduction in compartments.

Borge, (2002) argues that simple models, such as the one implemented in Pressim, describing the porosity development are sufficient for this purpose. However, he also mentions that it is essential that the mean porosity development is realistic regarding the pressure generation.

Once the quartz cementation temperature threshold reaches ($80^0$ C), the chemical compaction takes over the role of mechanical compaction to account for the further porosity reduction.

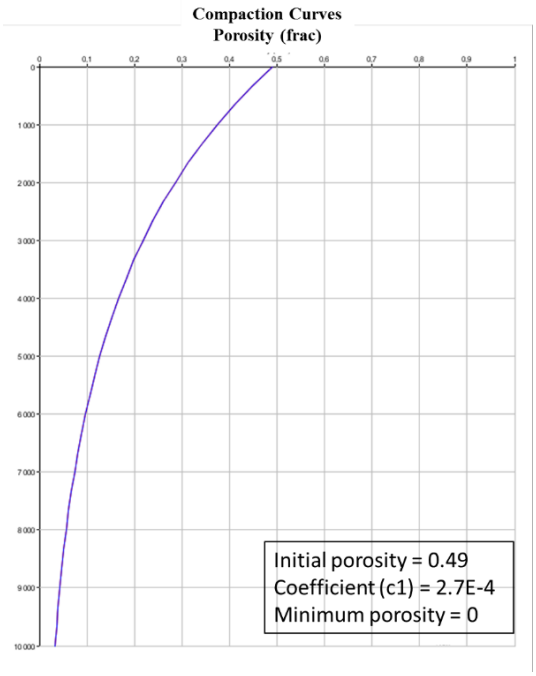


**Figure 3.5:** Porosity depth relation applied in this study (Sclater and Christie, 1980).

### 3.5.2 Pressure dissipation

At shallow depths clays and shales are usually considered to be permeable to the formation fluids because of high porosity. This is the main reason why overpressure is not being observed at shallow depths even though the temperature increases. Pressure corresponds to the hydrostatic pressure at this depth. In addition, mechanical compaction processes are usually very active at these depths (Borge, 2002).

Figure 3.6 shows simple vertical fluid flow model proposed by Borge, (2002) to describe the sealing effects of the shales instead of applying Darcy law to estimate shale permeability. Shale drainage in the caprock is determined depending on burial depth, with a drainage zone, a transition zone and accumulation zone.

Starting from the sealing depth ($z_s$), shales are completely acting as a seal to the vertical fluid column. However, lateral dissipation takes over the vertical flow zones in the vertical fluid flow model (Borge, 2000). The drainage curve illustrates a probable modelled relation between shale sealing capacity and becomes the dominating draining mechanism for reservoir units as a response to this.

The permeability of the faults versus depth is defined as an input parameter to calculate its transmissibility and it can be varied from sealing, partly sealing and non-sealing depending on the depth and fault throw (Borge and Sylta, 1998). The input parameters for the transmissibility of the faults help to calculate the flow across the faults and resulting overpressure in all the pressure compartments. The transmissibility values are default input set in this study and they depend on the burial depth, the length, width and the dip-slip displacement of the faults, thickness of the reservoir layers and the permeability inside the fault block (Borge and Sylta, 1998).

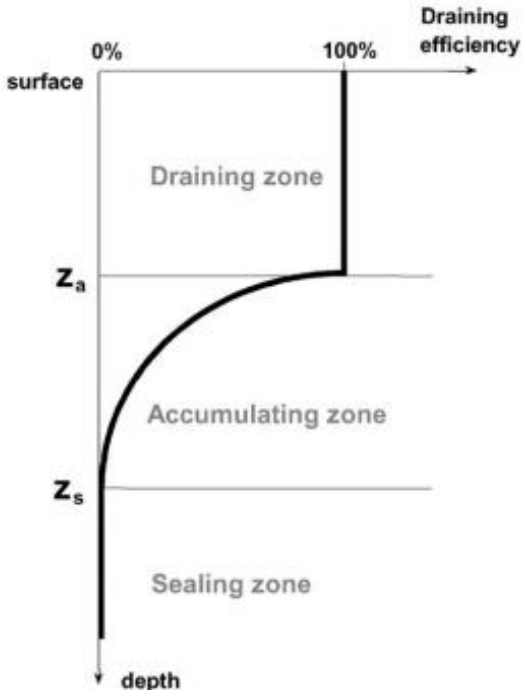


**Figure 3.6:** The vertical flow zones in the vertical fluid flow model (Borge, 2000). The drainage curve illustrates a probable modelled relation between shale sealing capacity and depth.

### 3.5.3 Hydraulic leakage and Frictional criteria.

In the approach of this study, the water excess pressure is dissipated by Darcy flow. If this process is too slow (i.e. the water cannot escape during sediment compaction), the overpressure may increase to such magnitudes that the sediment rock strength cannot withhold the escaping water. In these circumstances, hydraulic fracturing occurs and the excess pressure is dissipated with the leaking fluid. Hydraulic failure is hence usually taking place in pressure compartments at depths where the pressure generation/porosity reduction is active, and in addition, has a poor connectivity to the hydrostatically pressured parts of the basin.

In order to estimate timing of hydraulic failure and amount of leakage from the top point of each pressure compartment, failure criteria, named Griffith-Coulomb, is incorporated into the pressure simulator. It is the combination of Griffith and Mohr-Coulomb criteria. The point where the Mohr circle "touches" the Griffith-Coulomb failure envelope is defined as the rupture (failure) of the cap rock and subsequent leakage (Lothe, 2004). The Griffith-Coulomb failure criterion was used for the first failure, while the frictional sliding criterion was used for the reactivation of the failure, see Figure 3.7 (Lothe, 2004). The Mohr circle is constructed based on the maximum ($S_1$) and minimum principal effective stress values ($S_3$). In this study, the assumption is made such that, the overburden weight (vertical stress) is one of the principal stress components. The minimum horizontal stress is considered as another principal component. The value of the minimum horizontal stress at the top of a pressure component is given by empirical formulas (e.g. Grauls, 1998). The point of failure changes as the confining stresses defining the Mohr circle changes during burial history. Confining stress, $S_1$ usually changes as a response to the geological processes such as deposition and erosion of the sediments. Correspondingly, the second confining stress $S_3$ follows the similar trend with $S_1$.

Generally, Griffith-Coulomb failure criterion is parabolic in the tensile regime (Griffith part) and a straight line (Mohr-Coulomb part) in the shear regime (Figure 3.7). Stress states corresponding to Mohr circles which exceed the failure line are not allowed because failure of the rock would have occurred prior to the rock having achieved such a stress state (Zoback, 2010). Once the fault is activated, frictional sliding criterion should be used due to the loss in the cohesion (C) in the cap rock (Figure 3.7). As a result of this rupture the simulator shifts to the frictional sliding criterion which implies loss of cohesion in the cap rock.

In Figure 3.7, μ (coefficient of internal friction) is defined to describe the increase in strength of intact rock with pressure (i.e. the slope of the failure line on a Mohr diagram) in the context of failure of an initially intact rock using the linearized Mohr–Coulomb failure criterion., whereas μ' (coefficient of sliding friction) describes slip on a pre-existing fault in that material (Zoback, 2010). The Mohr-Coulomb criterion is independent of $S_2$.

Shear (deeper parts) or tensile failures (shallower parts), due to the hydraulic seal failures, can occur as a response to the development of fracture swarms, see Figure 3.8 (Lothe, 2004), but in this study the leakage of the fluid from the compartments is mainly related to the shear failure.

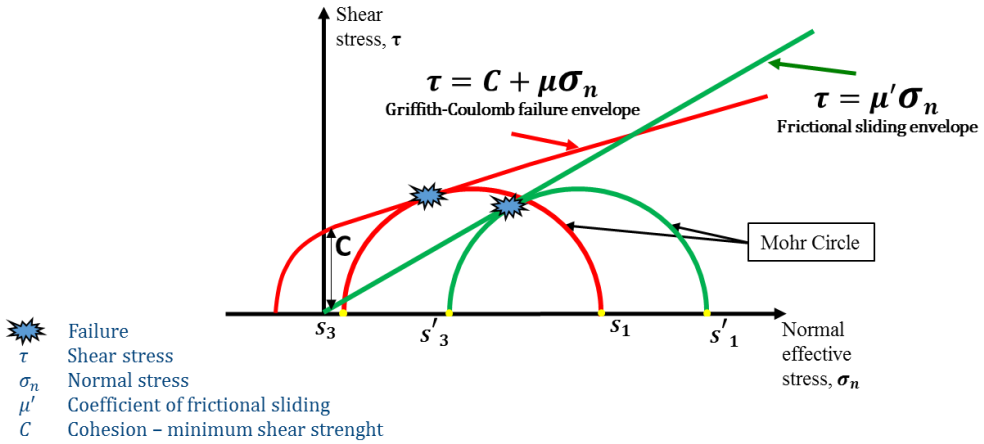


**Figure 3.7**: A combination of Griffith-Coulomb failure criterion and the frictional sliding criterion used in the present simulations. The green line shows the frictional sliding criterion when the rock material loses cohesion (C) due to failure (Lothe, 2004)

In this study $S_1$ and $S_3$ are calculated for every 10000 time step in the simulation. This means that, in approximately every 10000 years, there is a new layer that is introduced (or removed) into (from) the model. With the introduction of this new layer, the porosity is recalculated for the underlying layers followed by an update of rock physics parameters (unconfined compressive strength, tensile strength, cohesion, and frictional rock strength).

Figure 3.9 shows a geological illustration of a compartmentalized reservoir and the leakage process that occur once favourable conditions are met to cause the hydraulic failure.

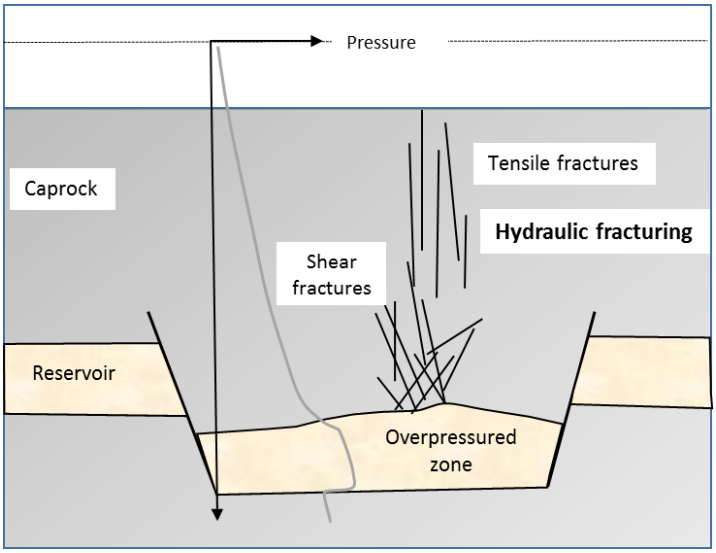


**Figure 3.8:** Sketch showing the hydraulic fracturing and leakage of fluids from the overpressured reservoir units and distinguishes between the two types of fractures. Redrawn from Lothe, (2004)

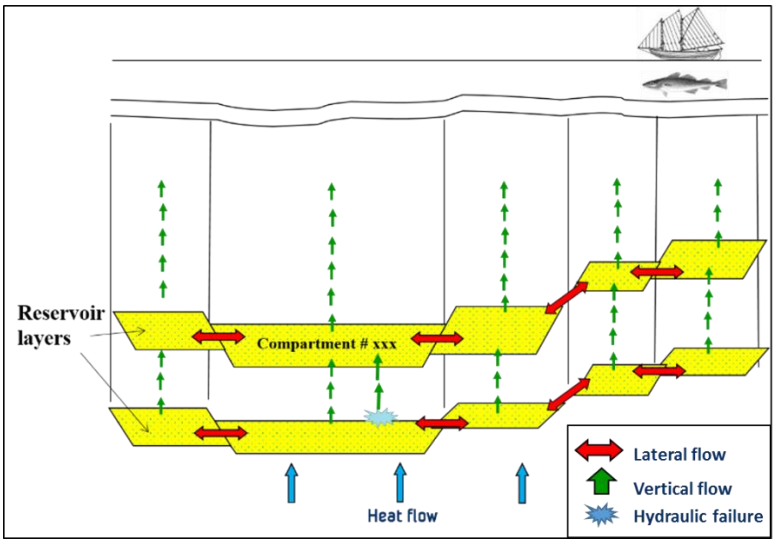


**Figure 3.9:** Descriptive model of the reservoir in cross-section view. Hydraulic failure of the reservoir is followed by the vertical leakage of the fluid out of the rock.

## 3.6 Minimum horizontal stress

The magnitude of minimum horizontal stress controls the timing of the hydraulic failures in the overpressured basin (Lothe, 2004). In the PhD study done by Lothe, (2004), she addresses different empirical or theoretical ways of calculating minimum horizontal stress. In that study, the results of these methods have been calibrated against datasets of leak off pressure (LOP) from the wells drilled in the study area. 'Leak-off test'(LOT) is usually carried out to assess the fracture strength of the rock unit immediately underneath the latest casing in a well (Bell, 1990; White et al., 2002). LOTs are performed at the well site by pumping mud into the borehole until the formation fractures and mud pressure variation and cumulative mud volume that enter the formation are measured (Bolås and Hermanrud, 2003).

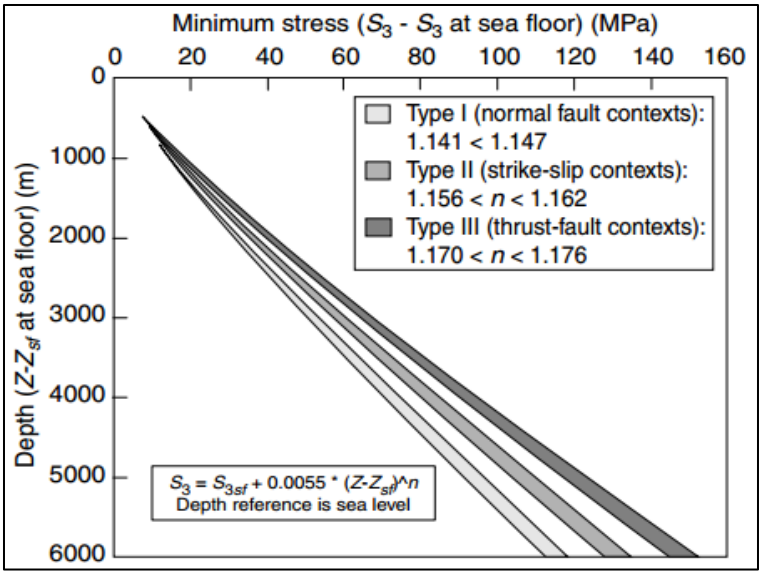


**Figure 3.10:** Evolution of minimum principal stress as a function of depth and tectonic stress regimes. $S_3$ and $S_{3sf}$ are the minimum principal stress values at depth Z and at sea floor $Z_{sf}$, respectively. The n exponent is dependent on the tectonic stress regime (Grauls, 1998).

The leak-off pressure (LOP) is reached when the increase in pressure with volume of mud pumped deviates from a linear relationship because the rock behaviour ceases to be elastic. LOP data are being used as a measure of least principal stress ($S_{Hmin}$) in this study. In her work, Lothe, (2004) concluded that the empirical approach presented by Grauls (1998) gives the best calibration of $S_{Hmin}$ with LOT. Therefore, Grauls (1998) method of calculating minimum horizontal stress until the top Stø Formation, have been applied in PRESSIM:

$$S_3=S_{3sf}+0.0055*(Z-Z_{sf})^n \qquad (3.1)$$

Here, $S_{3sf}$ is the minimum horizontal stress at the seafloor, $Z_{sf}$ is the depth of the seafloor and n is the power law function depending on the stress regime. The $S_3$ profile depends on the tectonic stress regime and exponent of n needs to be selected based on the basin tectonic regime among three types shown in Figure 3.10.

In addition to Lothe, (2004) several other studies (Addis et al., 1998; Okland et al., 2002; White et al., 2002) have done works to conclude that LOT is a good approximation for the minimum stress or fracture gradient along the depth.

## 3.7. Monte-Carlo simulation

In this study two parameters have been used for the Monte-Carlo simulation with a mean value and a standard deviation. For each simulation run, these two parameters are randomly and independently selected by using the given standard deviation constraints and the results are stored separately. After storing the results, the procedure is repeated:

1. Select new input values randomly.
2. Perform overpressure and leakage simulation run.
3. Store results

Iterative procedure is repeated until 1000 simulations have been run. It is enough number to build the probability distribution and do misfit analysis for the parameters varied in the Monte-Carlo simulation. One important aspect in this set-up is that simulation results can be weighted according to how well the iteratively modelled overpressure matches the pressure measured from the wells in the study area. The equation shows that the simulation results can be weighted depending on the measured pressures in wells. Each simulation run is weighted according to match the calibrated wells using the equation from Sylta & Krokstad., (2003), rewritten from hydrocarbon to pore pressure Lothe et al., (2008).

$$w_i = \frac{N}{\sum_{n=1}^{N} a_n (P_n^{\mathrm{mod}(i)} - P_n^{obs})^2} \qquad (3.2)$$

$w_i$, weight of simulation run number ‘i’

N, total number of calibration points

$a_n$, weight of importance of applied to each calibration points

n, wells

$P_n^{\mathrm{mod}(i)}$, is the modelled overpressure for wells ‘n’ in run ‘i’

$P_n^{obs}$, measured overpressures for calibration well for depth ‘n’

When the average difference between the modelled and measured overpressures increases, the weight of the simulations will decrease. An estimator for the most likely predicted pressure is Lothe et al., (2008).

$$P = \frac{\sum_{i=1}^{M} P^{\mathrm{mod}(i)} w_i}{\sum_{i=1}^{M} w_i} \qquad (3.3)$$

$w_i$, weight of simulation run number ‘i’

M, total number of simulations runs used

$P_n^{\mathrm{mod(i)}}$, is the modelled overpressure for run ‘i’

The weighting procedure done for this thesis is discussed further in chapter 6.2.

# 4. Data

## 4.1 Model setup and input data

Eight interpreted horizon surfaces (resolution 100x100), provided by Statoil, have been used to build the model. Pseudo-layers (Intra Sotbakken 10 and 34 Ma) were implemented for eroded sections in two different erosion periods: 40 to 35Ma and 10 to 2 Ma (Figure 4.1). These enabled the modelling of erosion in the given time steps. The present-day depth converted map of the top Stø Formation is used as the top of the reservoir unit (Figure 4.2), with interpreted faults. The fault traces were used to create closed compartments in a geologically reasonable manner. The small faults, which are not used in this process, were left inside the compartment as isolated traces and they had no impact in the pressure modelling. The depth-converted maps have been used to construct a decompacted burial history through time. These steps correspond to the age of stratigraphic horizons that are used to build the model. Table 4.1 shows the input table for the case study. Table 4.2 shows the dual lithology setting used in decompaction where sedimentary rocks are considered as a proportional mixture of two rock types.

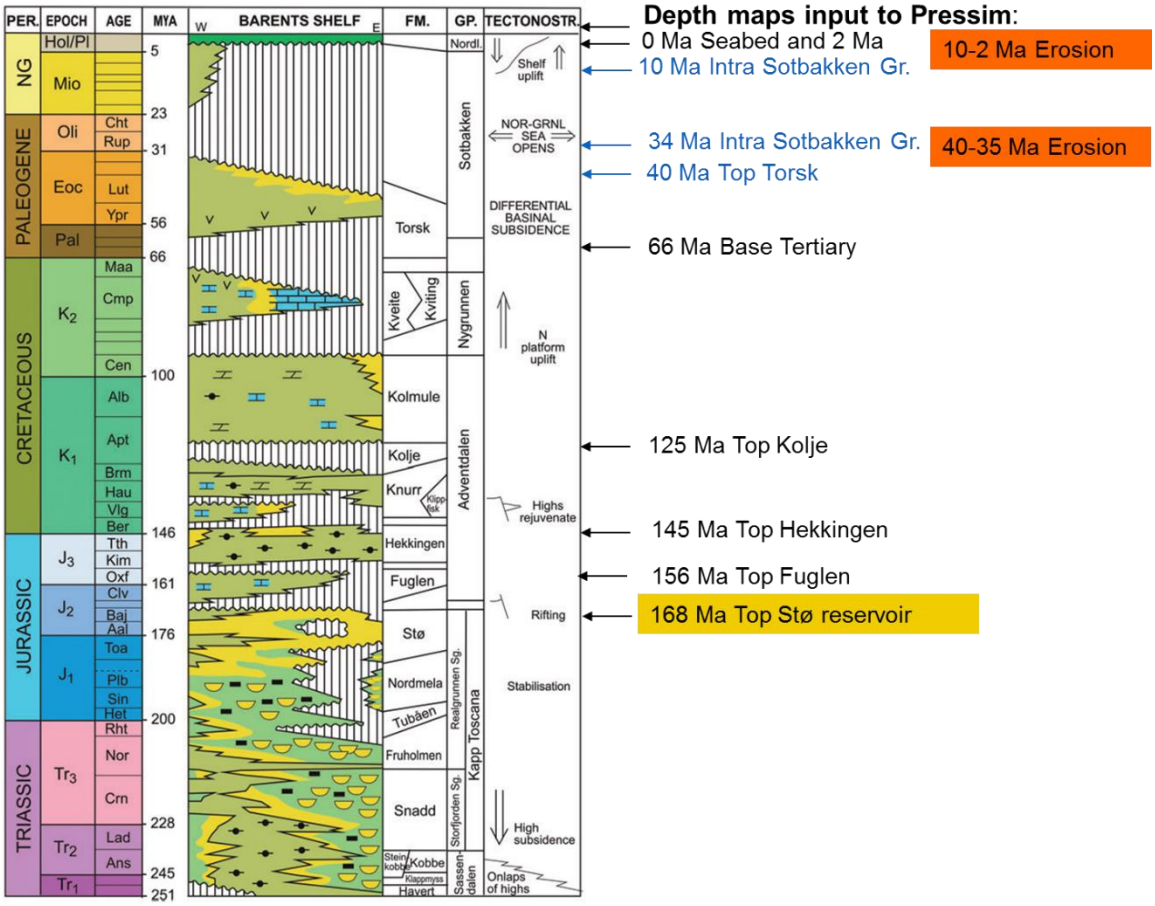


**Figure 4.1.** Interpreted seismic horizons used as input to the pressure modelling shown with black arrows. The blue arrow show the psedo-layers which are included to highlight the errored sections. Yellow filled box shows reservoir layer, orange boxes show the timing of erosion events. Reworked from Worsley, (2008), Nøttvedt et al.,(1993) , time scale; Gradstein et al., (2004).

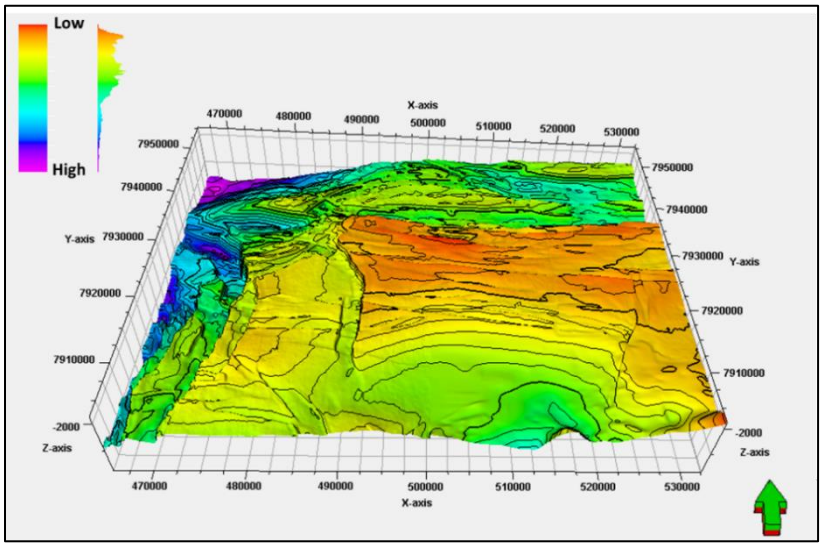


**Figure 4.2:** Top Stø surface map for the study area. Deeper part of the basin is seen to the west.

**Table 4.1**: Input datasets

| Input data | Pressim-water flow simulation |
|---|---|
| Depth-Converted seismic horizons | Seven time steps; 156 Ma, 145 Ma, 125 Ma, 66 Ma, 40 Ma, 34 Ma, 10 Ma, 2Ma and Present. |
| Isopach map reservoir | Stø Formation (183 Ma – 168 Ma) |
| Fault maps | Fault map at top Fuglen level |
| Pressure data | Overpressure calculation in Stø formation from 18 wells used for the calibration of the simulation. The wells are 7120/5-1,7120/6-1, 7120/6-2S, 7121/4-1,7120/7-1, 7120/7-2, 7120/7-3, 7120/8-1, 7120/8-3, 7120/8-2, 7120/8-4, 7120/9-1, 7120/9-2, 7121/5-2, 7121/7-2, 7121/7-1, 7121/4-2, 7121/5-1. |

**Table 4.2:** Dataset used for decompaction in Pressim. The decompaction is performed according to the porosity-depth relations of Sclater and Christie, (1980) which was set up for dual lithology.

| Stratigprahic Unit | Top age, Ma | Base age, Ma | Lithology 1 | Lithology 2 | Fraction* | Paleowater maps | Erosion Maps |
|---|---|---|---|---|---|---|---|
| Seabed | 2 | 0 | Shale | Sand | 0.4 | 0 - 2 Ma | |
| Base Quaternary | 10 | 2 | Shale | Sand | 0.3 | 2 - 66 | |
| Intra Sotbakken 10 | 34 | 10 | Shale | Sand | 0.3 | 2 - 66 | 10-2 Ma erosion |
| Intra Sotbakken 34 | 40 | 34 | Shale | Sand | 0.3 | 2 - 66 | |
| Top Torsk | 66 | 40 | Shale | Sand | 0.4 | 2 - 66 | 40-35 Ma erosion |
| Base Tertiary | 125 | 66 | Shale | Limestone | 0.2 | 2 - 66 | |
| Top Kolje | 145 | 125 | Shale | Limestone | 0.2 | 66 - 125 | |
| Top Hekkingen | 156 | 145 | Shale | Sand | 0.1 | 125 -145 | |
| Top Fuglen | 168 | 156 | Shale | Limestone | 0.1 | 145 - 156 | |
| Top Stø | 183 | 168 | Shale | Sand | 0.9 | 156 - 168 | |
| Top Nordmela | 197 | 183 | Shale | Sand | 0.8 | 168 -183 | |

* Fraction of 2nd lithology.

## 4.2 Input parameters to the simulator

The simulator uses the input parameters listed in Appendix A. After the seismic surface map and fault maps are interpreted, the next step was to import this depth map and fault traces into Pressim, prepare a fault segmentation map and give a number to each of the compartments (Figure 1.5). The number of compartments in the study area is 83. The fault traces are mapped on top of the Fuglen Formation. It is assumed that the faults of the Fuglen and Stø Formation are the same due to the very small thickness of the Fuglen Formation in that area. These fault traces define the lateral extent of the pressure compartments in a pressure simulator (Borge, 2000; Lothe, 2004) (Figure 4.3).

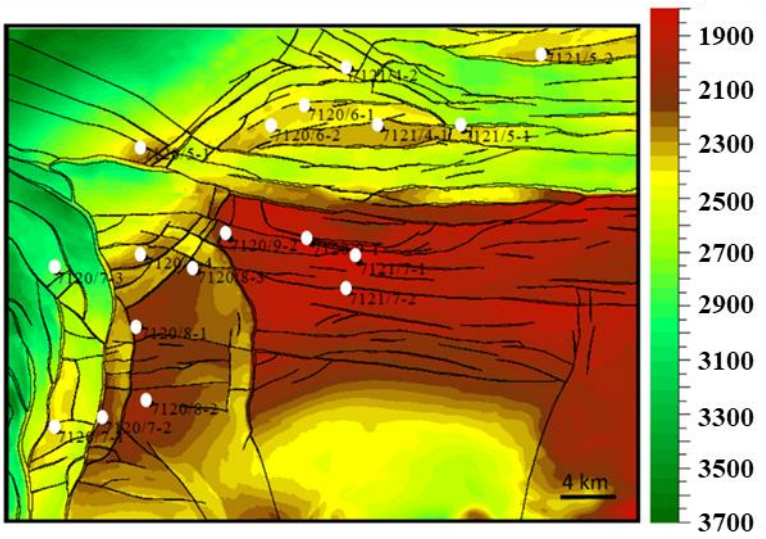


**Figure 4.3:** Present day depth (m) map of Top Stø (Pressim) with interpreted fault mapped from seismic data. White circles are the location of the wells used in the study.

## 4.3 Well data

Well data has been utilized for two major tasks in this study. First, it was used to calculate the overpressure of the wells to compare it with that coming from the model for a certain number of compartments. Second for the determination of the Grauls value (chapter 3.6), to calibrate the minimum horizontal stress.

### 4.3.1 Observed pressures in wells

Overpressure measured and observed in the Stø Formation and the Nordmela Formation has been collected from 18 wells in the study area. One well provides calibration for one compartment unless the compartment has several wells drilled into it. The overpressure calculation has been done based on the RFT (Repeat Formation Tester) data taken at the top of Stø Formation. The calculation of overpressure has been carried out manually by using a set of formulas. These are:

$$MFLTVD = Formation\ top(RKB) - Kelly\ Bushing \quad (4.1)$$

$$Overpressure = FP - (\rho_{fw} * g * MSTVD) \quad (4.2)$$

Here, MSLTVD is true vertical depth of the formation below mean sea level, RKB is the depth of the formation below the rotary kelly bushing, $\rho_{fw}$ is the density of formation fluid and FP is the formation pressure measured in bar. In this formula, Kelly bushing height, depth to the formation top and formation pressure comes from the NPD (Norwegian Petroleum Directorate) database for each well separately, and $\rho_{fw}$ is accepted as a constant, 1.1 g/cm$^3$. Table 4.3 shows the values of calculated overpressure in each well. Some of the wells are drilled into one compartments and their measured pressure is given as a range, in the table, for the pressure calibration of that compartments.

**Table 4.3:** Measured overpressure for all the wells used in the study area

| Well number | Measured overpressure, bar |
|---|---|
| 7120/5-1 | 6 |
| 7120/6-1, 7120/6-2S, 7121/4-1 | 4-10 |
| 7120/7-1 | 2-8 |
| 7120/7-2 | 4-11 |
| 7120/7-3 | 4 |
| 7120/8-1, 7120/8-3 | 3-11 |
| 7120/8-2 | 4-12 |
| 7120/8-4 | 0-3 |
| 7120/9-1,7120/9-2 | 4-9 |
| 7121/5-2 | 9 |
| 7121/7-2 | 9 |
| 7121/7-1 | 11 |
| 7121/4-2 | 9 |
| 7121/5-1 | 13 |

### 4.3.2 Modelled minimum horizontal stress calibration with Leak of Test (LOT)

The vertical stress is calculated in the simulator using:

$$\sigma_v = \rho g z \qquad (4.3)$$

where ρ is the density, g is the gravitational constant and z is the depth of burial.

The calculation of the minimum horizontal stress use empirical data to give a relationship between burial depth and the magnitude of the minimum horizontal stress (Chapter 3.6).

Figure 4.4 displays LOT data points coming from the well data in NPD. Each of these wells used in the study contain several measured LOT points as pointed out by the dots in the graph. The illustration between the simulated minimum horizontal stress and LOT points will be given separately in the upcoming chapter. Based on Figure 4.4, Shmin has been simulated by varying the value of Grauls number (n- exponent in equation 3.1) so that the modelling results can be compared with the LOT data points.

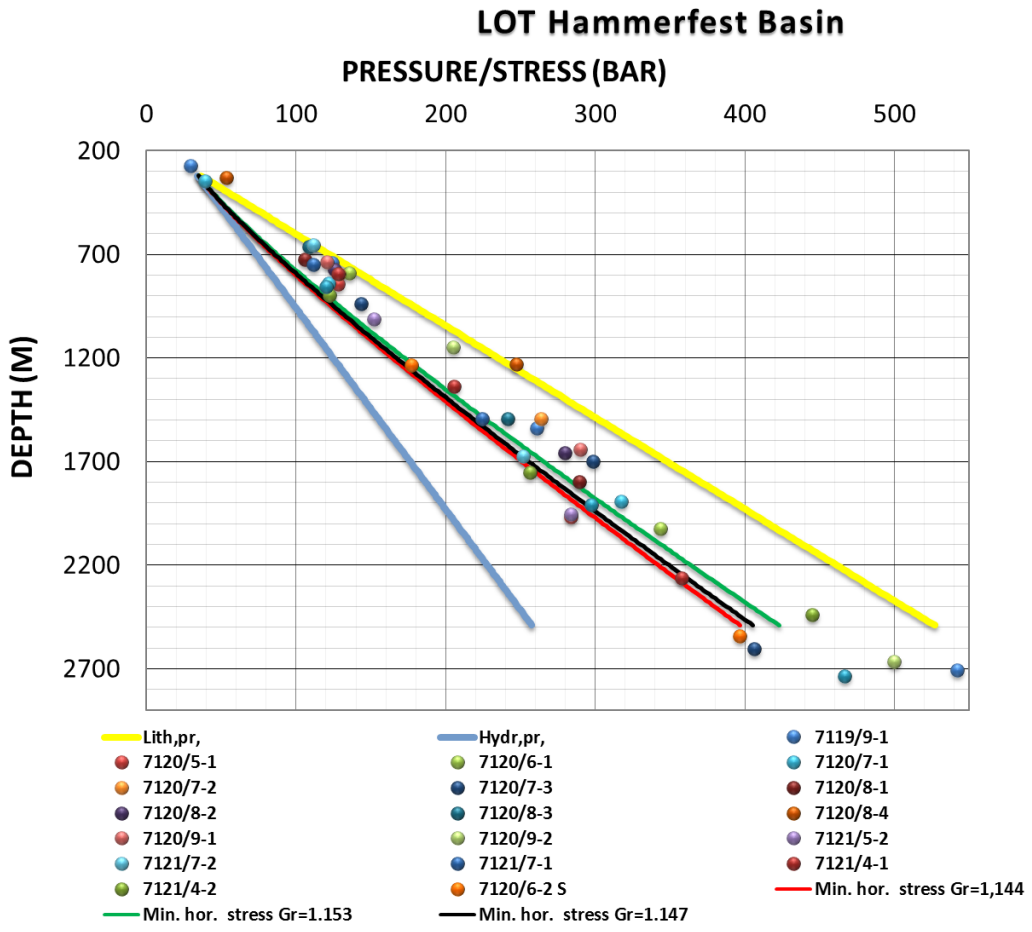


**Figure 4.4**: Calibration plot between the LOT and $S_{Hmin}$ by using three different values of Grauls number. Minimum horizontal stress is modelled for the compartment 65. The plot also includes hydrostatic and lithostatic pressure measurements modelled along the depth. LOT points are colour coded based on the name of the well.

## 4.4 Erosion scenarios

Two different erosion scenarios have been tested in this study. The first erosion scenario has been adopted from Baig et al, (2016) where several techniques of exhumation estimation were used, namely seismic shot gathers, VR, and sonic log data which had been averaged to produce the final erosion map. Figure 4.5 illustrates the part of the map crossing the study area in Pressim.

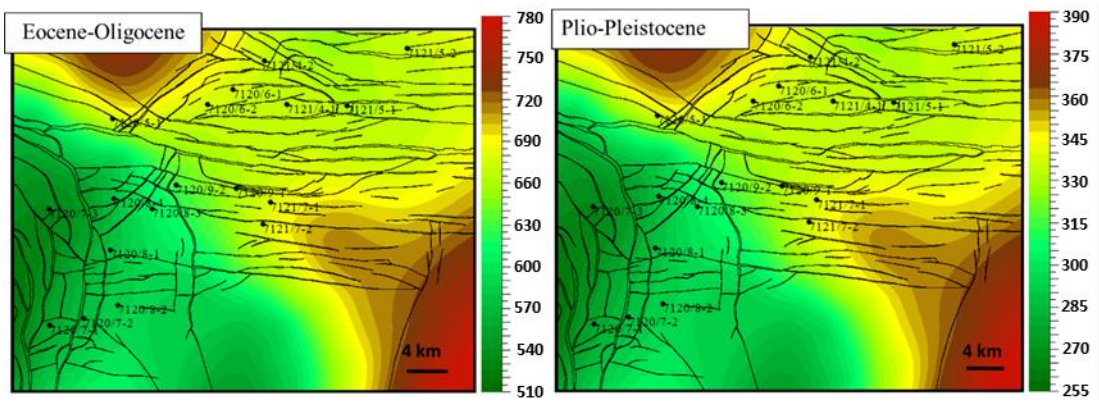


**Figure 4.5:** Total erosion map of Baig er al., (2016) divided into two parts. The left map shows the first erosion period from 40-35 Ma and its magnitude is two times larger than that on the right. The right map shows the amount of erosion from 10 – 2 Ma.

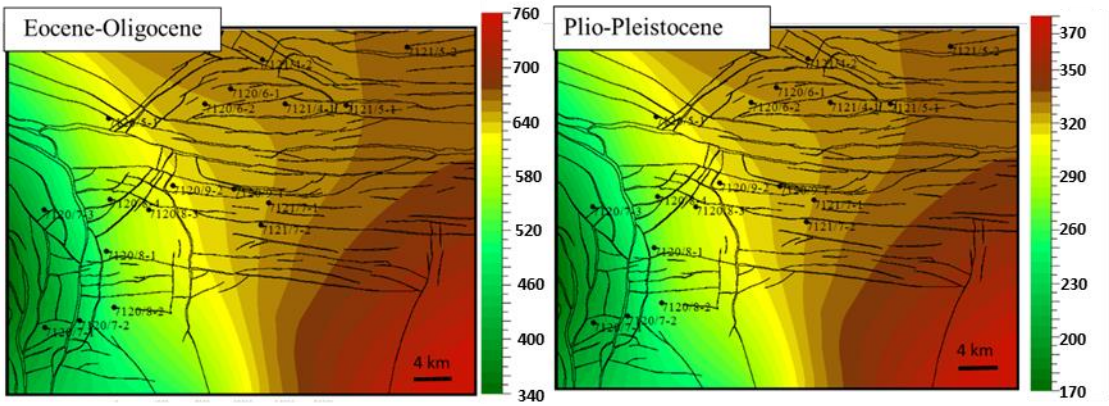


**Figure 4.6:** Total erosion map of Henriksen et al. (2011) divided into two parts. The left map shows the first erosion period from 40-35 Ma and its magnitude is two times larger than that on the right. The right map shows the amount of erosion from 10 – 2 Ma.

The second scenario is published by Henriksen et al., (2011).They also use the similar approach of combining several data sources to produce the final erosion map. The aim of using several methods (where available) is explained as to reduce the standard deviation in net erosion estimates. Only two contour lines are located in the areal focus of this study since the map produced by them had a big areal coverage in the Barents Sea. Figure 4.6 illustrates this map.

## 4.5 Shale permeability

There are two permeability related parameters that are influencing the leakage history of the basin. First one is surface permeability (permeability at zero depth or at seabed – $k_0$) and second one is the change of permeability with depth known as permeability exponents. Both of these parameters helps to describe the permeability at the cap-rock level overlying the Stø reservoir rock. Hence, they have been selected to be tested in this study despite of the difficulty with their determination.

Different values have been tested by using the model given in Figure 4.7. At the ocean floor the permeability of the shale corresponds to the permeability of the unconsolidated rock. In this study, permeability at the sea floor has been determined to be 10 mD as the base case which corresponds to the $10^{-14}$ $m^2$ – a typical permeability for the unconsolidated shales. Assuming the c value as 9 resulted with permeability for the cap-rock at $10^{-7}$ mD ($10^{-22}$ $m^2$) (around 2300 m depth).

Permeability models in Figure 4.7 have been built by using two input parameters: $k_0$ and c. In order to see the influence of these parameters on the pressure and leakage, three different scenarios for the c value and k value have been tested in the single run simulations. The base case values are used as an "intermediate" case and the other two parameter sets have been selected to create very "open" and "closed/tight" rock models for the shale.

A detailed discussion of this will be covered in the following chapter (Chapter 5.3).

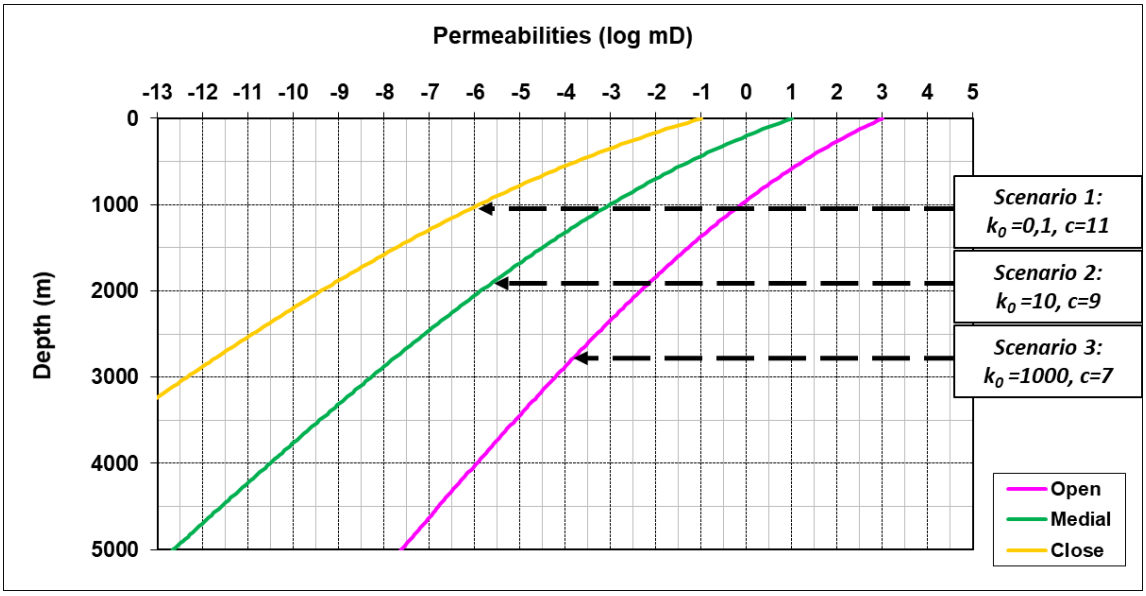


**Figure 4.7:** Different models of permeability. Horizontal axis shows the initial permeability at the seabed in the exponents of milli-darcy. Vertical axis shows the depth.

The formula for the calculation of permeability with depth is given below (Yang and Aplin, 2010):

$$k=k_0(\frac{e}{e_0})^c \qquad (4.4)$$

$k_0$ – shale permeability at surface

e – void ratio

c – shale permeability exponent

This is the formula that had been implemented in the model to track the change of permeability with depth. Yang and Aplin (2010) estimated the permeability of mudstones based on the measured pore throat size distribution plus assumed pore alignments and pore shapes.

## 4.6 Burial history

There are two erosion episodes modelled in this work (Figure 4.1). The lack of the accepted magnitude division between these erosion episodes made it necessary to analyse the influence of the burial history in the overpressure modelling. The three burial history scenarios will be tested in Chapter 5.5.

# 5. Results of overpressure modelling

This chapter will demonstrate the results varying single parameters on the overpressure build up and distribution. The effect of varying the minimum horizontal stress, shale permeability, erosion scenarios and burial history will be tested. The importance of single run simulation, is to help to define the uncertainty range and the mean value for the parameters to be varied in the next stage in Monte-Carlo analysis. There is a base case set of parameters which had been identified after several runs. The base case values of parameters will be kept constant while one of them is being tested at the time. This helps to see the distinct influence of each parameter on the overpressure. Figure 5.1 shows the overall workflow followed in this thesis including all the parameters tested both in the single run sensitivity analysis and Monte -Carlo simulation.

Table 5.1 illustrates the all the scenarios, in terms of Grauls number and shale permeability, that are going to be tested in this chapter.

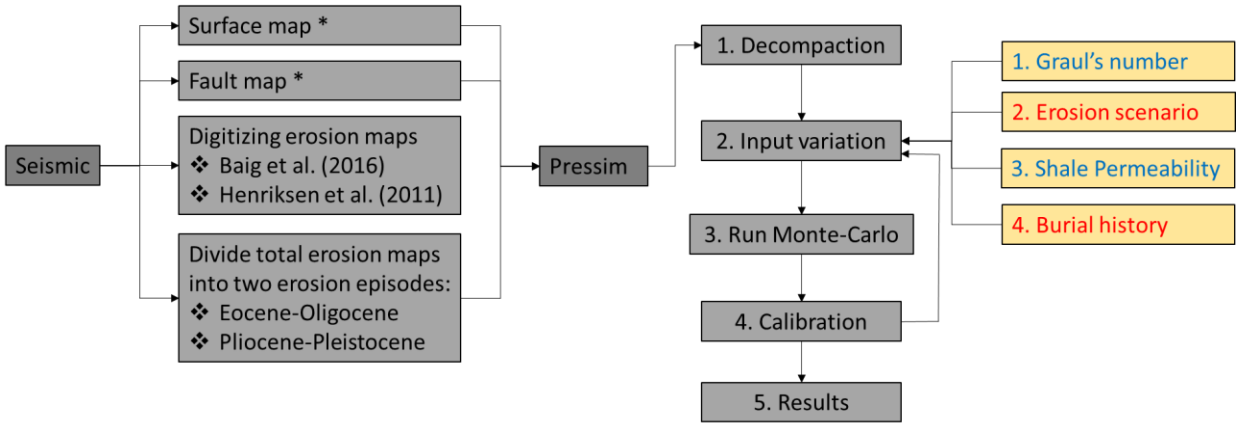


* Default input into the study

**Figure 5.1:** Flowchart showing the overall workflow followed in this thesis together with all the methods used. Yellow box shows the varied parameters in terms of single sensitivity analysis (1,2,3,4) and in terms of Monte-Carlo analysis (1 and 3)

**Table 5.1:** Grauls number and permeability parameters change based on which scenario that has been run. Grauls number and shale permeability are constant (base case) for the scenarios that are testing parameters other than these two.

| Model | Grauls number | Shale surface permeability and permeability (mD) exponent |
|---|---|---|
| Grauls number – Scenario A (base case) | 1.144 | $k_0$=10, c=9 |
| Grauls number – Scenario B | 1.149 | $k_0$=10, c=9 |
| Grauls number – Scenario C | 1.153 | $k_0$=10, c=9 |
| Permeability - Tight seal | 1.144 | $k_0$=0.1, c=11 |
| Permeability – Medial (base case) | 1.144 | $k_0$=10, c=9 |
| Permeability - Open seal | 1.144 | $k_0$=1000, c=7 |
| Erosion scenario - (Henriksen et al., 2011) | 1.144 | $k_0$=10, c=9 |
| Erosion scenario - (Baig et al., 2016) (base case) | 1.144 | $k_0$=10, c=9 |
| Burial history (ratio 1:2) – Scenario D | 1.144 | $k_0$=10, c=9 |
| Burial history (ratio 4:1) – Scenario E | 1.144 | $k_0$=10, c=9 |
| Burial history (ratio 1:4) – Scenario F | 1.144 | $k_0$=10, c=9 |

**Table 5.2:** All the input parameters used in the base case scenario

| Scenario | Grauls number | Permeability | Erosion scenario | Burial history |
|---|---|---|---|---|
| Base case | 1.144 | $k_0$=10, c=9 | (Baig et al., 2016) | ratio 2:1 |

## 5.1 Analysis of the base case scenario

The base case scenario is simulated with the given set of parameters, see Table 5.2 and Appendix A. One of the major output of the simulation studies is the distribution of overpressure both along the geological time axis for a specific compartment and overpressure distribution maps for the nine time steps. The overpressure modelling is done for every 10000 time steps but the simulator is only able to display overpressure distribution maps for the study are for nine time steps in the geological history. Figure 5.2 shows the change in the overpressure for the compartment 65, where the Snøhvit field is located, in the northern part of the study area.

Uplift and erosion is assumed to take place from 40 Ma till 35 Ma and from 10 - 2 Ma. This is shown for the burial depth, and mirrored for the pressures. The uplift lead to a rapid reduction in the overpressures at 40 Ma for the Snøhvit Field (compartment 65; Figure 5.2). Orange trend in the figure shows the advancement of the burial history for the top Stø Formation including the

erosion episodes and their magnitude. It illustrates that simulated overpressure started to emerge and increase from 66 Ma till 40 Ma where it reaches the peak values of 130 bar at some compartments. Generally, the maximum overpressure attained at this period is on the north-western corner of the study area (see map at 40 Ma). This high overpressures leads to hydraulic fracturing and leakage through the caprock above the reservoir as illustrated in Figure 5.4b.

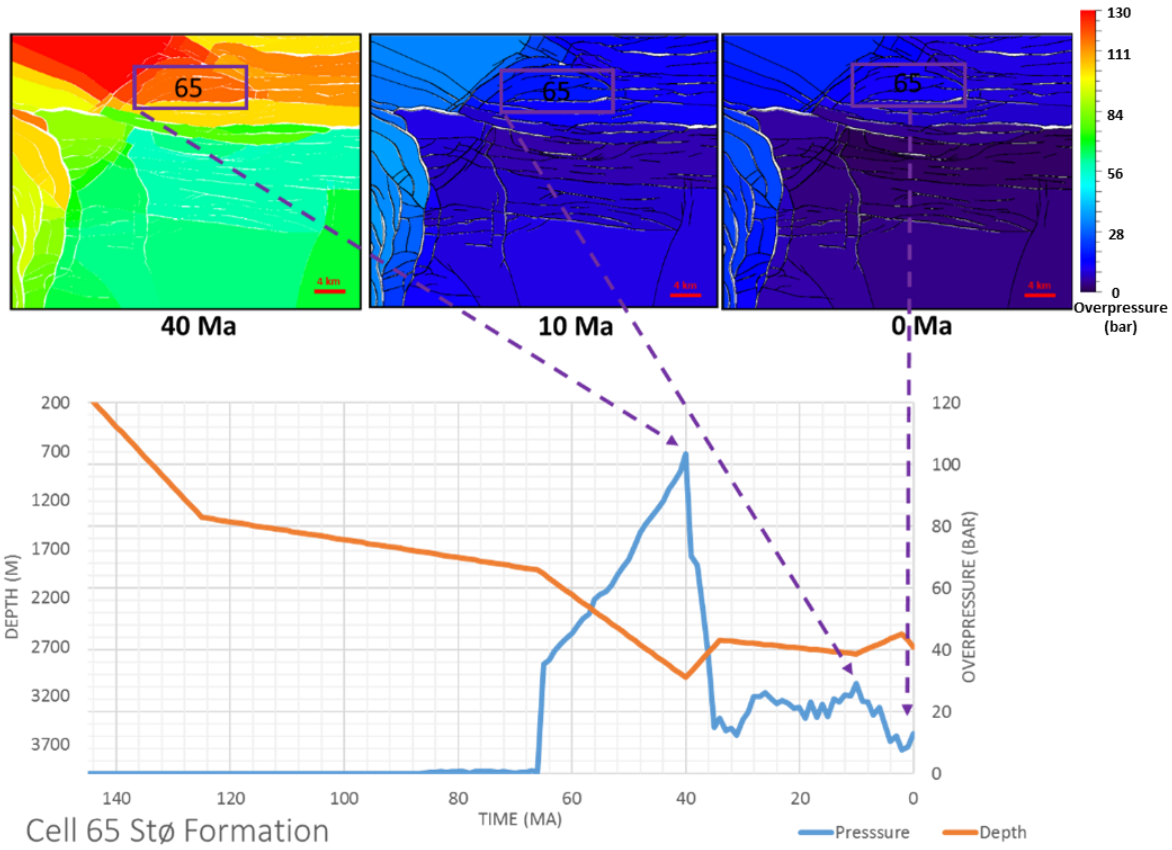


**Figure 5.2**: The graph describes the changes in simulated overpressure and burial history over 145 – 0 Ma for the compartment 65. The three modelled overpressure maps show the pressure distribution at 40, 10 Ma and Present. Highlighted box shows the location of compartment 65 on the map.

Only three compartments show the leakage. Two of them are located on the north-west part and one in the eastern part of the study area. The timing of leakage corresponds to the period of geological history where maximum overpressure is observed. Leakage of this base case will be discussed further in the following sub-chapter. At 40 Ma, modelled overpressure is ranging from 50 to 80 bar in the central, south and south-eastern part of the study area. With the initiation of the first erosion episode (40-35 Ma), overpressure plummeted down to the level of 20 bar for the compartment 65. After the first erosion period ends at 35 Ma, overpressure generation started to intensify and the second period reached peak pressure value of 32 bar for this compartment at 10

Ma. Due to the ongoing erosion starting from 10 Ma, pressure was released and reached 18 bar by the end of erosion episode at 2 Ma. At present, pressure is nearly hydrostatic in the central compartment and to the south, south-eastern part of the study area.

Figure 5.3 helps to relate the generated overpressure on the western direction at 40 Ma, to the two different sources namely mechanical compaction and quartz cementation. A rapid burial rate in Figure 5.2, and quartz cementation in Figure 5.3c caused this massive pressure build up for the compartment 65 at 40 Ma. The depth of the compartments on the western part is relatively deeper compared to the central area (Figure 5.3a**)**. As mentioned earlier, mechanical compaction will be the dominant pressure generation process down to approximately 2 km depth. At deeper burial depths, quartz cementation (chemical compaction) will be the dominating pressure generating process. The Figure 5.3c shows the degree to which type of compaction is responsible for overpressure build up for each compartment. The high porosity values and shallower depth in the central part of the study area explains why the nearly hydrostatic pressure regime is dominant in this part of the map.

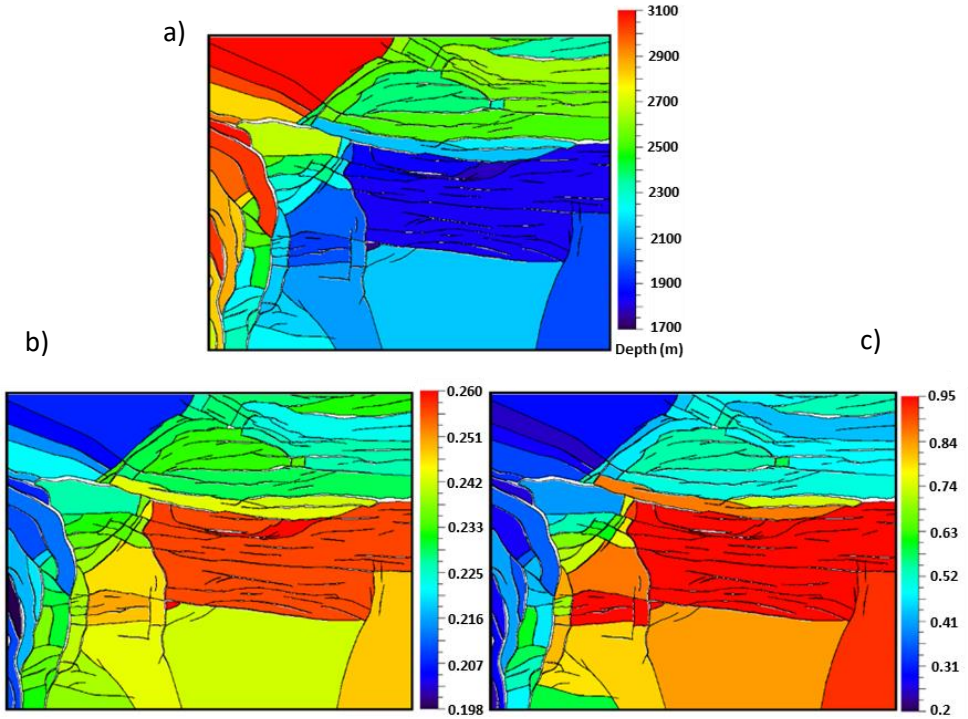


**Figure 5.3:** (a) Mean depth (burial depth) to each compartment shows that the deepest compartments are located on the north-west and western part of the study area, (b) modelled porosity distribution map shows that the central compartments with the shallower depth are having higher porosity due to the lack of intensive shale compaction that can be observed from (c). This last figure (c) shows the fraction of overpressure generated due to the shale compaction.

## 5.2 Vary the magnitude of the minimum horizontal stress

Simulated minimum horizontals stress using Grauls, (1998) is compared to the measured stresses from LOTs in wells, assuming that LOT can be used as equivalent to the minimum horizontal stress at a certain depth. Thereafter the modelled pressure is compared to the present-day pressure measurements from wells. In Figure 4.4 several values of Grauls number (see equation 3.1), that define the magnitude to minimum horizontal stress versus depths, have been identified in order to be varied in single run simulations.

Figure 5.4 illustrates the outcome of the overpressure modelling once the different values of Grauls number (*n*) are being used. The maps on the right side of the figure illustrates the amount of cumulative leakage due to hydraulic leakage that is modelled from the compartments in the study area for the different scenarios, respectively.

Graphs on the left side of Figure 5.4 demonstrates how the simulated minimum horizontal stress matches with the LOT data with the change of *n* value. The lowest minimum horizontal stress is modelled in scenario A, medium in scenario B and the highest minimum horizontal stress in scenario C (Figure 5.4 a, c & e). The LOT versus simulated $S_{hmin}$ calibration is done for the Snøhvit field, situated in compartment 65, which is highlighted in all the leakage maps (Figure 5.4). There is an obvious change in the number of leaking compartments from three to one and to two, when larger magnitude of minimum horizontal stress is used as an input. Figure 5.4b shows the resulting leakage map when the lowest value of Grauls number (1.144) is being used. In this scenario A, simulated minimum horizontal stress causes leakage of three compartments, two of them located on the north-western (compartment 66 and 70) part and one on the eastern part of the study area (compartment 55). In the case of scenario B, Figure 5.4d shows that the only compartment 66 is leaking. However, the amount of leakage for this scenario is the highest among all three scenarios based on the unified colour scale. In Figure 5.4f the number of leaking compartments increases to two. From the evaluation of maps, one would expect compartment 70 to leak in the scenario B (Figure 5.4d) too, since it leaks in the other two scenarios. The reason of this non-leaking is that when compartment 66 stars to leak it leads to a loss in accumulated overpressure. Hence, leakage from one compartment creates a critical influence on the other compartments. None of the compartments exhibited any failure once the value of 1.154 and higher is used for the simulation. This happens when the minimum horizontal stress is big enough to prevent the failure of the rock by avoiding the interaction between the Mohr Circle and Griffith-Coulomb failure envelope.

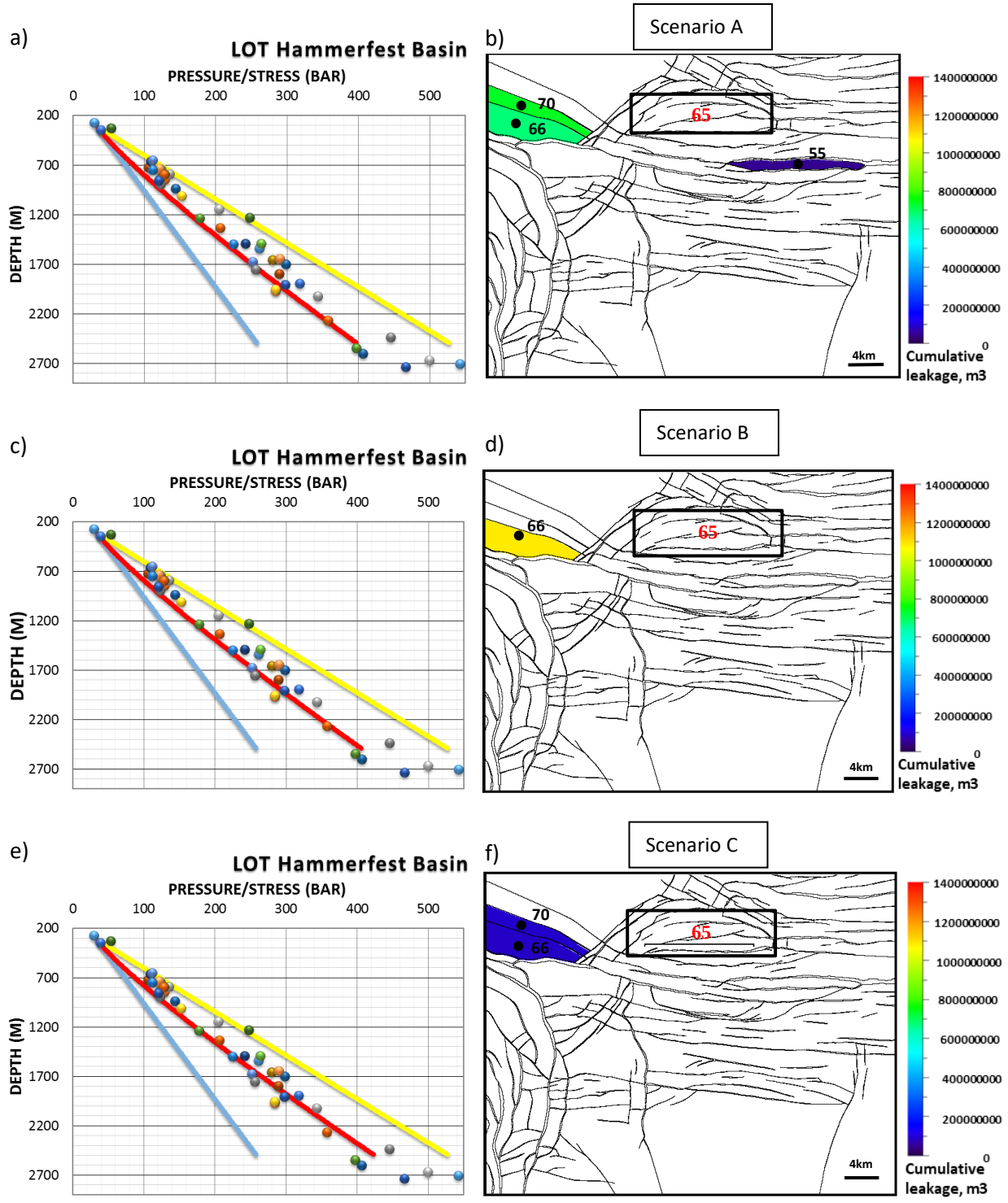


**Figure 5.4**: (a), (c) and (e) show simulated hydrostatic pressure (blue line), vertical stress (yellow line) and minimum horizontal stress (red line) versus depth in the study area when Grauls number is (a) n=1.144, (c) n=1.147 and (e) n=1.153 compared with the measured LOT data from the wells. (b), (d) and (f) shows cumulative amount of leakage over geological time (145-0 Ma) for n=1.144 , n= 1.47 and n=1.153 respectively. No leakage is modelled in the Snøhvit field (compartment 65) in these runs.

Figure 5.5 shows the difference in simulated leakage pulses that took place for compartment 66 for the different scenarios. This comparison has been done for the compartment 66 since it is the only compartment that leaks for all the scenarios. Highest leakage rate has been observed for the scenario B and it happened with continuous pulse over a certain geological time, similar to the scenario A. The timing of leakage in these two scenarios corresponds to the first large overpressure build up period of 66-40 Ma. However, leakage happened as one single pulse for a shorter time when the highest simulated value of Grauls number (1.153) used in the modelling and the timing of leakage corresponds to the 44-40 Ma.

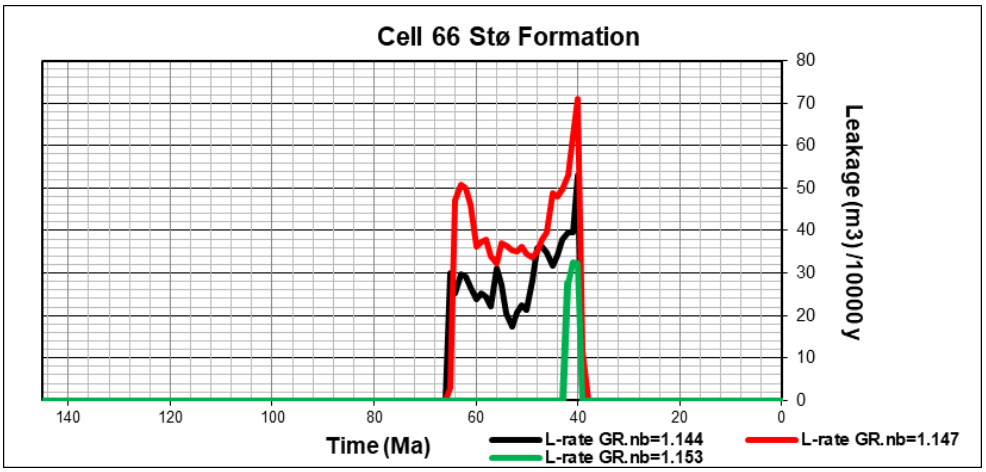


**Figure 5.5:** Comparison of the leakage rate (L-rate, $m^3/10000$) of fluid in compartment 66 for each of the three scenarios described above.

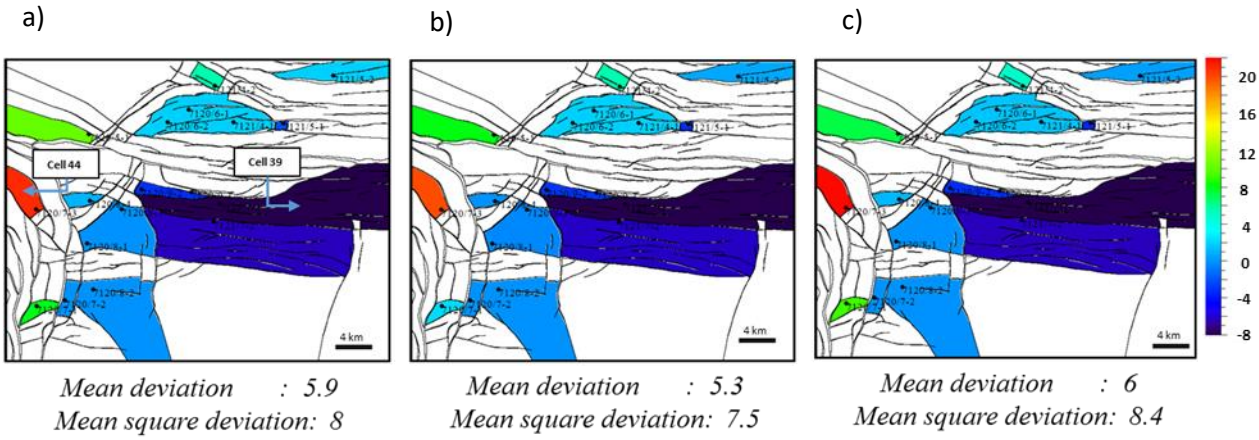


**Figure 5.6:** Pressure deviation maps between the modelled and measured pressure for the three scenarios of Grauls number, (a) n=1.144, (b) n=1.149, (c) n=1.156. The Hammerfest area shows low deviation (+/- 6 bar). In the western part (part of Tromsø Basin) larger deviation is modelled (up to 22 bar).

The reasonable value of Grauls number should also give the least amount of deviation between the modelled and measured overpressure. The calibration maps in Figure 5.6 have been illustrated, each with its own mean and mean square deviation. Although the deviation in pressure is lowest in the scenario B, the values are very similar to each other in magnitude.

Table 5.3 shows how the deviation in pressure between the measured and calculated overpressure, for each of the pressure calibrated compartments, changed with the change of the scenario A, B & C. The largest deviations occurred for the compartments 44 and 39 due to the several reasons that will be discussed in Chapter 7. Thus, it is expected that the calculation of mean pressure which is given at the end of table for each scenario is mostly affected by these two compartments. The location of these compartments is given in Figure 5.6a.

**Table 5.3:** Deviation in overpressure for each compartment in different scenarios.

| Wells used in the calibration study | Compartment name | Grauls number n=1.144 | Grauls number n=1.149 | Grauls number n=1.153 |
|---|---|---|---|---|
| | | Deviation, bar | Deviation, bar | Deviation, bar |
| 7120/5-1 | 66 | 10.2 | 9.1 | 7.3 |
| 7120/6-1, 7120/6-2S, 7121/4-1 | 65 | 1.9 | 1.6 | 1.5 |
| 7120/7-1 | 10 | 7.9 | 7.7 | 9.1 |
| 7120/7-2 | 11 | 0.0 | 0.0 | 0.0 |
| 7120/7-3 | 44 | 21.0 | 20.6 | 22.1 |
| 7120/7-3, 7120/8-3 | 26 | 0.0 | 0.0 | 0.0 |
| 7120/8-2 | 12 | 0.0 | 0.0 | 0.0 |
| 7120/8-4 | 37 | 1.0 | 1.3 | 1.1 |
| 7120/9-1, 7120/9-2 | 41 | -3.1 | -3.1 | -3.1 |
| 7121/5-2 | 79 | 1.9 | 0.7 | 0.4 |
| 7121/7-2 | 35 | -6.3 | -6.3 | -6.3 |
| 7121/7-1 | 39 | -9.2 | -9.2 | -9.2 |
| 7121/4-2 | 78 | 5.7 | 5.3 | 5.0 |
| 7121/5-1 | 67 | -2.1 | -2.9 | -3.4 |
| Mean deviation | | 5.9 | 5.8 | 6.0 |

## 5.3 Vary the shale permeability

The permeability to the shales in the overburden varies with depth (Chapter 4.5) due to the mechanical compaction process. In this chapter three models that have been built by varying the surface permeability of the unconsolidated shale ($k_0$) and permeability exponent (c), in Equation 4.4. Parameters of these models are given in Figure 4.7**.** Each of these three scenarios will run different sets of two parameters ($k_0$ and c) to evaluate the overpressure history in the basin. Grauls number that had been analysed in the previous chapter will be kept as 1.144 (constant) for the remaining simulations carried out in this in this thesis.

The formula given by Yang and Aplin, (2010) in Chapter 4.5 shows the mathematical relationship between the surface permeability and permeability at depths. Therefore, the permeability scenarios will focus on the variation of the surface permeability and permeability exponent, to model how the shale permeability changes versus depth.

The shale permeability scenarios are named:

- Open - where higher than normal surface shale permeability value is applied
- Tight - where lower than the normal shale surface permeability is applied
- Base case - medial shale permeability

Figure 5.7 illustrates the leakage maps and the leakage rate for the corresponding compartments in each of the modelled permeability scenarios. To start with the “Open” seal rock, it leads to the dissipation of generated overpressure, and few compartments fails (Figure 5.7b). Leakage from compartments on the north-western part of the study (66 and 70) took place, as one continuous pulse, from 68 Ma till 39 Ma (Figure 5.7a). The timing of failure initiation for these compartments (66 and 70) does not differ for the tight and open cases (Figure 5.7a & c).

In the open and medial permeability scenarios, leakage stops at 40 Ma with the onset of erosion, however, compartments continue to leak till 37 Ma in the tight scenario. This can be due to the late healing process of the fractures. In addition, there is a variation in the leakage rates for compartment 66 and 70 in the different scenarios (Figure 5.7a, c & e). The highest leakage rates for both compartments 66 and 70 is observed in the tight shale model. It was over 60 $m^3$ for compartment 70, just below 60 $m^3$ for compartment 66 (Figure 5.6c).

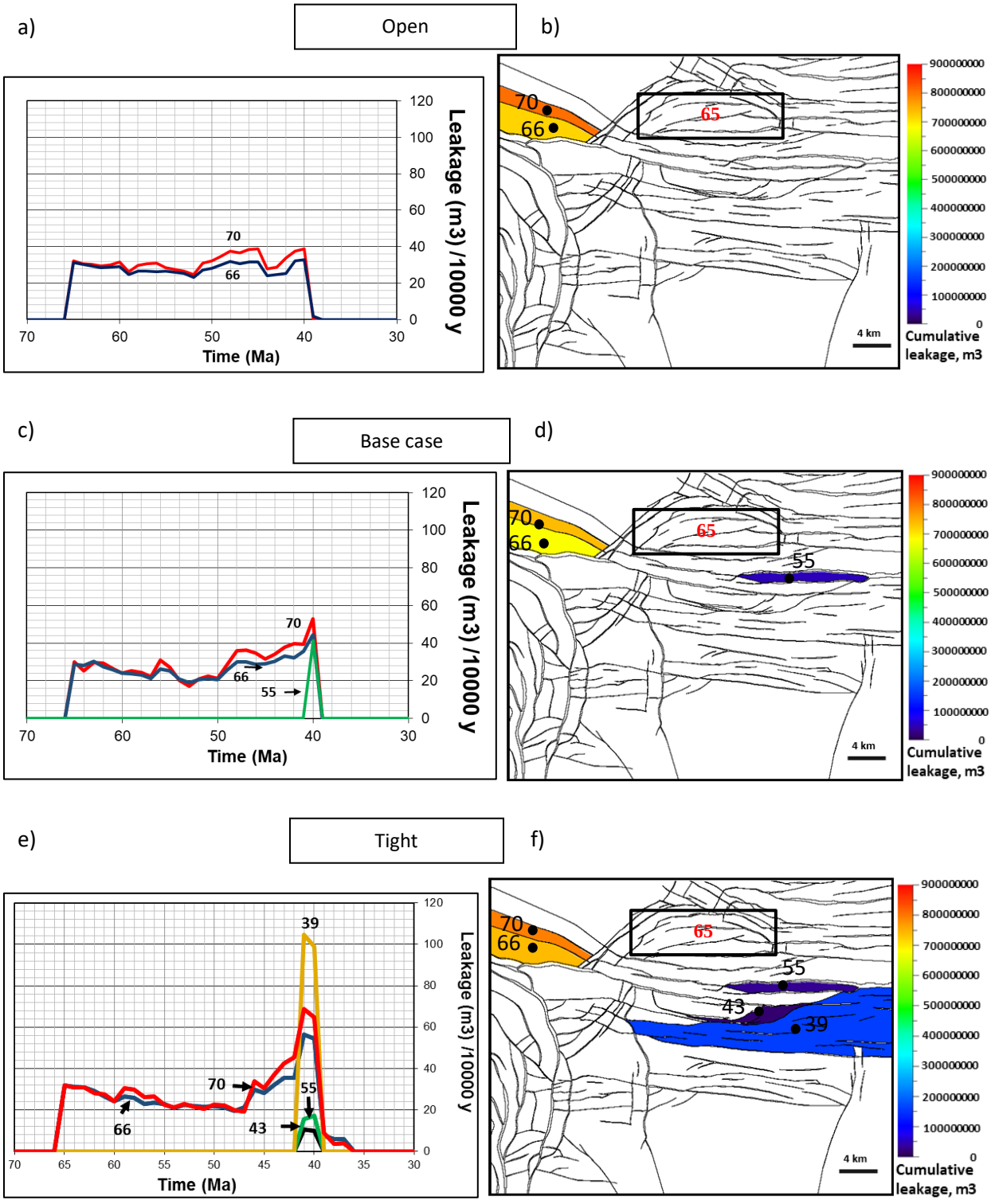


**Figure 5.7:** Leakage rate ($m^3$/10000 years) and timing of leakage in different pressure compartments for three different scenarios of surface permeability and exponent, a) $k_0$=1000 mD, c=7 (open); c) $k_0$=10 mD, c=9 (base case), e) $k_0$=0.1 mD, c=11 (tight). The maps b), d), f) are corresponding cumulative leakage maps in the study area. The scale on the maps shows cumulative leakage to present day ($m^3$). No leakage is modelled in the Snøhvit field (compartment 65) in these runs.

Leakage for the compartments 55, 43 and 39 is observed to be a sudden pulse that went on for 3 Ma (Figure 5.7e). Compartment 55 failed in the base and tight cases whereas compartment 43 and 39 fails only in the tight shale case scenario. All these three compartments started to leak at a later time than compartment 66 and 70.

In the base case, compartment 55 leaked from 40 to 39 Ma, however leakage started 1 Ma earlier for this compartment in the tight case. Compartment 55, 43 and 39 all started and stopped leakage at the same time in the tight case. Compartment 39 distinctly differs from the other compartments due to its large size (Figure 5.7f) and it experienced a leakage only for a short time interval (Figure 5.7e). This can be the reason of leakage rate of nearly 100 $m^3$ per ten thousand year which is the highest rate modelled among the all three shale permeability scenarios. The fact that failure has happened relatively late for this compartment can also lead to such a sudden pulse of leakage, followed by the accumulated large overpressures.

Figure 5.8 illustrates the cumulative leakage versus time for each of the leaking compartments. The total amount of leakage for compartment 70 is always simulated to be higher than that of 66. In this figure, cumulative leakage for the same cases and for the respective leaking compartments have been calculated. The results for the base case showed that highest cumulative leakage took place from compartment 70 in the north-western area and least cumulative leakage from the compartment 55 in the south-eastern area. There is a progressive reduction in the total amount of cumulative leakage when comparing compartment 55 in the second and third scenarios. This is also observed for the compartment 66. The reason can be due to the initiation of failure in compartment 39 which reduces amount of accumulated overpressure in compartment 55. Similar history happened for compartment 66 but this time due to the increase in the amount of leaked fluid in compartment 70.

In Figure 5.9, modelled overpressure build up for all the scenarios in compartment 70 and 66 shows that there is no obvious change in the magnitude of overpressure due to the change of cap-rock permeability. One would expect to see increase of overpressure as the scenarios changes from one to three because as the shale rock gets tighter it traps more and more generated pressure. However, it is possible to explain the lack of this trend with the leakage process. As the compartments initiated hydraulic fracturing of the shale rock, accumulated overpressure started to get released for all the scenarios. Thus, ongoing leakage process does not let overpressure to exceed the certain threshold. In addition, simulated overpressure, for the all scenarios, is relatively higher for the

compartment 70 than compartment 66 which would explain the why leakage rate in compartment 70 is higher since high overpressures trigger the larger hydraulic leakage.

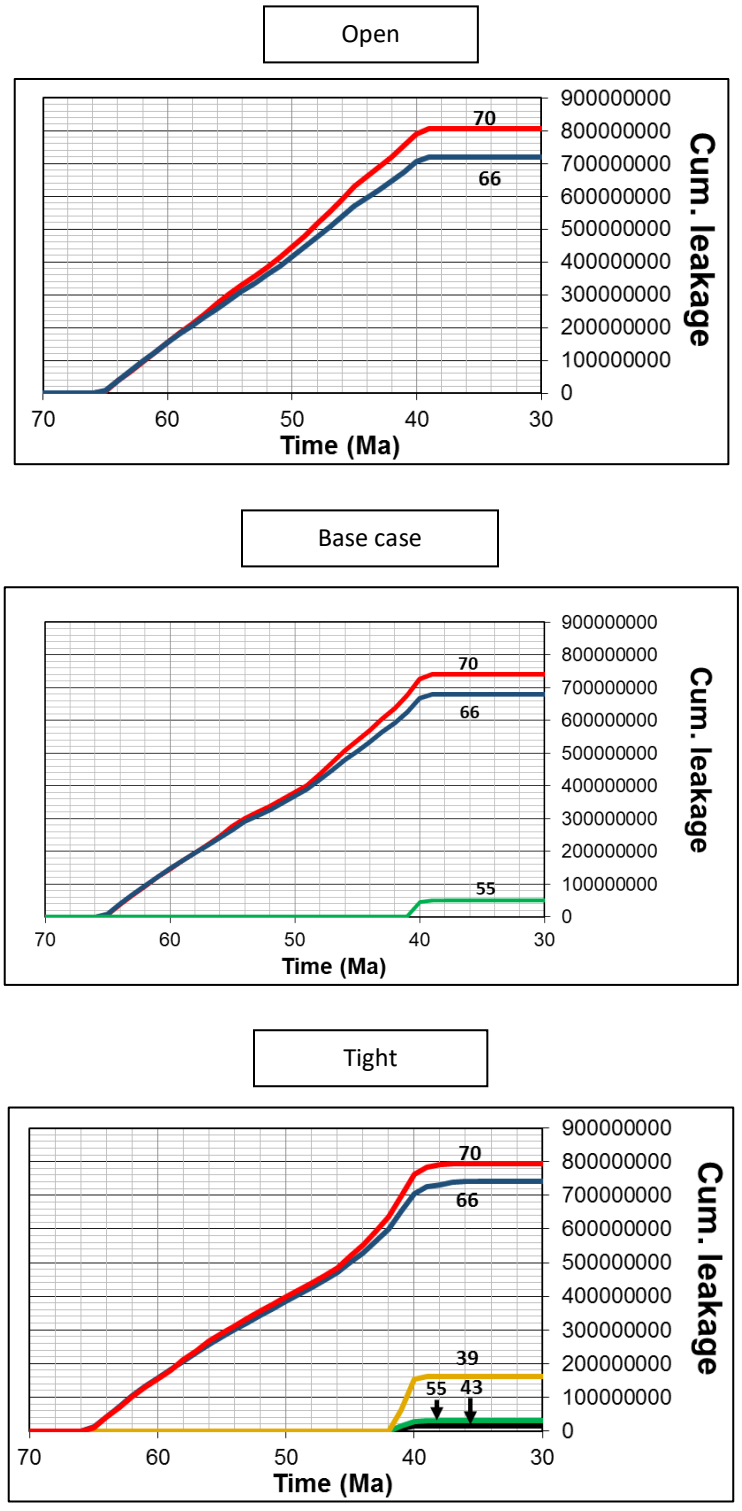


**Figure 5.8:** Cumulative leakage ($m^3$) in each compartment for the three permeability scenarios.

Comparison in the timing of overpressure and leakage based on Figure 5.8 and Figure 5.9 shows that maximum leakage has been modelled once the overpressure reached the maximum value, before the onset of the first erosion episode, at approximately 40 Ma.

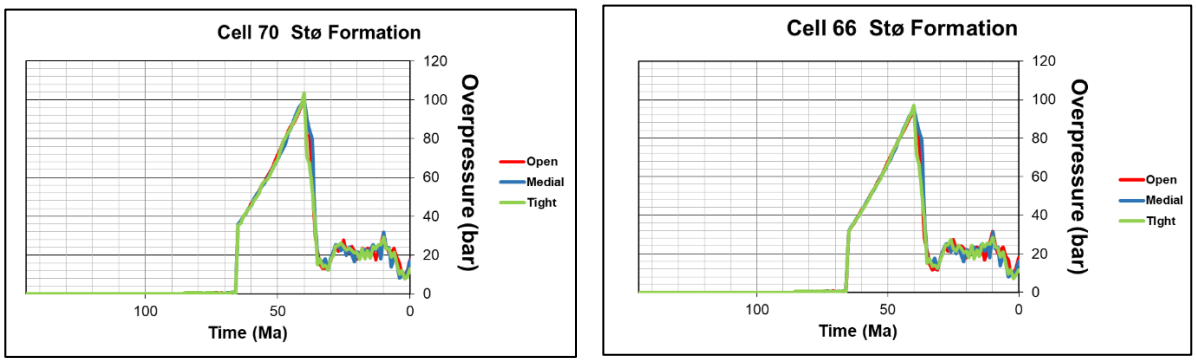


**Figure 5.9:** Modelled overpressure (bar) for compartment 70 (left) and 66 (right).

### 5.3.1 Compare simulated and observed pressures

Finally, Figure 5.10 shows a deviation map, between simulated and observed overpressures in the study area for each of the three permeability scenarios.

The maps show that the deviation among the open and base scenarios are rather similar whereas the tight scenario shows relatively higher deviation from the measured pressure. The base case scenario is used further in the thesis, for the shale permeability.

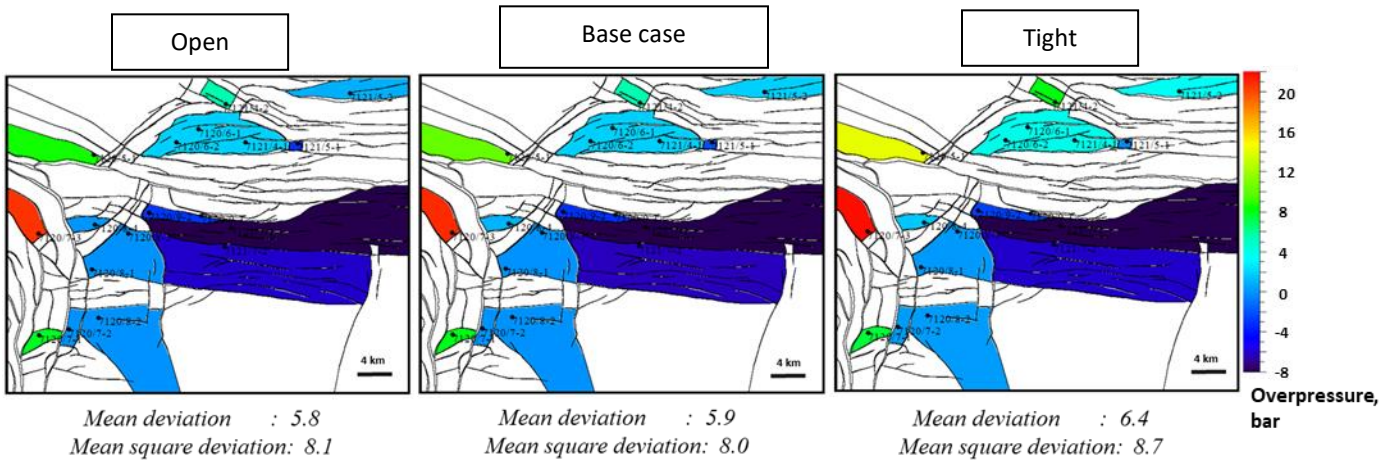


**Figure 5.10:** Deviation maps between the modelled and measured overpressure for the three scenarios of permeability. Colour scale in bars.

Table 5.4 shows the the deviation in pressure between the measured and calculated overpressure, for each of the calibrated compartments. The largest deviations are seen for the compartments 44

and 39. The deviation for each of the compartments goes down as the permeability of shale rock increases.

**Table 5.4:** Deviation in overpressure for each compartment in different scenarios.

| Wells used in the calibration study | Compartment name | Open shale | Base case | Low case |
|---|---|---|---|---|
| | | Deviation, bar | Deviation, bar | Deviation, bar |
| 7120/5-1 | 66 | 13.3 | 10.2 | 8.5 |
| 7120/6-1, 7120/6-2S, 7121/4-1 | 65 | 3.6 | 1.9 | 1.9 |
| 7120/7-1 | 10 | 7.0 | 7.9 | 7.8 |
| 7120/7-2 | 11 | 0.0 | 0.0 | 0.0 |
| 7120/7-3 | 44 | 20.8 | 21 | 20.7 |
| 7120/7-3, 7120/8-3 | 26 | -0.1 | 0.0 | 0.0 |
| 7120/8-2 | 12 | 0.0 | 0.0 | 0.0 |
| 7120/8-4 | 37 | 1.3 | 1.0 | 0.1 |
| 7120/9-1, 7120/9-2 | 41 | -2.8 | -3.1 | -2.9 |
| 7121/5-2 | 79 | 3.3 | 1.9 | 0.9 |
| 7121/7-2 | 35 | -6.1 | -6.3 | -6.0 |
| 7121/7-1 | 39 | -8.7 | -9.2 | -8.9 |
| 7121/4-2 | 78 | 7.5 | 5.7 | 5.7 |
| 7121/5-1 | 67 | -0.5 | -2.1 | -3.0 |
| Mean deviation | | 6.4 | 5.9 | 5.8 |

## 5.4 Amount of erosion – Baig et al, (2016) and Henriksen et al, (2011)

Till now in the thesis, the amount of erosion used in the model set-up was adopted from the study done by Baig et al., (2016), where they presented a net erosion map for the Barents Sea. Another net erosion map is published by Henriksen et al., (2011). While varying the erosion maps, all the other input parameters are kept constant (Table 5.1). The timing of erosion is also kept constant, from 40-35 Ma, and 10 to 2 Ma, and with two times larger magnitude in first erosion event (ratio 2:1) (Figure 4.5 and Figure 4.6).

Figure 5.11 compares pressure distribution map for four times step using the two erosion scenarios. The time steps correspond to 40 Ma, 10 Ma and present day. They have been selected intentionally since important geological events (uplift/erosion and overpressure generation) are related to these time steps. The maps at 40 Ma and 10 Ma are illustrating the overpressure distribution before the first and second erosion episodes (Eocene and Late Miocene-Pliocene) respectively. The maximum overpressure over geological time has been observed at 40 Ma in both scenarios. However, there is a difference between these maps depending on which erosion scenario is being used (Figure 5.11a, c & e and Figure 5.11b, d & f). For all the time steps overpressure is modelled to be higher for the maps that applied the Baig erosion scenario.

The reason of such a distinct difference between the overpressure maps depending on the erosion scenario can be explained with the help of Figure 4.5 and Figure 4.6 which shows the erosion map of Baig with a higher magnitude than of Henriksen. The difference between them is only limited to a few 10's of meters but this was enough to create the distinct difference among the simulation results both on the overpressure and leakage history.

Finally, if the magnitude of erosion is higher in one case, it also experiences steeper burial curve prior to that erosion. Thus, knowing that there is slightly higher amount of erosion for Baig means that the burial rate prior to erosion episodes was slightly steeper for this scenario compared to Henriksen. This process is naturally gets translated into the overpressure maps. For a basin with steeper burial rate (fast sediment deposition) the magnitude of the generated overpressure is higher than that of a basin with less steep burial rate. As mentioned above, there is only very small difference between the two erosion maps, therefore it is not possible to see the visual difference in the steepness of the modelled burial rates for any specified compartment.

One thing to be observed is that the change of erosion scenario has a large impact on the paleo-pressure and leakage. However, the difference in present day overpressure between the two-erosion scenarios is relatively smaller compared to the other two time steps. Figure 5.12 shows the two-different modelled cumulative leakage map each representing the results of the different erosion scenarios.

Figure 5.13 shows the overpressure development through the time for the compartment 4 which is leaking in the Henriksen erosion scenario (see also in Figure 5.11 the location). Figure 5.13 shows

that compartment 4 experienced larger overpressures when the Baig erosion map is used. However, this large overpressure was not enough to set up the failure in this compartment.

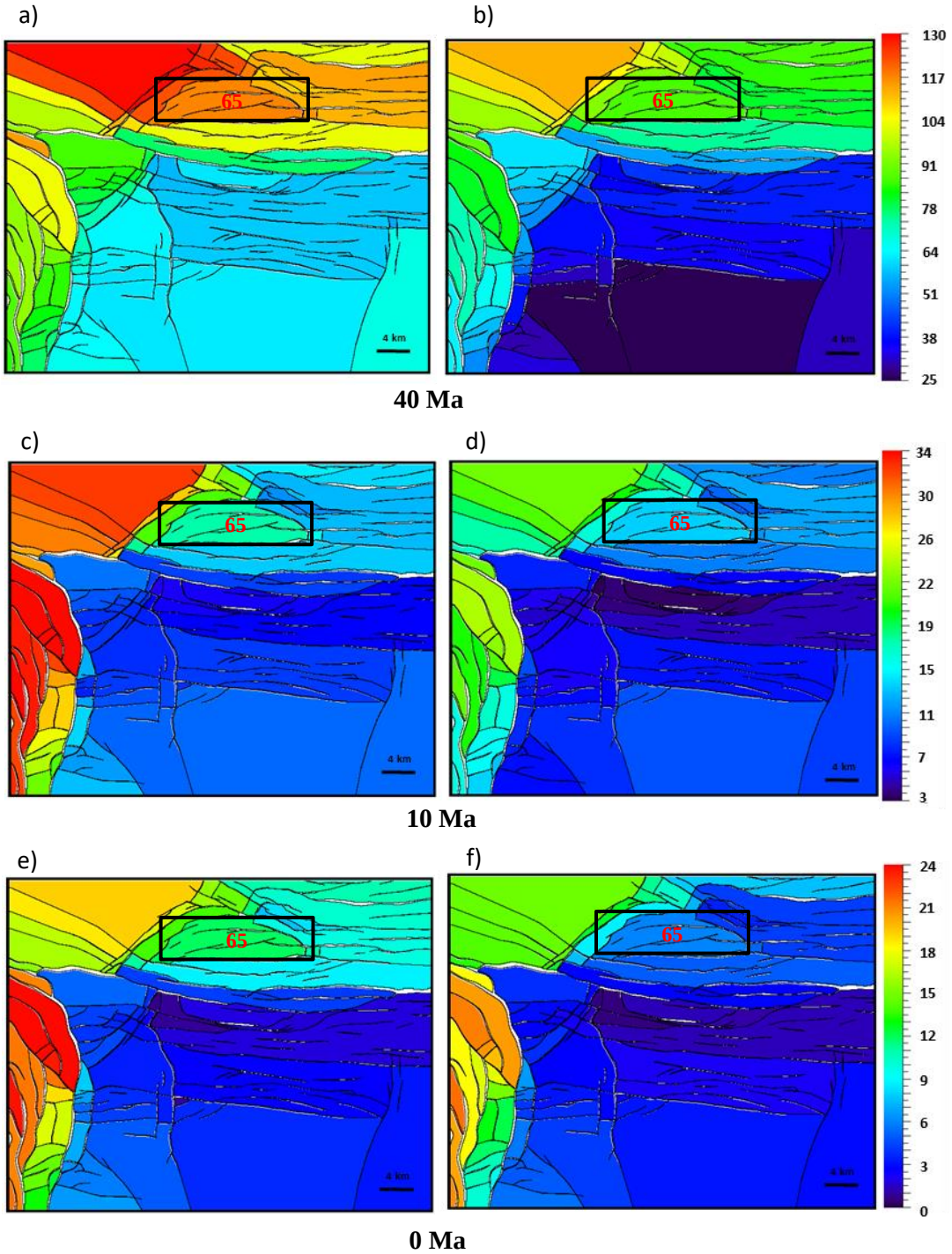


**Figure 5.11:** Overpressure distribution map at time step 40, 10 and 0 Ma by using (a), (c), (e) Baig et al., (2016); (b), (d), (f) Henriksen et al., (2011) erosion maps. The colour scale is unified for each time step. Snøhvit compartment (65) highlighted with the black box.

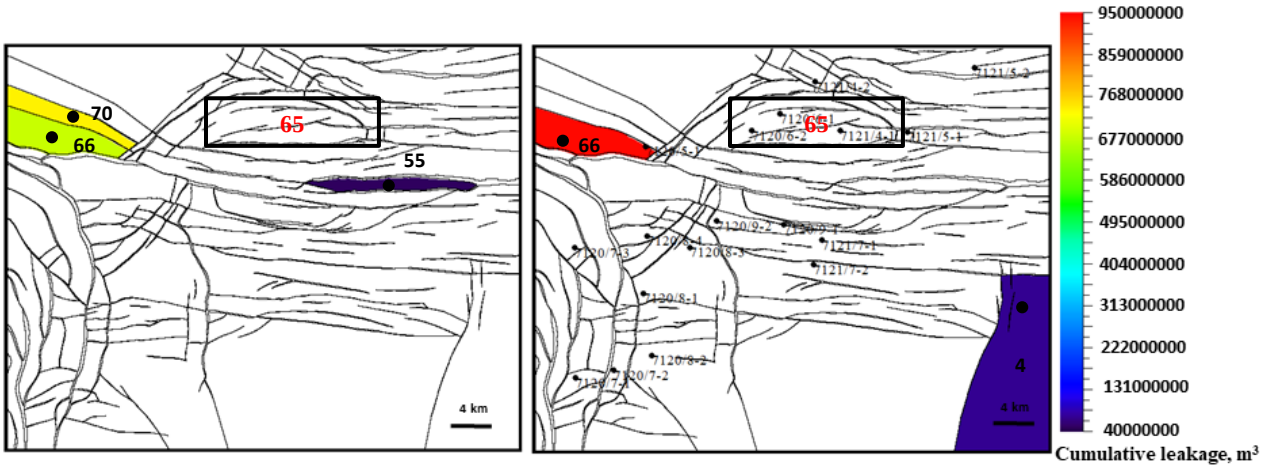


**Figure 5.12:** Cumulative leakage maps when the Baig et al., (2016) (left); Henriksen et al., (2011) (right) erosion maps are used for modelling. Notice the leakage in compartment 4 in southeastern corner using Henriksen's erosion map.

Magnitude of erosion for this compartment 4 can be compared between the two scenarios on Figure 4.5 and Figure 4.6. Red colour indicates the highest magnitude of erosion in the colour scale of maps in Figure 4.5 and in Figure 4.6. One can see that red colour is more dominant and covering all over the compartment 4 and nearby area in Figure 4.6, which is not the case in Figure 4.5. This could explain why the compartment initiates failure once the overpressure reaches its maximum value.

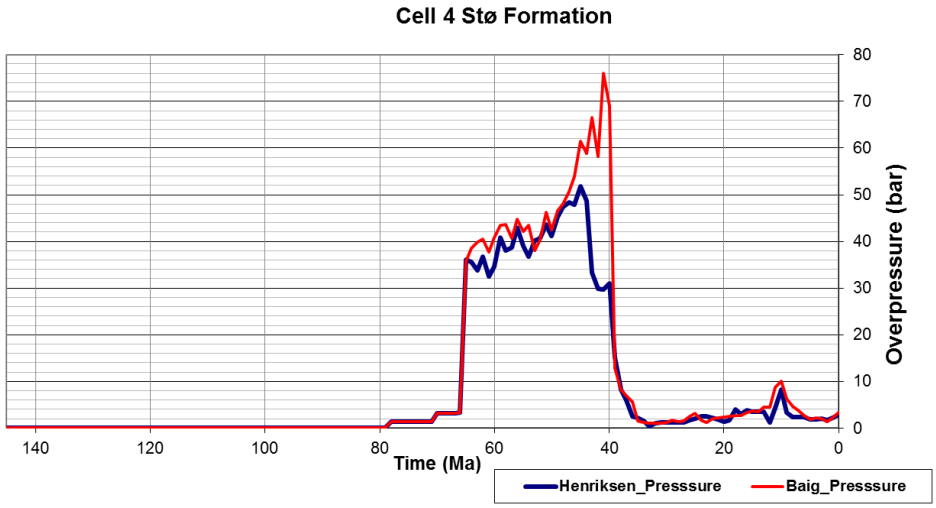


**Figure 5.13:** Overpressure development modelled by using Baig's and Henriksen's erosion maps for the compartment 4.

Comparison of the leakage rate for the leaking compartments of the Baig erosion scenario has already been discussed in Chapter 5.3 and Figure 5.7c as a part of the base case permeability model. Leakage rates for the leaking compartments of the Henriksen et al., (2011) scenario are given in Figure 5.14. Leakage started at a different time for both of the compartments. Compartment 4 shows the leakage of fluid only for very short time before the first erosion episode (Eocene) starts whereas for compartment 66 timing of leakage is much longer due to the higher accumulated overpressure in that part of the study area that can be observed from Figure 5.11b.

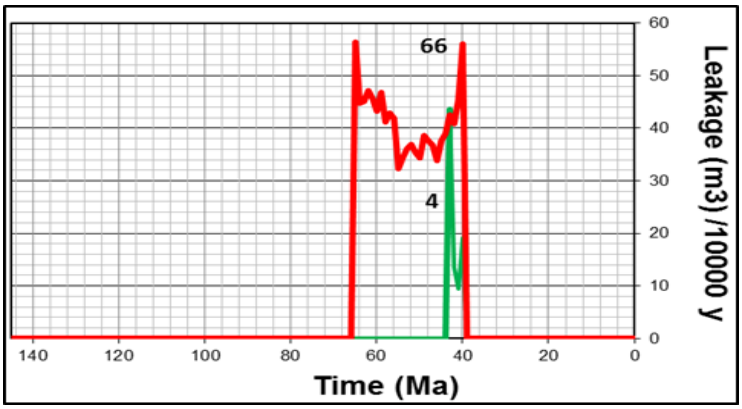


**Figure 5.14:** Leakage rates ($m^3$/10000 years) through geological time for the leaking compartments of the model once the Henriksen et al., (2011) net erosion map is applied in the simulation.

### 5.4.1 Deviation using different erosion maps

Figure 5.15 shows the results of the pressure calibration. The deviation values are smaller for Henriksen erosion map compared to the results acquired when the Baig erosion map has been used.

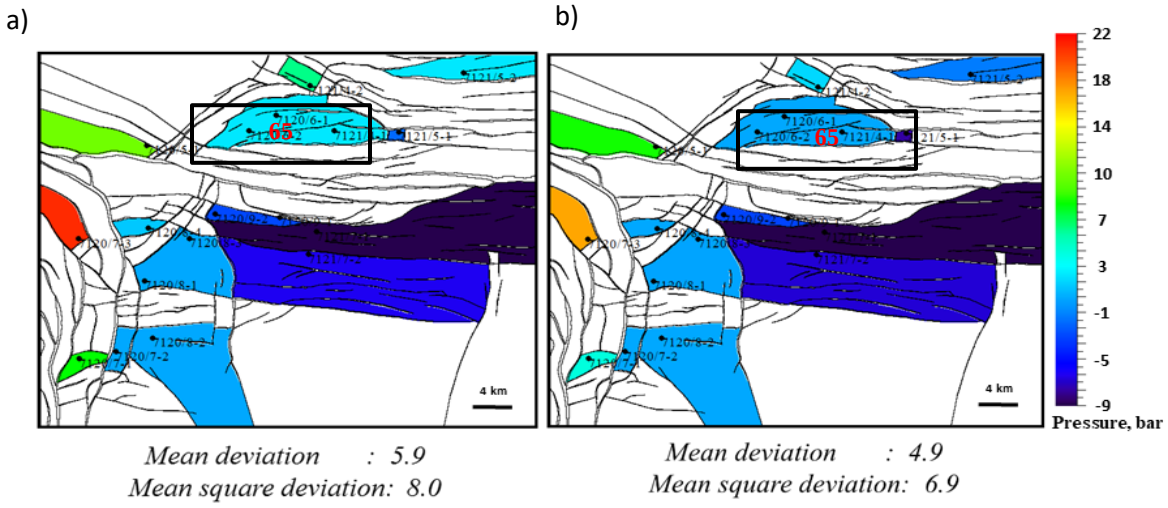


**Figure 5.15:** Overpressure deviation maps between the modelled and measured pressure for (a) Baig et al., (2016); (b) Henriksen et al., (2011).

Table 5.5 shows the deviation in pressure for each compartment after the erosion scenario is changed. Deviation in pressure differs at least +/- 2 bar for each compartment when the simulation is done by using the Henriksen's erosion map instead of Baig's erosion map.

**Table 5.5:** Deviation in overpressure for each compartment in different scenarios.

| Wells used in the calibration study | Compartment name | Baig et al., (2016) | Henriksen et al., (2011) |
|---|---|---|---|
| | | Deviation, bar | Deviation, bar |
| 7120/5-1 | 66 | 10.2 | 8.1 |
| 7120/6-1, 7120/6-2S, 7121/4-1 | 65 | 1.9 | 0.0 |
| 7120/7-1 | 10 | 7.9 | 3.8 |
| 7120/7-2 | 11 | 0.0 | 0.0 |
| 7120/7-3 | 44 | 21 | 17.2 |
| 7120/7-3, 7120/8-3 | 26 | 0.0 | -0.2 |
| 7120/8-2 | 12 | 0.0 | 0.0 |
| 7120/8-4 | 37 | 1.0 | 0.0 |
| 7120/9-1, 7120/9-2 | 41 | -3.1 | -3.3 |
| 7121/5-2 | 79 | 1.9 | -1.5 |
| 7121/7-2 | 35 | -6.3 | -6.8 |
| 7121/7-1 | 39 | -9.2 | -9.7 |
| 7121/4-2 | 78 | 5.7 | 1.4 |
| 7121/5-1 | 67 | -2.1 | -7.7 |
| Mean deviation | | 5.9 | 4.9 |

## 5.5 Variation in burial history

Different erosion magnitudes for two erosion episodes (Eocene and Late Miocene-Pliocene) is tested below by varying their ratio in their magnitude. All the magnitude changes will be implemented in the Baig et al., (2016) net erosion map. The timing of these erosion episodes is assumed to be constant, 40-35 Ma for Eocene, 10-2 Ma for the Late Miocene-Pliocene.

As mentioned in Chapter 4.6, there are several opinions on this but yet there is some disagreement to the answer of the posed question of which erosion event had the highest magnitude of sediment

removal. Therefore, in this chapter, several magnitude ratios will be varied to display the importance of it in the leakage and overpressure history of the basin. Table 5.6 shows the scenarios that will be tested and their magnitudes.

**Table 5.6**: Overview of the tested burial history scenarios.

| Burial history | | | |
|---|---|---|---|
| Eocene: Late Miocene - Pliocene | | | |
| Base case | Scenario D | Scenario E | Scenario F |
| 2:1 | 1:2 | 4:1 | 1:4 |

### 5.5.1 Scenario D (erosion ratio 1:2)

The initial test will be performed by changing the default magnitudes ratio (2:1) of two erosion (Eocene**:** Late Miocene-Pliocene), episodes that has been used in the simualtions up to this step, to the ratio of 1:2. Figure 5.16 shows how the overpressure changes during the three critical geological time steps both for the study area (three maps on top) and for the compartment 65 (graph). There is no leakage observed in any compartment for this scenario since ovepressure is unable to attain the higher enough values to initiate the hydraulic fracture. The change of the erosion magnitude over geological time is illustrated with the pressure trend (in blue color) of compartment 65 in the graph in Figure 5.16. The graph shows the first overpressure period, that took place before the onset of first erosion event did not reach high values. The second overpressure generation episode, that starts approximately at 25 Ma reached the maximum value of nearly 80 bar before it started to decrease with the inititation of second and largest erosion episode for this scenario.

The comparison of these two ovepressure picks tells that the magnitude of the maximum overpressure picks attained before the onset of each erosion episodes has approximately a ratio of 1:2, which is proportional to the erosion scenario magnitudes implemented for this case. Burial depth trend (in orange color) in the graph, is also helpful to distiguish two erosion magnitudes and follow the rate of burial over the geological time. The fastest burial rate observed for this compartment corresponds to the timing after the end of first erosion epiode til the onset of second erosion episode. The maps in Figure 5.16 also illustrates a similar conclusion in the basin scale, that the maximum overpressure is observed at 10 Ma which corresponds to the time between the two erosion episodes.

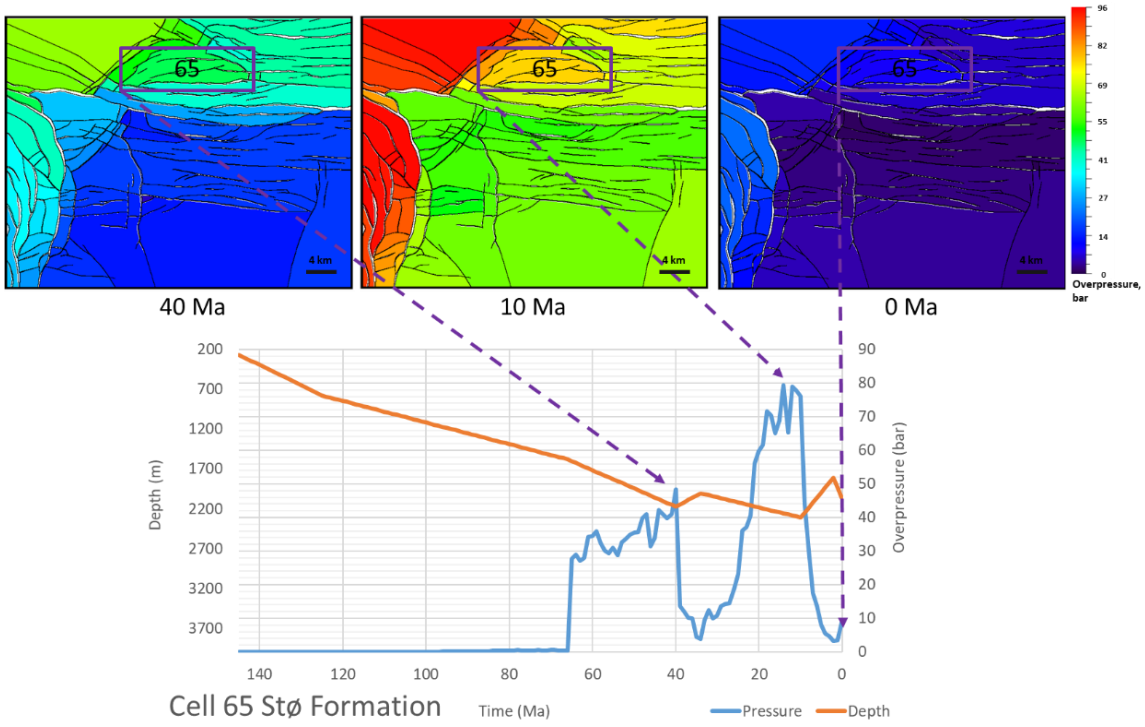


**Figure 5.16:** The graph below describes the change of overpressure and burial history over 145 – 0 Ma for the Snøhvit compartment (65). The three modelled overpressure maps belong to the 40, 10 and 0 Ma in the geological history while applying the burial scenario D (1:2).

### 5.5.2 Scenario E (erosion ratio 4:1)

This scenario describes the case where the magnitudes of erosion episodes have the ratio of 4:1 by taking the first erosion episode as the major one and second episode as the minor one. The graph in Figure 5.17 shows the modelled overpressure change over a geological time for compartment 65 as a response to the implemented erosion scenario. Only one major pressure pick visible, reached to nearly 120 bar (Figure 5.17). Since the first erosion episode is simulated to erode 460 m of the sediment column, almost all generated overpressure is released at this time. However, following the first erosion episode, there were no significant pressure build up due to the severe uplift that happened previously. The same trend can be observed from the areal overpressure maps in the Figure 5.17, that among three time steps maximum overpressure is modelled approximately at 40 Ma and the other two time steps shows the overpressure at maximum 30 bar but no more than that. Hence, the analysis done for the compartment 65 is similar to the pressure analysis in the study area.

Burial rate in the graph in Figure 5.17 shows that Stø Formation is deeply buried till nearly 2400 m depth which is a relatively deep depth compared to the other cases

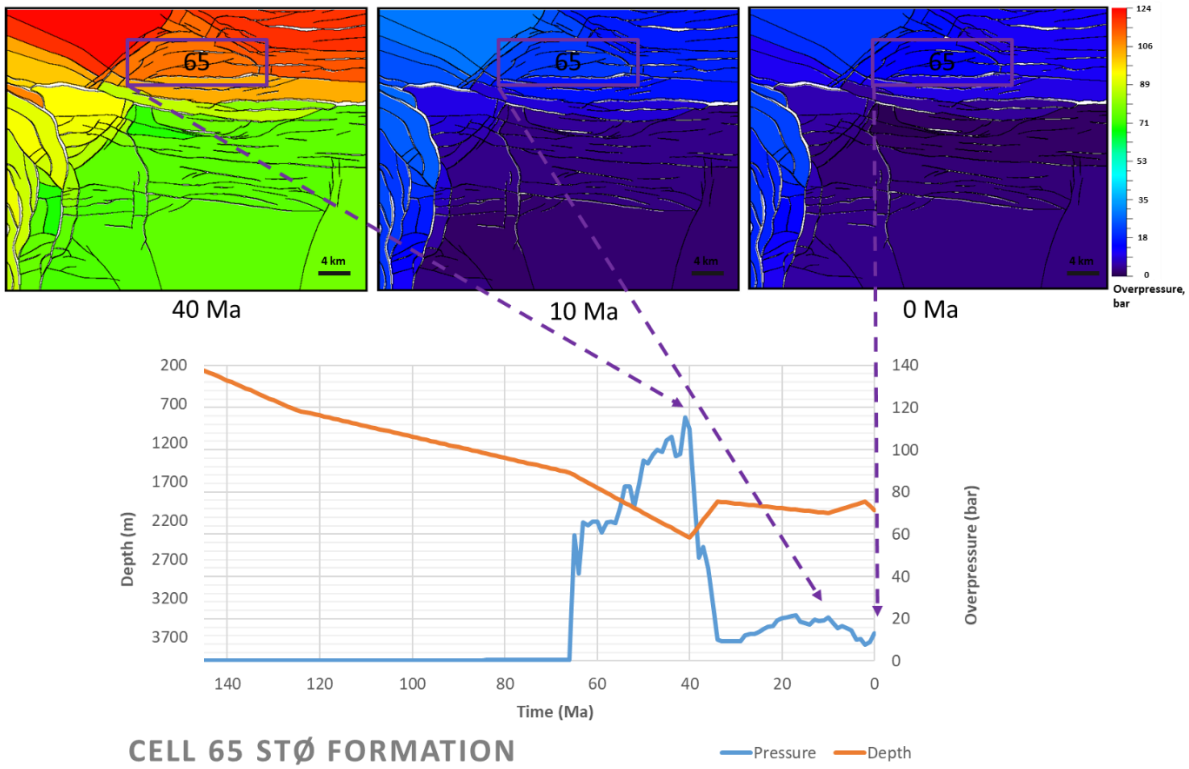


**Figure 5.17:** The graph describes the change of overpressure and burial history over 145 – 0 Ma for the Snøhvit compartment (65). The three modelled overpressure maps correspond to 40, 10 and 0 Ma in the geological history while applying the burial scenario E (4:1).

In this scenario, hydraulic leakage is modelled since the overpressure attains very high values during burial at the reservoir section which lead to the cap-rock failure. In total, five compartments failed and most of them located on the western, deeply buried part of the study area (Figure 5.18a). The comparison of the leakage rate in each of the compartments is given in the Figure 5.18b. The least amount of leakage is modelled for the compartment 54 which is located on the western side and leakage started relatively late in the geological history. This can be due the influence of the two major leaking compartments - 70 and 66, located on the western side of the study area. They started leaking at 66 Ma. This leads to the loss of the accumulated overpressure in the nearby compartments as well as, such as in compartment 54. Therefore, compartment 54 started to leak relatively late, at 48 Ma.

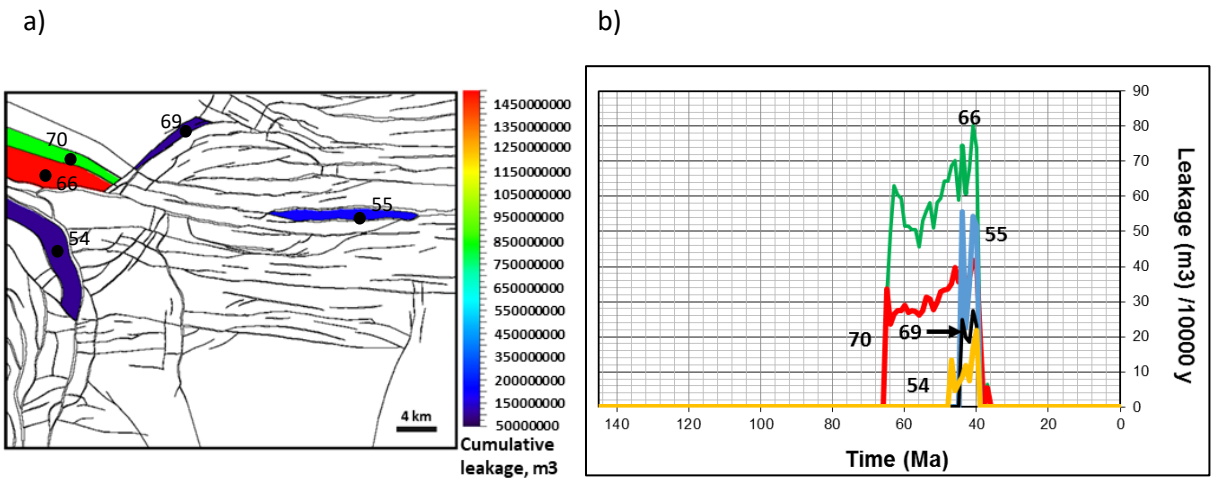


**Figure 5.18:** (a) Modelled cumulative leakage ($m^3$) map and (b) leakage rate ($m^3$/10000y) for all the leaking compartments (right).

### 5.5.3 Scenario F (erosion ratio 1:4)

This is the inverse of the previous scenario where erosion magnitudes will be switched from 4:1 to 1:4. The results of the simulation is given in Figure 5.19 and Figure 5.20. Accordingly, in Figure 5.19, the overpressure trend is demonstrated for compartment 65 to show how the pressure picks changed their location on time.

Compared to the erosion scenario E, the maximum pressure build up attained in compartment 65 is just below 100 bar at 10 Ma following the first erosion episode (Figure 5.19). However, there is not enough pressure generated prior to the onset of the first erosion episode. In addition, there is a considerable difference in the magnitude of first overpressure build up between the previous scenario and current one. In scenario E, the small pressure peak modelled at 18 Ma (Figure 5.17) was barely reaching to 20 bar whereas for this scenario overpressure goes up to 40 bar since in this scenario there was much more time for the pressure to build up to occur, starting from 145 Ma till 66 Ma, without having any interfering erosion episode. Modelled burial rate (orange colour) in the graph of Figure 5.19 illustrates that the reservoir rock Stø Formation is buried deepest prior to the initiation of the second erosion which has the highest magnitude for this study.

For this scenario, there are only four compartments that are leaking (Figure 5.20a). The highest leakage rate is modelled in the compartment 4 which is located on the south-eastern part of the study area and this is the compartment that stared leakage earliest in the geological history (Figure 5.20b).

The timing of failure in all three compartments is concentrated between the first and second erosion episodes and they correspond to the time when the second and largest overpressure generation took place.

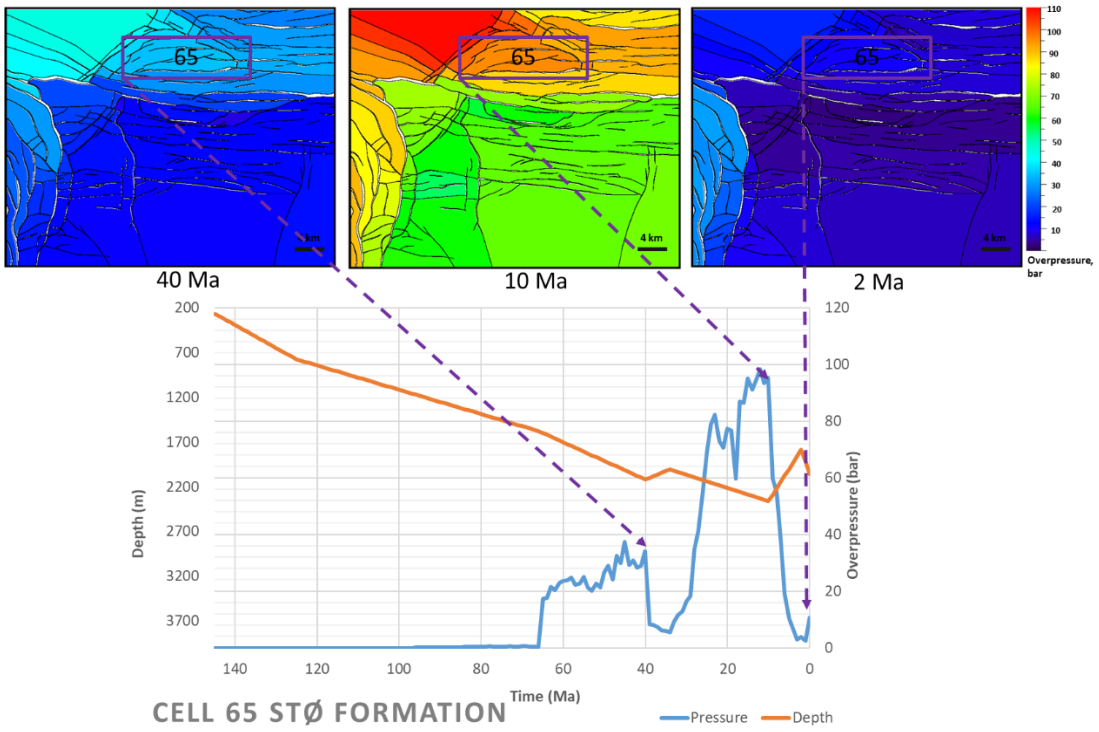


Figure 5.19: The graph describes the change of overpressure and burial history over 145 – 0 Ma for the Snøhvit compartment (65). The three modelled overpressure maps correspond to 40, 10 and 0 Ma in the geological history while applying the burial scenario F (1:4).

a) b)

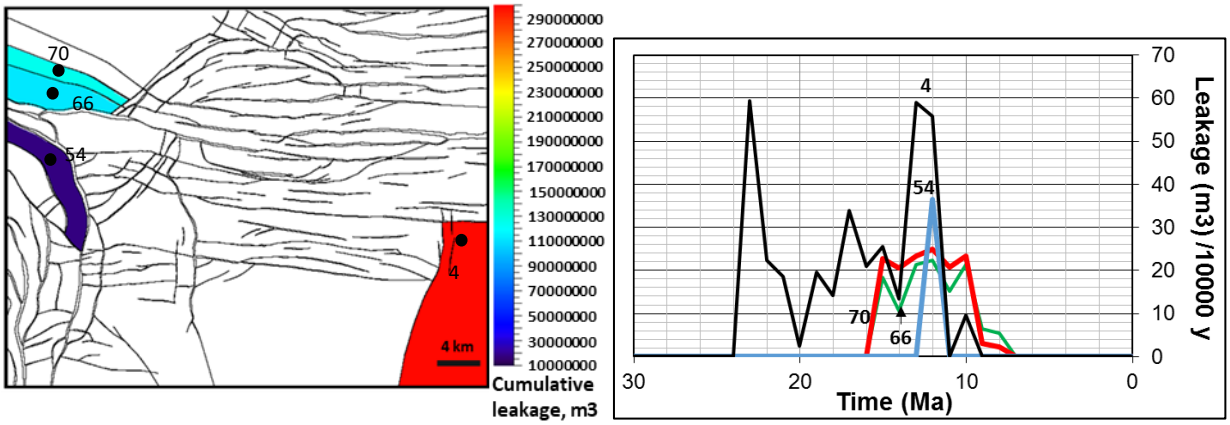


**Figure 5.20:** (a) modelled cumulative leakage ($m^3$) map and (b) leakage rate ($m^3$/10000y) for all the leaking compartments.

# 6. Uncertainty modelling using a Monte-Carlo approach

A total of 1000 runs were used in one Monte Carlo simulation. There are two parameters varied in terms of simulation. Magnitude of minimum horizontal stress– Grauls number and permeability exponent. These were defined as with mean and standard deviation and Table 6.1 shows the mean and standard deviation that is used for of the input parameters in the simulation. In each Monte-Carlo simulation run, values of the selected parameters were drawn randomly from their assigned probabilistic distribution.

**Table 6.1:** Parameters and their values used in the Monte-Carlo simulation

| Process modelled | Mean | Std. Deviation |
|---|---|---|
| Minimum horizontal stress (Grauls number) | 1.144 | 0.05 |
| Permeability exponent | 9 | 2 |

Two different Matlab codes have been employed to display the figures in this chapter. For the studies of the first two chapters', calibration between the measured and simulated overpressure is taken as the basis for the Monte-Carlo simulation analysis. The aim was to find the best-case scenario that gives the least deviation with the measured overpressure among 1000 simulations.

There are some compartments where more than one well used for the pressure calibration and in these compartment the wells do not measure the same overpressure with each other. Hence, the average value of overpressure is used to account for the uncertainty in these compartments. This average overpressure could be the source of inherent uncertainty in estimating the amounts of overpressure for some of the compartments. In the calibration file, different weights can be applied to the wells. An important aspect of this procedure is this weighting of the simulation results according to how well they match the measured pressures in the study area. The choice of weighting procedure and the correct weights is crucial to the reliability of the results. If weight is set to 1 for all wells, no calibration field weighting is performed and the misfit (deviation in pressure) is considered to represent a "global misfit". Hence, the results are presented in two different subchapters one with weighted calibration and one with unweighted calibration. The third chapter illustrates the modelling results for the most probable pressures along a vertical well path.

## 6.1 Unweighted Monte-Carlo simulation

There are two parameters that are implemented into Monte-Carlo simulation. Figure 6.1 shows the error plot for the Grauls value. Blue circles in the figure mark the average pressure deviation between the measured and modelled overpressure as normalized to 0 and 100 for each simulation where the Grauls number changes along the horizontal axis of the plot. Figure 6.4 illustrates the similar plot for the permeability exponent which is the second parameter to be varied in Monte-Carlo simulation. The total number or runs in these figures equal to 1000.

### 6.1.1 Grauls number

In the Figure 6.1, error is increasing as the Grauls number decreases. Error skyrocketed towards 100, for the Grauls numbers smaller than approximately 1.07, which gives confidence range. Blue circles make a saddle trend where the error is lowest for very low values of Grauls number but then the error became relatively constant no matter which value of Grauls number is used. This, is the case when probabilities resulting from Monte Carlo simulation approach became stable. 'Stable' is taken to mean that the distribution shows minor changes when doubling the number of simulated parameter. The red circle in this figure is positioned in the saddle zone to show the case when the least error is acquired.

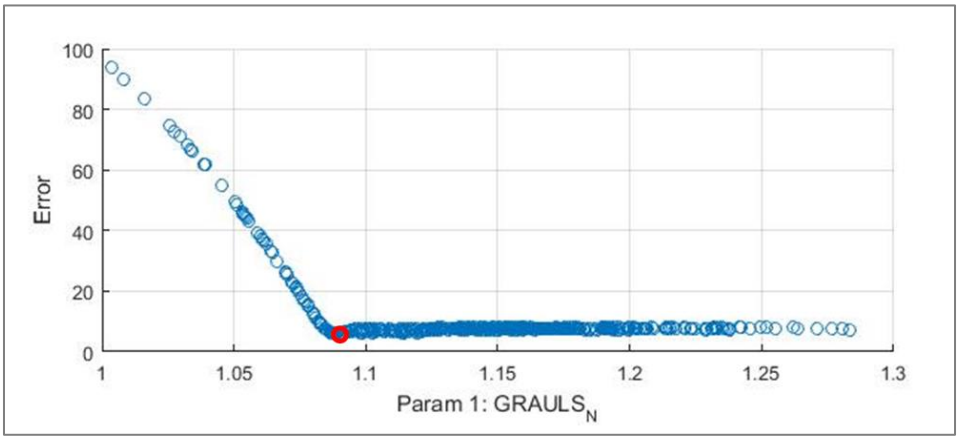


**Figure 6.1:** Grauls number from 1000 simulations versus pressure deviation in each simulation. Deviation in pressure is normalized to 0 to 100 scale of error. Red circle highlights the run where the least error is achieved.

The location of the red circle corresponds to the Grauls number of 1.09. This value is significantly lower than the observed LOT data from the area (Figure 4.4). Hence, new error distribution plot is made by excluding the simulations with value of Grauls number less than 1.14 among the 1000

simulations. There are 552 simulations left after this. The new error distribution of the Grauls number is given in Figure 6.2. Grauls number for the best match run (solid red circle) is 1.185. This number is quite different than the one used in Chapter 5 for the sensitivity analysis. The red dotted polygon shows the part of the plot where data is clustered which corresponds the confident range of Grauls number to be used in the future studies.

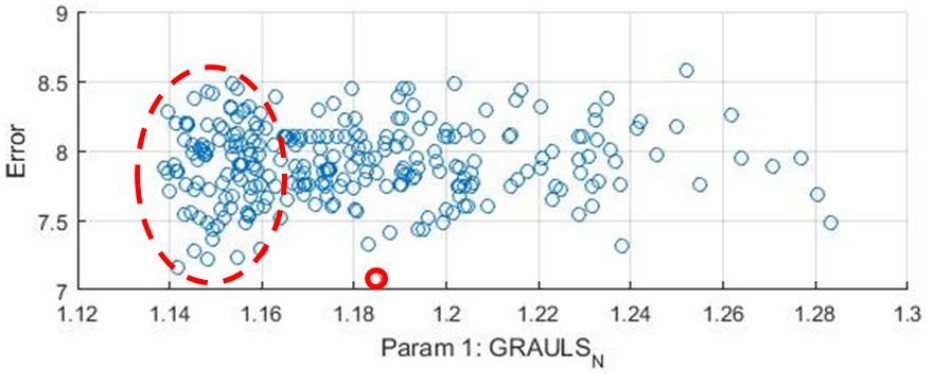


**Figure 6.2:** Simulated scenarios of Grauls number when Grauls number less 1.140 cases are excluded from the plot. Deviation in pressure is normalized to 0 to 100 scale of error. Red circle highlights the run where the least error is achieved. Grauls number at the least error point corresponds to 1.185.

### 6.1.2 Shale exponent

Figure 6.4 shows 1000 simulation runs and their evenly distribution of permeability exponent between 4 and 15. The red circle corresponds to the permeability exponent value of 8.9 which is almost the same value used in the sensitivity analysis in Chapter 5. However, no confidence range can be acquired based on this plot. Majority of the circles are aligned on a line and they seem to show the same error value.

Figure 6.5 illustrates the error distribution of permeability exponent for 552 simulation runs (after the Grauls number cut-off made). There are a lot of supercharge points for the distribution of the parameter permeability exponent (Figure 6.5). Permeability exponent of 7.2 is picked as the one giving the lowest deviation. Similar to the Grauls number, this selected value of permeability exponent is also different from the one employed as a base case of single run simulations in Chapter 5 (Table 6.2). Slightly clustered data zone is also observed in Figure 6.4 and highlighted with red dotted polygon.

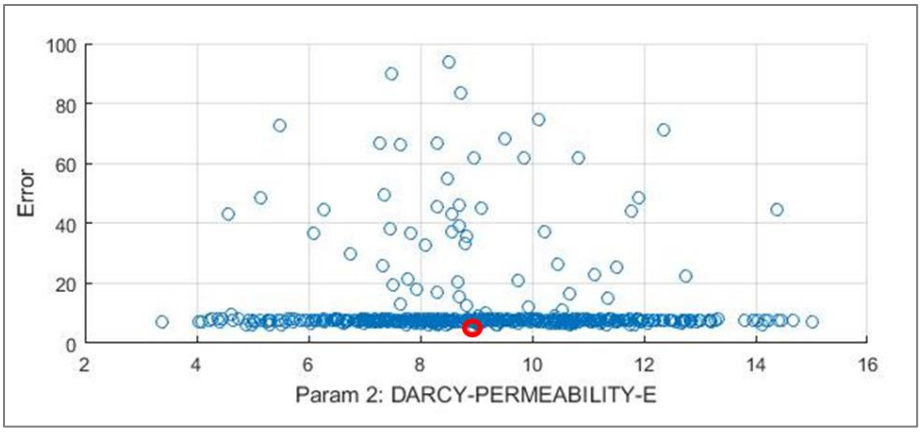


**Figure 6.3**: Permeability exponent from 1000 simulations versus pressure deviation in each simulation. Deviation in pressure is normalized to 0 to 100 scale of error. Red circle highlights the run where the least error is achieved.

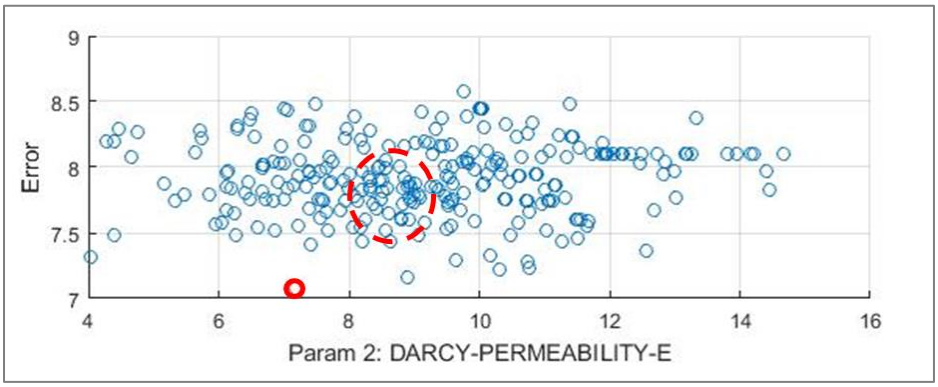


**Figure 6.4:** Simulated scenarios of permeability exponent when Grauls number less 1.140 cases are excluded from the plot. Deviation in pressure is normalized to 0 to 100 scale of error. Red circle highlights the run where the least error is achieved. Permeability exponent at the least error point corresponds to approximately 7.2.

### 6.1.3 Misfit for each well

Figure 6.5 describes the global misfit plots for the calibration wells. There are 552 simulation runs plotted in the upper graph of this figure. The lower graph is the magnified version of the scenarios from 200 to 250. These global misfit plots show how accurate a simulation run matches the calibration wells, i.e. the average error in the modelled pressure in the compartments. Horizontal axis shows the number of the simulations and the vertical misfit axis is the measure of the average pressure deviation in each compartment for each scenario. If there are a several wells in the one compartment, the average measured pressure is used for the calibration from that compartment. Not all of the compartments showed a good fit with the modelled pressure data. Based on the

colour code, it is quite straightforward to define which well has good or bad fit with the modelled overpressure. The largest misfit is observed for well 7120/7-3 and well 7120/5-1. Both of these wells are drilled into the compartments situated at the rim of the study are (compartment 44 and 66 respectively) (Figure 5.6a). In addition, they are not included in the study area with their whole size. Thus, these compartments may have some uncertainty due to their part outside of the study area.

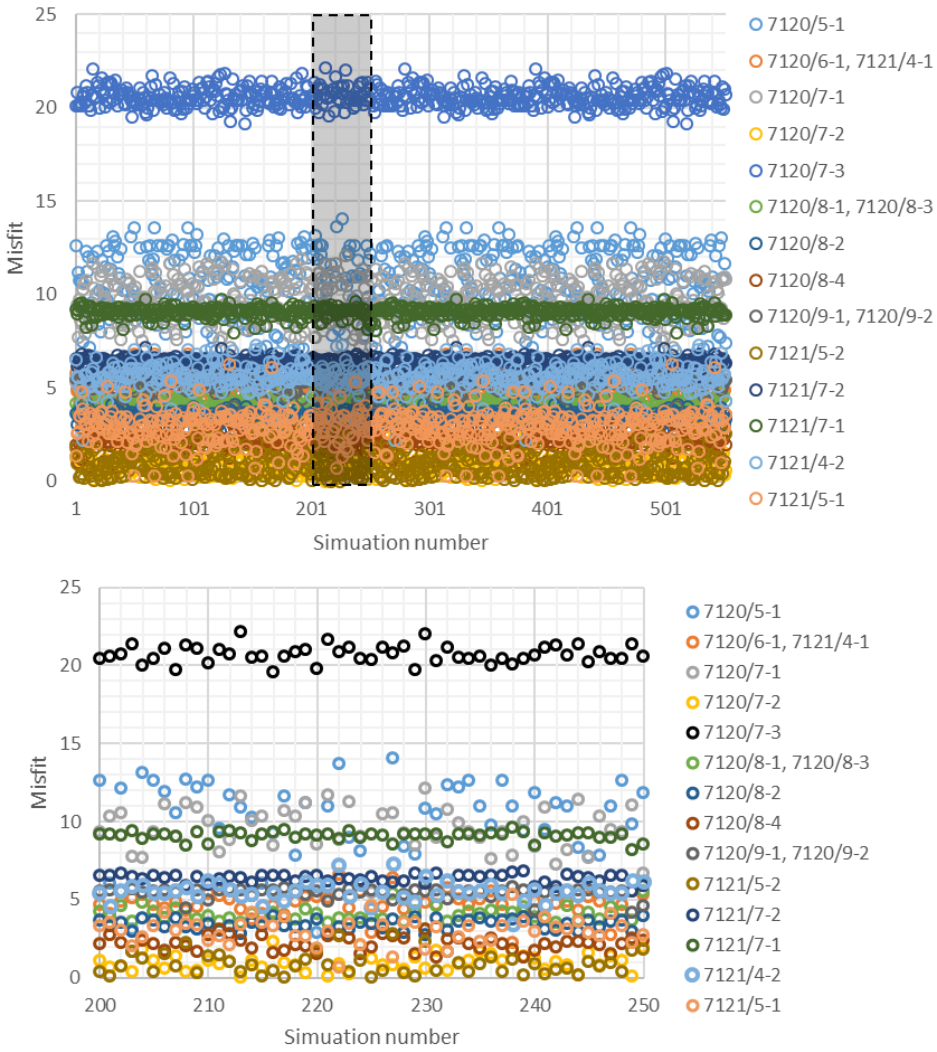


**Figure 6.5:** Misfit plot for the scenarios with the Grauls number cut off 1.140. Number of the scenarios after the cut made is 552. Misfit is normalized to 0 to 100 scale of error. Plot on top shows the misfit for all the simulated scenarios whereas plot on the bottom shows the misfit only for 200-250 scenario range. Misfit of each well for all the scenarios is color coded and is shown to right of the figure on both plots. The largest misfit belongs to the well 7120/7-3 drilled in a boundary compartment on the western part of the study area.

Well 7121/7-1 is also among few wells where misfit has large value. The compartment calibrated by this well (39) has relatively larger size compared to the others (Figure 5.6a). Therefore, source of large misfit can be connected to the existence of the undetected faults and barriers, which makes it difficult to calibrated the whole compartments with just one well drilled in the centre of it. The rest of the compartments showed relatively lower misfit values, especially Snøhvit compartments wells 7120/6-1 and 7121/4-1. In the magnified plot, small yellow circles highlight close to zero misfit for the well 7120/7-2. This compartments that the well drilled in, is located between the two reliably calibrated pressure compartments on the south-western part of the study area.

## 6.2 Weighted Monte-Carlo simulation

This study is performed for the scenarios which has the Grauls number of larger than 1.14 due to the reasons discussed in the previous chapter. Calibration of the Snøhvit compartment (65) is done with three measured pressure from three different wells. Thus, this compartment has given maximum weight of 100% due to the reliable pressure measurements done. As mentioned above compartments with the average measured pressures are given relatively lower weights compared to the other wells. Table 6.2 helps to compare the best matched scenarios for Grauls number and permeability exponent. There is a large difference for both parameters between single run sensitivity analysis (chapter 5) and unweighted Monte-Carlo simulation results. The difference gets smaller between the values of these parameters after weighted calibration was performed. However, the table shows that Grauls number and permeability acquired after the weighted analysis do not particularly match the sensitivity analysis of chapter 5, however it is much closer than the unweighted analysis results. It is possible to get a better match between the weighted and single run simulations by increasing the number of simulation for the future studies.

**Table 6.2:** The simulation and tested parameters that are selected as the best match in three different studies. MoCa: Monte-Carlo

| The study | No of the simulation | Grauls number | Permeability exponent |
|---|---|---|---|
| Single run (Chapter 5) | | 1.144 | 9 |
| Unweighted MoCa | 225 | 1.185 | 7.2 |
| Weighted MoCa | 75 | 1.148 | 10.3 |

## 6.3 Pressure modelling along the well path

Monte-Carlo simulation can also be used to model the change of overpressure at the present day along a planned vertical well path. Figure 6.6 shows the probability distribution of overpressure for the reservoir rock of the Stø Formation. The pressure plotted, is taken from the top of the pressure compartment 65 at the Snøhvit field. The modelled main overpressure is 11.5 bar. The distribution of the overpressure in this figure is a skewed distribution and the most probable overpressure is well matching with the mean of the distribution.

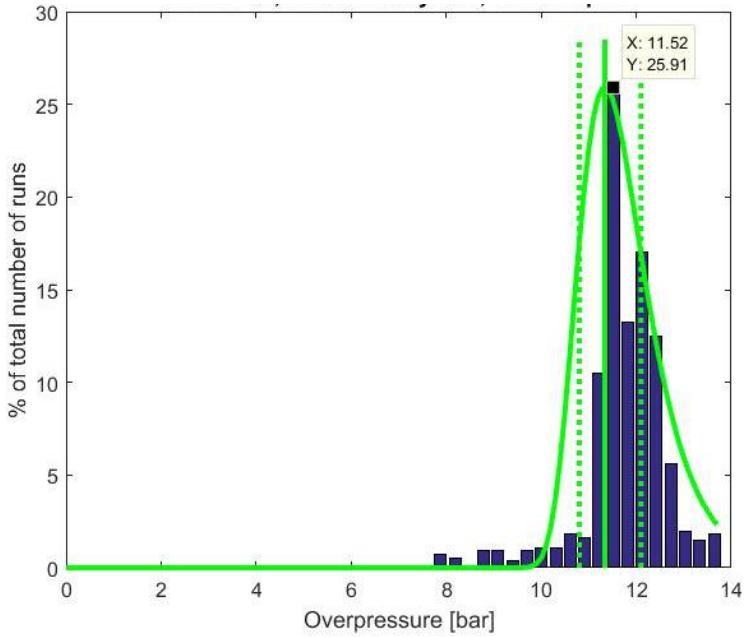


**Figure 6.6:** Probability distribution of overpressure for Snøhvit compartment (65) with std. dev of +/- 1 bar.

Each of the 552 simulation results, that Grauls number cut-off applied, were used to build the most probable pressure prognosis for every compartment just like simulating pore pressure for the projected well at present. Figure 6.7 illustrates the hydrostatic and lithostatic pressure together with the most probable pore pressure and its standard deviation for the Snøhvit compartment. The figure shows that there is no considerable overpressure modelled for this compartment.

Figure 6.8 shows the plot of the predicted overpressure versus depth. The small note on the figure informs that the overpressure at top reservoir depth is equal to 11.4 bar.

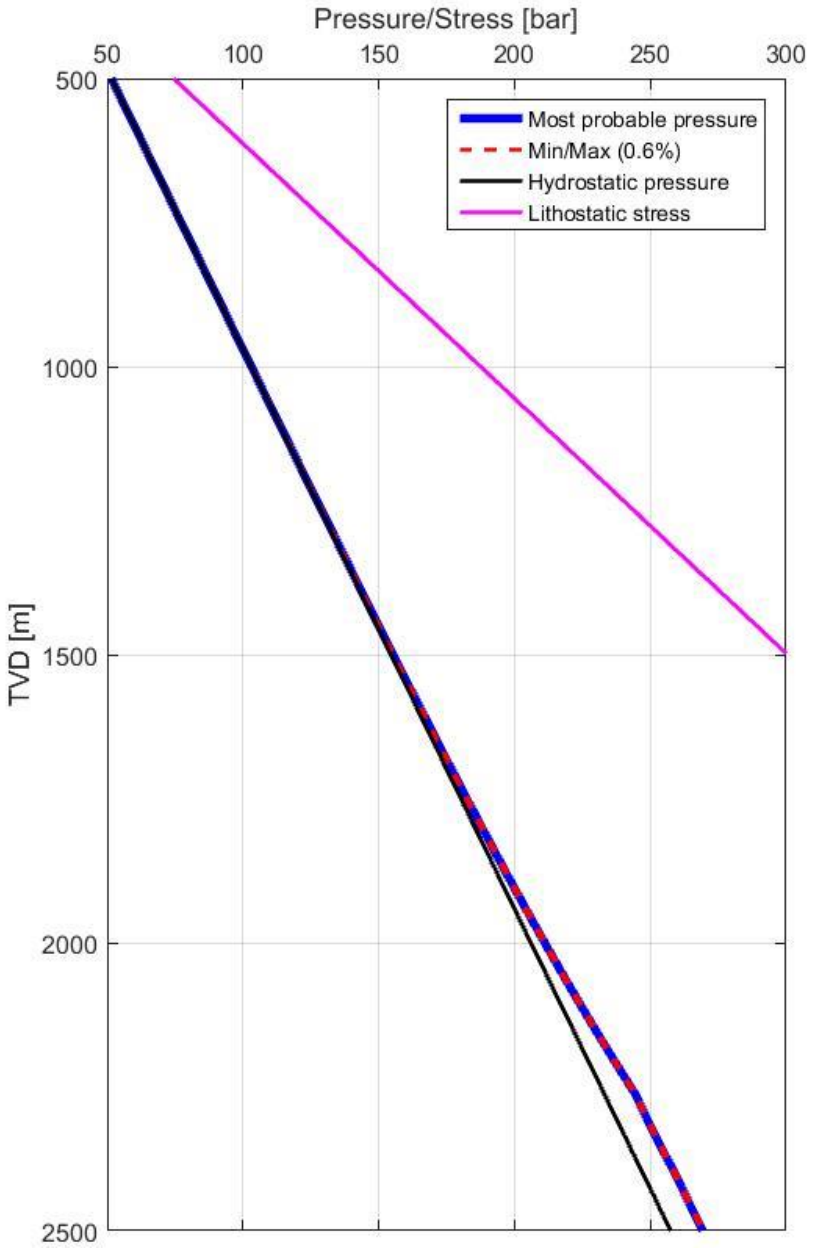


**Figure 6.7:** Schematic illustration of pore pressures predicted pre-drill. Uncertainty ranges are given from Monte-Carlo analysis.

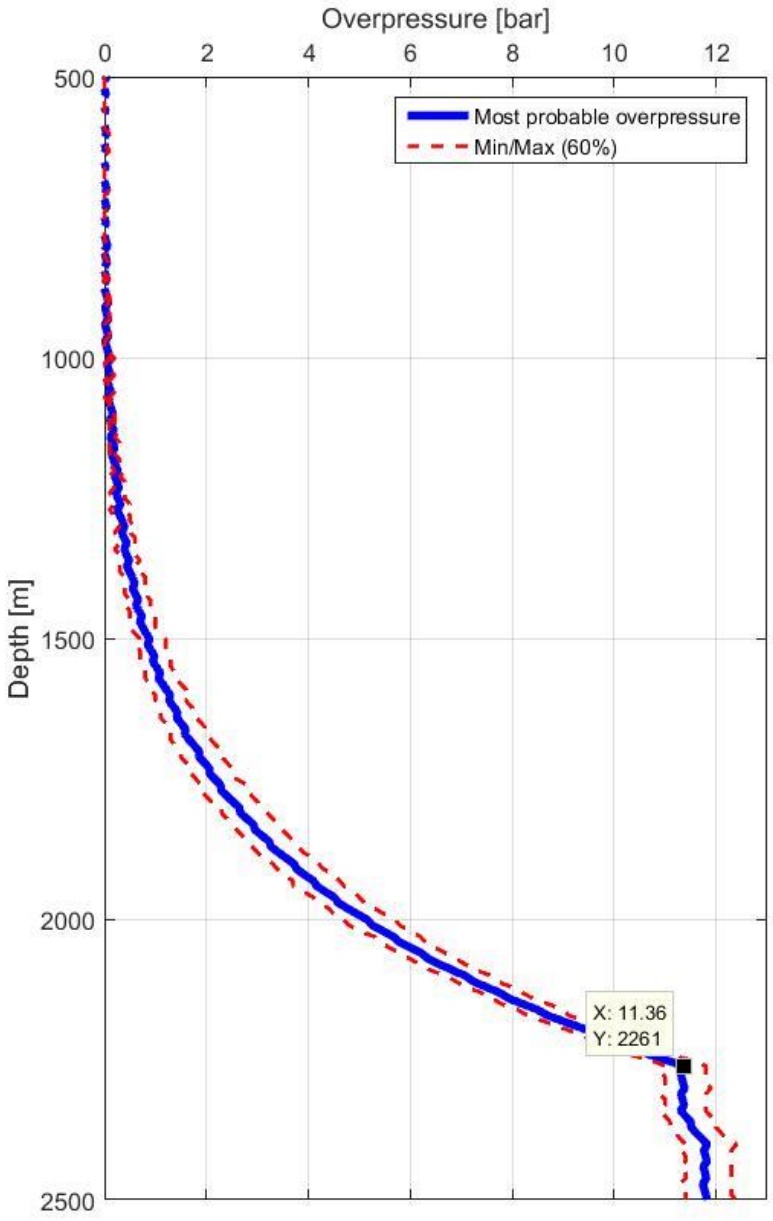


**Figure 6.8:** Mean and standard deviation in overpressure vs depth (mTVDSS) for Snøhvit pressure compartment (65) with std. dev of +/- 0.5 bar.

# 7. Discussion of the results

In this study, the main focus was on the set of parameters affect the pressure distribution and leakage in the Hammerfest Basin, thus these parameters and their values are discussed first before moving on the discussion of the pressure and leakage maps.

In this chapter, input data and model set up like minimum horizontal stress, shale permeability, net erosion and timing of erosion is analysed and compared to existing literature. In addition, the leakage map has been compared to the observed leakage maps done in the literature.

## 7.1 Magnitude of minimum horizontal stress

The measured LOT data from wells has natural scatter in a basin (Figure 4.4). The issue of scattering LOT points has also been mentioned by Økland et al., (2002) as a way of giving considerable room for subjective interpretation of the local minimum horizontal stress trend. Addis et al., (1998) noted that the lower LOT values in an area probably reflect the presence of the favourably oriented pre-existing fractures in the test interval. Therefore, they use a lower bound envelope to a number of LOTs as a reliable method. This reasoning is applied here and simulated minimum horizontal stresses are creating the lower bound for the LOTs in the plots given in Figure 5.4a, c & e.

The measured LOT for the study area matches with Grauls number in the range of 1.13-1.155 (Figure 4.4). Therefore, the further analysis was done by using three values in this interval which are the closest to the best match and also gave the good fit between the modelled and calculated overpressure in the study area.

Structures of the Hammerfest Basin at the top Stø level has been dominated by extension (normal fault) regime although it has been suggested that the deformational style indicates reactivation by strike-slip in the Late Jurassic to Early Cretaceous (Berglund et al., 1986; Gabrielsen and Færseth, 1989; Gabrielsen et al., 1990; Sund et al., 1986). However selected value fo Grauls number (1.144) for the base case corresponds to the range of extensional basins in the Figure 3.10

## 7.2 Shale permeability

The two parameters (surface permeability - $k_0$ and permeability exponent (c) that are tested, to determine the shale permeability at depth, are poorly known and given the highly variable lithological nature of mudstones, these parameters are likely to be variable (Yang and Aplin, 2010).

Shale actually has a lot of porosity, but extremely low permeability due to the small grain size, which reduces the paths that the hydrocarbon can flow.

There is extreme difficulties in measuring permeabilities lower than $10^{-5}$ mD (Deming, 1994). However, there are permeabilites that are low enough to contain anomalous pressures for the periods of time as stated by Deming, (1994). He conducted a study regarding the sealing characteristics of shale. He showed that the permeability and sealing properties were dependent on time and thickness (Figure 7.1). In a response paper, He and Corrigan, (1995) argued that the rock layer of a given thickness can maintain excess pressures at permeabilitites (for a given time period) and durations (for a given permeability) that are 1-2 orders of magnitude greater than concluded by Deming, (1994). It is quite uncertain to apply this plot for the study done here due to the erosion episodes that the basin experienced periodically. These generated erosion episodes interrupted the overpressure generation and build up process, thus it is difficult to estimate the time over which the overpressure is preserved. However, the selected base case permeability at surface (10 mD) resulted with the permeability of the seal rock at depth around $10^{-6}$ – $10^{-7}$ mD which corresponds to the Hurron and Marcellus shale shown in Figure 7.1.

Previous studies done by Katsube and Williamson, (1994, 1995) indicate that permeability decreases with burial depth from 10 mD – 10000 mD at the ocean floor surface to $10^{-7}$ – $10^{-4}$ mD at the depth of 2.5 – 4 km. The average depth of the Hekkingen Formation (seal rock) is near 2300 m which lies in this depth range, therefore the given constraints by Katsube and Williamson (1994, 1995), surface permeability of 10 Md (base case) have been applied in this study.

The study conducted by Neuzil (1994) about the permeability of the shales and suggested value of the shale permeability was between $10^{-8}$ mD and $10^{-2}$ mD. Duran et al, (2013) studied the basin development of the Hammerfest Basin in terms of the assessment of the petroleum generation, migration and leakage. They acquired a change of permeability for the seal rock through geological time. The modelled permeability is set to approximately $10^{-7}$ mD at present day for the Hekkingen and Fuglen Formations. Their modelling set up is supported by Linjordet and Olsen, (1992) in the study done for the Snøhvit field.

All the works supports the determined base case as the permeability of the shale closest to the reality to be used in the simulations and further studies.

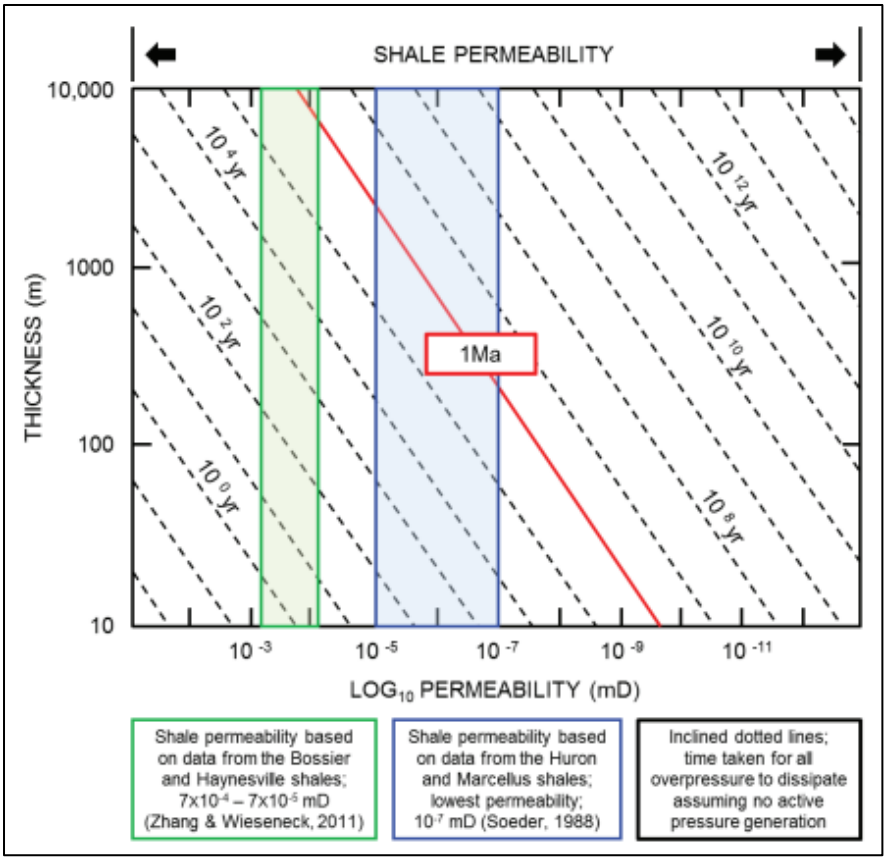


**Figure 7.1:** Pressure dissipation over geological time, dependent on shale thickness and permeability (Deming, 1994). Dotted lines and red arrow represent lines of geological time. Superimposed data are from Zhang and Wieseneck, (2011) from the Bossier and Haynesville shales and Marcellus and Huron shales ((Soeder, 1988); $10^{-7}$ mD, Huron and Marcellus shale) and Zhang and Wieseneck ((2011); 0.00007 – 0.0007 mD Bossier and Haynesville shale). The implication is that even at the low permeability present in these accumulations, pressure will revert to hydrostatic in 1 Ma ('geological time') unless gas generation and expansion occurs (or seals are very thick). He and Corrigan, (1995) state that the values by Deming, (1994) are 1-2 orders of magnitude too low in terms of maintaining excess pressures for a given time period. Given this, very thick seals are still required to maintain pressure over geological time of 1 Ma (red inclined line above) (O'Connor et al., 2014).

Permeability of the shale at the cap-rock level is one of the parameters that has been tested in Chapter 5.3 in the sensitivity analysis, but it has not been varied in the Monte-Carlo simulation. This is because permeability and standard deviation can only be described with $m^2$ for Monte-Carlo simulation and when permebilities in mD are converted into $m^2$, they turn out to be very small values, outside of the model accuracy. Hence it was not possible to set the permeability run in the Monte-Carlo simulation. The permeability exponent is varied instead and the permeability at the surface has been kept as constant value which is defined as the base case permeability**.**

## 7.3 Timing and magnitude of erosion and uplift

There exists large uncertainty to both the timing, the number and the amount of erosion episodes. In addition, methods known in the literature is also subjective when it comes to the quantification of uplift and erosion (Nyland et al., 1992). The two well-known methods to identify these variables are appetite fission track analysis (AFTA) and vitrinite reflectance data (VR). There are also other techniques of exhumation estimation known as sonic log and shot gathers. Both AFTA method and VR method can give the estimation of exhumation based on the determination of maximum paleotemperatures attained by an individual rock sample from a sedimentary unit. The comparison between the VR or AFTA and default thermal history constructed based on present day thermal regime and stratigraphic section helps to unravel the historical uplift processes. For example, if the AFTA data show a greater degree of fission track annealing, and/or if VR values are higher than predicted from the Default Thermal History, then the sampled unit has been hotter in the past (Green and Duddy, 2010). In this project work, the constraints in the timing of erosion episodes have been selected based on the study done by Green and Duddy, (2010). Eocene erosion coincide with the timing of the rift flank uplift in the Barents Sea (Dimakis et al., 1998; Zieba et al., 2014).The second erosion event shows that the entire north-western European margin was uplifted during the Late Miocene (Knies et al., 2009; Zieba et al., 2014). This view is supported by sedimentological and geochemical data from the Atlantic-Arctic gateway (Green and Duddy, 2010). The latest cooling event due to the glaciation is not modelled in this study since it does not coincide with the ages of the erosion detected by AFTA (Green and Duddy, 2010). Duran et al, (2013) noted in their paper that the deterioration of the climate in the northern hemisphere started at around 2.50 Ma, which resulted in regional glaciations (Jansen and Sjoholm, 1991; Vorren et al., 1991). There are also several other authors, such as Cavangh et al., (2006), Ostanin et al., (2017) supporting the idea that the glacial related erosion has happened only recently in the past 1-2 Ma.

The magnitude of erosion were acquired from the net erosion maps published by two different sources (Baig et al., 2016; Henriksen et al., 2011). Methodology of the maps are briefly explained in Chapter 4.4. As a base case, it is assumed that two erosion episodes occurred since Late Jurassic: Eocene erosion episode with 2/3 of net erosion; Miocene-Early Pliocene 1/3 of new erosion. Erosion maps that have been used in this study (Baig et al., 2016; Henriksen et al., 2011) are published as a net erosion maps during the geological time with no specific magnitude division

between the different erosion episodes. The most common knowledge is to divide the total maps with the ratio of 2:1 to determine the magnitude of Eocene and Late Miocene-Pliocene erosion episodes respectively. This method has been applied in the studies of Duran et al., (2013) However, several opposing ideas also exist to the given ratio above since there is no exact answer to this question of magnitudes. To account for this uncertainty, three burial history scenarios were tested in the Chapter 4.5. The Figure 7.2 and Table 7.1 below help to discuss the pressure calibration and fluid leakage results of these scenarios.

Figure 7.2 is used to see how good a match these burial history scenarios led to between the measured and simulated overpressure. A pressure calibration map for the base case with the ratio of 2:1 in two erosion magnitudes is already given in Figure 5.6a. The mean deviation is equal to 5.8 bar for that map. As can be seen from Figure 7.2 the least amount of deviation is observed once the ratio of the two erosion magnitudes is used with inverse values (1:2) by taking the second erosion event as the major one, which corresponds to the first scenario. The deviation value is even smaller in this case than the one given in the base case. However, the generally accepted scenario is the base case. The scenario E (4:1) shows the largest deviation among the three of them. Table 7.1 shows the deviation in each compartment depending on the burial history change. However, based on the study done by Green and Duddy, (2010), they suggested that the largest erosion in magnitude is the Eocene.

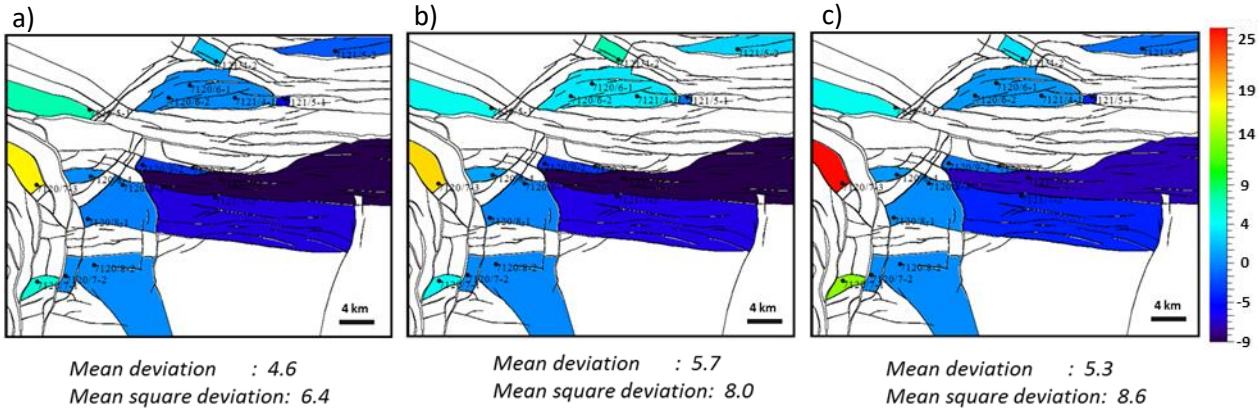


**Figure 7.2:** Pressure calibration maps between the modelled and measured pressure. (a) burial scenario D (ratio of 1:2) (b) burial scenario E (ration of 4:1) (c) burial scenario F (ration of 1:4).

## 7.4 Amount of leakage

Green and Duddy, (2010) showed that AFTA data and temperature estimate for the well 7120/9-2 indicate that the largest burial event is the first erosion episode (Figure 7.3).

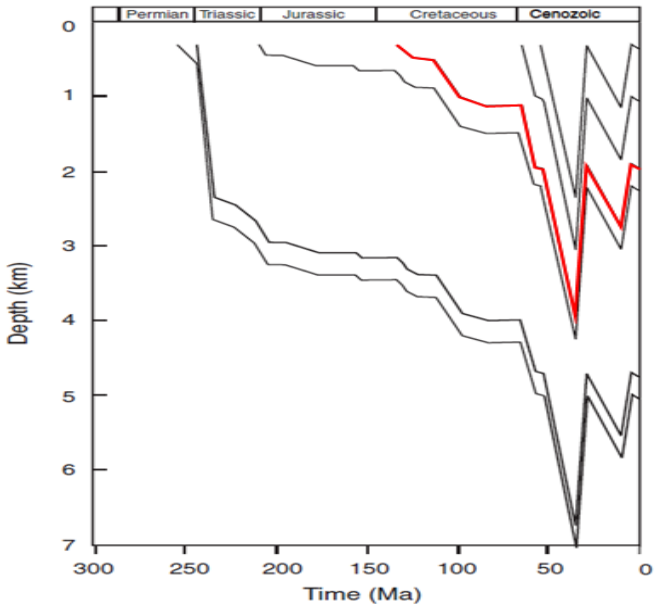


**Figure 7.3:** Integration of the paleothermal episodes with the preserved stratigraphic section results in reconstruction of the history of the post-Early Eocene burial and subsequent exhumation. Edited from Green and Duddy, (2010). Red colour signifies the burial history curve of the Stø Formation.

Figure 7.4 compare amount of leakage for some compartments for simulations where different burial history has been used. The timing of burial and uplift is kept constant, while the ratio has been varied using scenario E (4:1) and scenario F (1:4). Figure 7.4b shows that leakage started relatively late in the geological history in the scenario F. In both cases compartment 54 shows the least leakage and starts to leak the latest due to the influence of the nearby compartments 66 and 70.

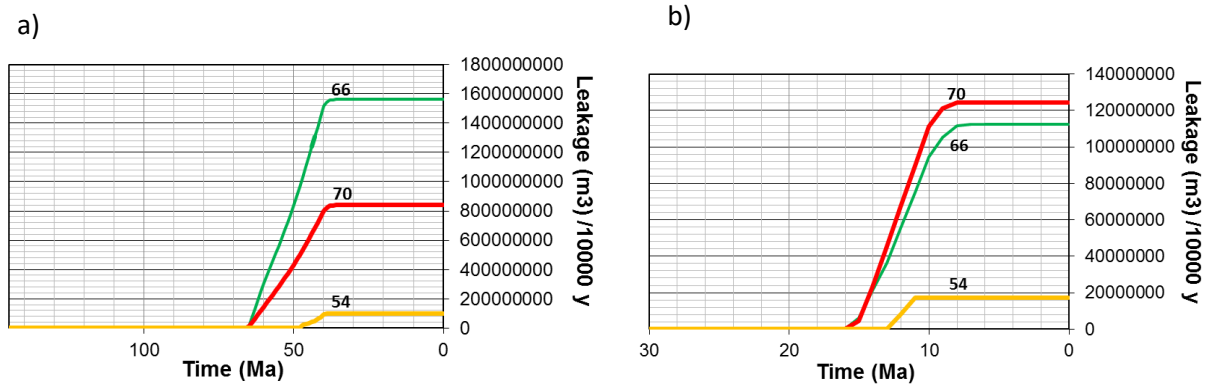


**Figure 7.4:** Comparison of the cumulative leakage ($m^3$) in each compartment for the two burial history scenarios (a) scenario E (4:1) (b) scenario F (1:4).

**Table 7.1:** Deviation in overpressure for each compartment in different scenarios. Wells used in the calibration study

| Wells used in the calibration study | Compartment name | Scenario D (1:2) | Scenario E (4:1) | Scenario F (1:4) |
|---|---|---|---|---|
| | | Deviation, bar | Deviation, bar | Deviation, bar |
| 7120/5-1 | 66 | 6.9 | 4.7 | 4.7 |
| 7120/6-1, 7120/6-2S, 7121/4-1 | 65 | 0 | 3.4 | 0.6 |
| 7120/7-1 | 10 | 5.7 | 4.7 | 13.6 |
| 7120/7-2 | 11 | 0.0 | 0.0 | 0.0 |
| 7120/7-3 | 44 | 17.8 | 18.8 | 26.8 |
| 7120/7-3, 7120/8-3 | 26 | -0.4 | -0.3 | 0.0 |
| 7120/8-2 | 12 | 0.0 | -0.2 | 0.0 |
| 7120/8-4 | 37 | 0.0 | 1.0 | 0.6 |
| 7120/9-1, 7120/9-2 | 41 | -3.0 | -3.1 | -0.7 |
| 7121/5-2 | 79 | 1.8 | 2.7 | 1.0 |
| 7121/7-2 | 35 | -6.4 | -6.3 | -3.9 |
| 7121/7-1 | 39 | -9.1 | -9.3 | -7.1 |
| 7121/4-2 | 78 | 1.9 | 7 | 3.1 |
| 7121/5-1 | 67 | -5.3 | -0.8 | -3.8 |
| Mean deviation | | 4.6 | 5.7 | 5.3 |

Figure 7.5 illustrates development of overpressure and leakage rate over geological time for the compartment 66 which is one of the commonly leaking compartments for the burial scenarios E (ration 4:1) and F (ration 1:4). Based on the observations done in the overpressure development trend of each of these compartments one can conclude that leakage started with the onset of overpressure for the scenario E whereas for the scenario F sudden pressure increase at around 30 Ma is not enough to initiate hydraulic failure (Figure 7.5). Thus, failure occurred sometime after the overpressure reached its highest value and stayed relatively stable. Compartment 70 also experienced the similar trends to compartment 66 both in overpressure and leakage rate whereas there is a change in the modelling results for the compartment 54 in both scenarios (Figure 7.6). This could be explained with the influence of compartments on each other again. This could be

due to the overpressure generation trend. Figure 7.6b shows that overpressure reaches higher value (120 bar) in its second peak and suddenly drops which is not the case in Figure 7.6a where maximum overpressure is observed around 100 bar and stayed at the same level for a longer time. The leakage in compartment 54 initiated in the scenario F (1:4) for the high overpressure case and with the drop of overpressure it stopped leaking immediately.

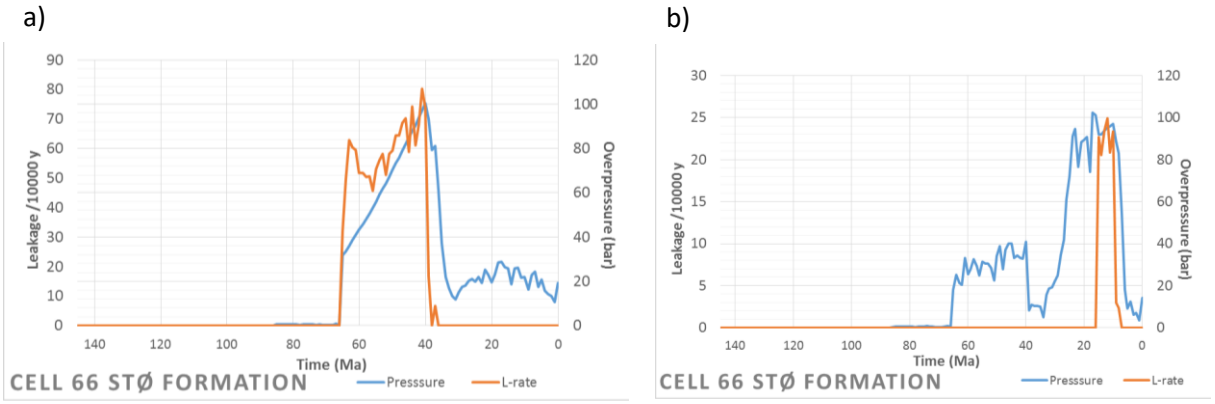


**Figure 7.5:** The change of overpressure and leakage rate ($m^3$/10000y) over 145 – 0 Ma for the compartment 66 which is one of the leaking compartments in both (a) scenario E (4:1) (b) scenario F (1:4).

In addition, there is at least ten times difference in leakage rate in favour of the scenario E for all the compartments. Leakage rate decreased at least four time from the scenario E to scenario F for the compartment 66. However, it slightly increased between two scenarios for the compartment 54. There is an obvious correlation between the rate of leakage and the corresponding time interval that the leakage occurs (Figure 7.5 and Figure 7.6).

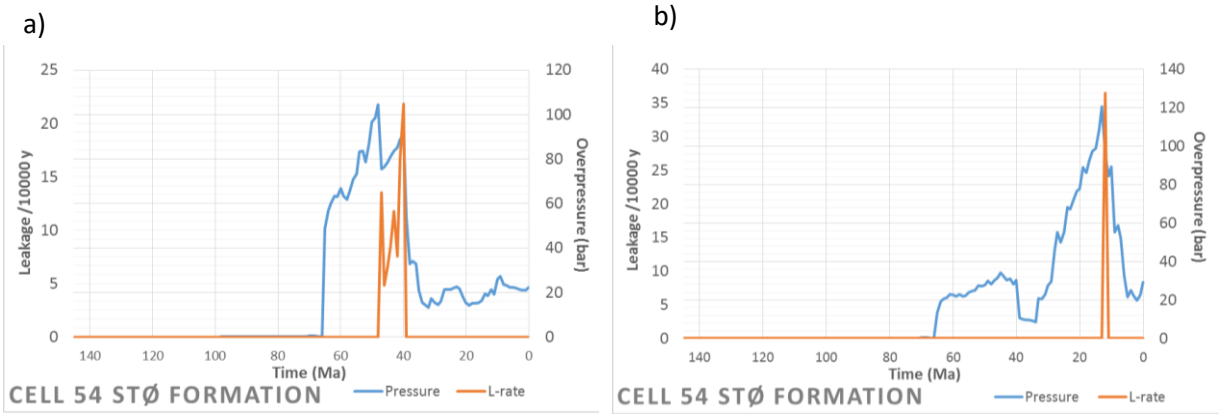


**Figure 7.6:** The changes of overpressure and leakage rate ($m^3$/10000y) over 145 – 0 Ma for the compartment 54 which is one of the leaking compartments in both (a) scenario E (4:1) (b) scenario F (1:4).

## 7.5 Comparison between the modelled and observed leakage

Several modelled leakage maps as part of this study, show that leakage from the pressure compartments depend on the burial history and input parameters. Ostanin et al., (2017) models hydrocarbon breakthrough zones near faults that are leaking gas and oil. In order to compare the leaking zone in Ostanin et al's, (2017) study and the one performed here, Figure 7.7 is built to show the approximate locations of leakage zones with green starts adapted from their leakage map illustrated in Figure 7.8. Modelled leakage map on the background in the Figure 7.8 belongs to the base scenarios that is described in Chapter 5.1.

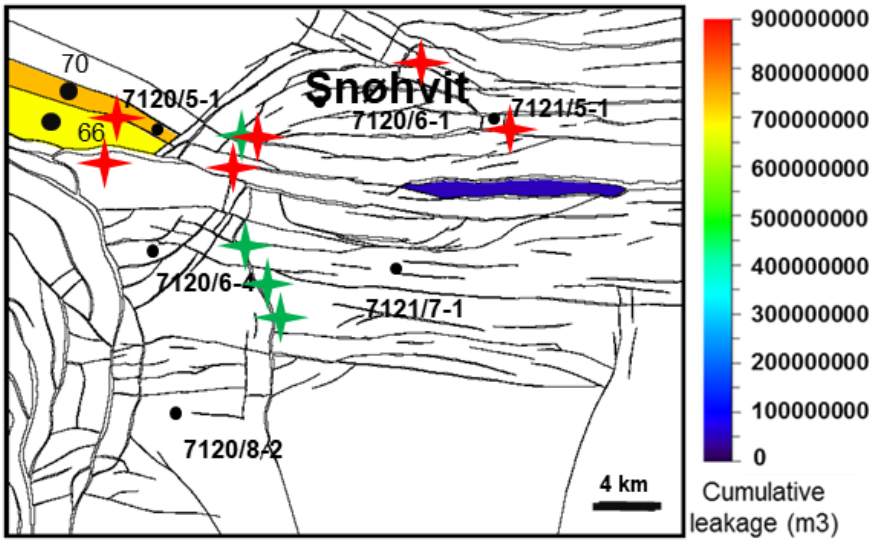


**Figure 7.7:** Base case modelled cumulative leakage map and superimposed leakage zones based on Ostanin et al., (2017) (green star) and Vadakkepuliyambatta et al., (2013) (red star) studies.

Vadakkepuliyambatta et al, (2013) mapped the distribution of the fluid-flow systems in the Southern-Barents Sea from 2D seismic. They were able to map the location of the gas chimneys as a fluid-flow feature. It is shown from Figure 7.9, that the gas chimneys are present close to the Snøhvit reservoir. It is also stated in the paper that many of these chimneys were located above major fault in the study area. In Figure 7.7 red stars help to compare the leakage zones between the study done here and the one by Vadakkepuliyambatta et al., (2013). This figure shows that the only common leaking zone with Vadakkepuliyambatta et al, (2013), is located west of the Snøhvit field, close to the modelled well 7120/5-1. The modelled base case leakage map and the two maps taken from literature shows that there are less leaking compartments in the study area compared to the non-leaking ones in general.

However, there are several uncertainties that need to account for before making any direct comparisons. First of all, in the leakage map of Vadakkepuliyambatta et al, (2013), the source of leakage is presented as several different formations. However, the leakage in this study is only limited to the Stø reservoir unit.

Both Ostanin et al., (2017) and Vadakkepuliyambatta et al., (2013) leakage maps illustrates the hydrocarbon breakthrough locations. The study done here assumes only water fluid in the basin, without taking hydrocarbon into consideration. But hydrocarbon leakage is expected to be sensitive to hydraulic fracturing and water fluid leakage in an overpressure area. It is important to note that hydrocarbon fill history is also time-dependent and relies on the overpressure, charge, trapping, hydraulic fracturing and leakage histories (Lothe, 2004).

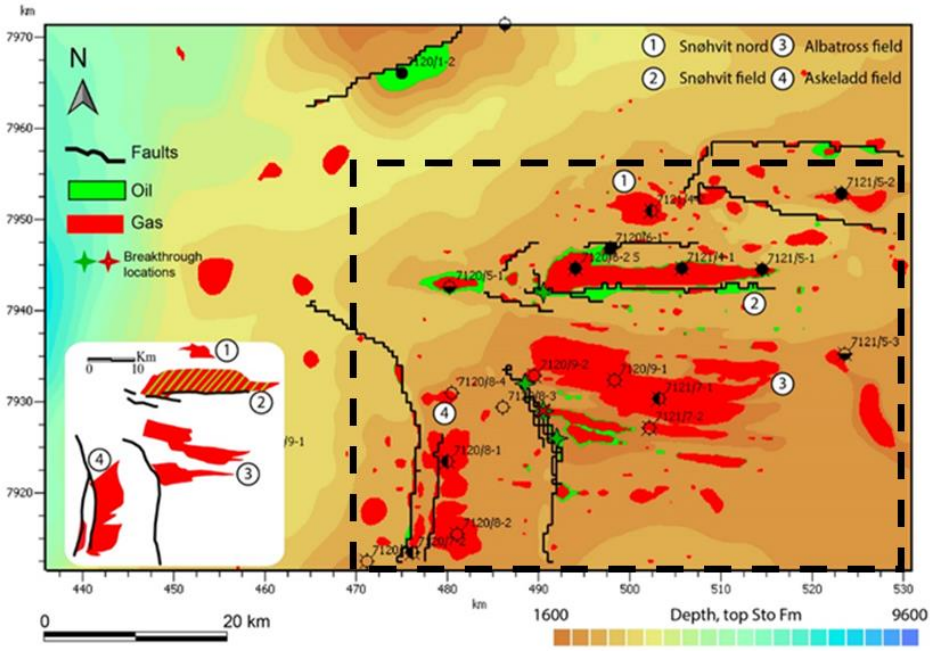


**Figure 7.8:** Modelled accumulations based on 3D petroleum system modelling showing the main Snøhvit, Albatross and Askeladd reservoirs, as well as associated oil and gas phases. Input fault traces are also shown, as well as petroleum break-through locations, on maximum hydrocarbon (HC) column height, reservoir structure and sealing capacity. The insert (bottom left) shows the location and outlines of discoveries and producing fields in the Hammerfest Basin. Dotted black box shows the study area.

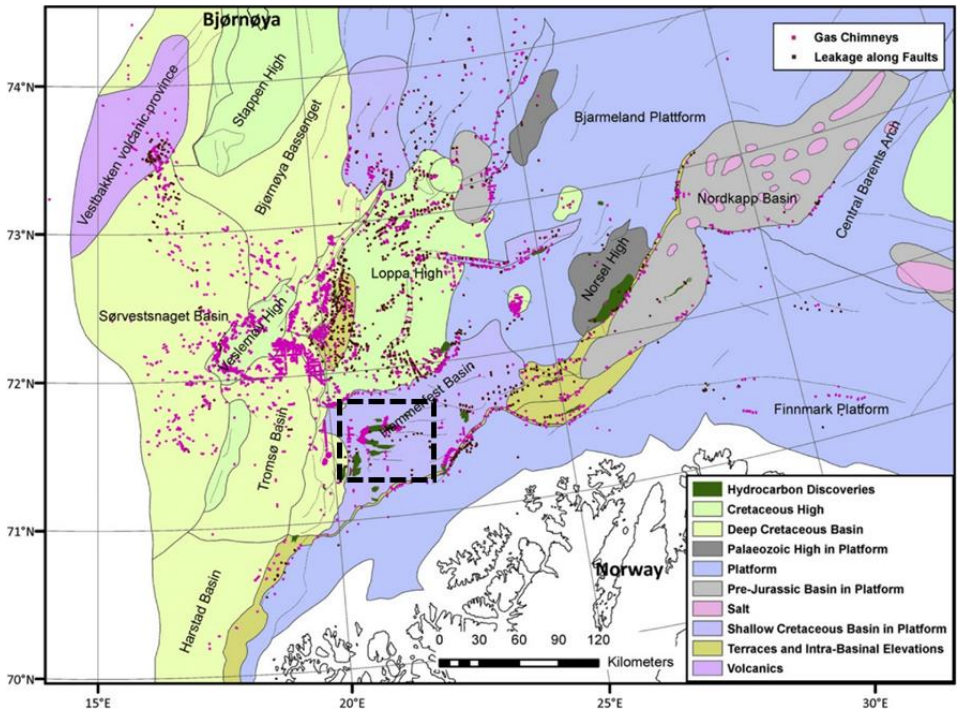


**Figure 7.9:** Map showing the distribution of gas chimneys and leakage along faults in the SW Barents Sea. The black lines are the major fault boundaries. Most of the features were located right on top of major faults in the area. Dotted black box shows the study area.

# 8. Conclusion and further work

- The overpressure distribution map and leakage maps were modelled for nine different time steps in the geological history, the last time step being the present day. The results have been calibrated with the observed pressure from the wells drilled in the study area. Generally, most of the modelled overpressure maps showed quite low mean deviation +/- 6 bar
- The overpressure maps show low overpressure at present day and most of the basin, excluding the northern and western part, is dominated by a hydrostatic pressure regime. The modelling showed that there have been hydraulic fracturing and leakage in several compartments in the past, whereas there is no leakage detected at present day. The leakage mainly took place before the uplift/erosion episodes.
- The magnitude of the input minimum horizontal stress (Grauls 1998) versus depth, were varied. The minimum horizontal stress curve was calibrated with the Leak Off Test data coming from the wells drilled in the study area. The best results of the pressure modelling are acquired using Grauls number in the range of 1.14-1.15 e.g. extensional stress regime.
- Three different permeability models were created to describe the shale permeability at the cap-rock level. The results showed that when the permeability is low (tight rocks) more compartments initiates failure and leakage occurs.
- Two alternative erosion scenarios (Baig et al., 2016; Henriksen et al., 2011) were used in the modelling. When pressure calibration maps were compared, the Henriksen et al, (2011) erosion scenario resulted with in less mean deviation, compared to the scenario that Baig et al. (2016) was used. Overall, using Baig net erosion map resulted in leakage from more compartments.
- There are four different burial history scenarios modelled in this study, the first one being the base case, signifying the ratio between the two-erosion events as 2:1. Changing this scenario influenced largely the leakage maps by changing the number of the leaking compartments for every scenario used.
- Overall there are less leaking compartments compared to the non-leaking ones in all the case studies. Two compartments (66 and 70) on the north-west of the study area showed leakage in most of the tested scenarios.
- Monte-Carlo simulation is performed with a total number of 552 runs. Permeability exponent and Grauls number were tested. Misfit analysis done for both of the parameters and the best-

case scenario is identified giving the least deviation. This best-case scenario is very similar to the one identified as result of single run simulations.

- By using 552 simulations, the most probable pore pressure, lithostatic pressure and hydrostatic pressure is modelled along the well (vertically) for the selected Snøhvit compartment and the results showed very small overpressure build-up along the depth. Probability distribution of overpressure for the present day showed that, current dominant pressure for this compartment is 11.5 bar.

## 8.1 Further work

The methods used here can be applied to other basins to model overpressure build up over geological time scale, and possible hydraulic fracturing and leakage. In high overpressured basins such pressure prognosis along the well can be used for:

- Borehole stability evaluation
- Mud weight optimization
- Avoiding drilling hazards
- Optimized well placement

The fluid pressure distribution in a carrier or reservoir rock can influence the secondary migration of petroleum in a sedimentary basin. Good estimates of present fluid pressure in yet undrilled prospects are highly relevant for planning safe well layouts and drilling procedures. Modelling of the fluid pressure distribution over geological periods of time and up to recent can therefore contribute to reduce exploration and technical risks.

# 9. References

Addis, M., Hanssen, T., Yassir, N., Willoughby, D., Enever, J., 1998. A comparison of leak-off test and extended leak-off test data for stress estimation. Presented at the SPE/ISRM Rock Mechanics in Petroleum Engineering, Society of Petroleum Engineers.

Anderson, E.M., 1951. The dynamics of faulting and dyke formation with applications to Britain. Hafner Pub. Co.

Athy, L.F., 1930. Density, porosity, and compaction of sedimentary rocks. AAPG Bull. 14, 1–24.

Baig, I., Faleide, J.I., Jahren, J., Mondol, N.H., 2016. Cenozoic exhumation on the southwestern Barents Shelf: Estimates and uncertainties constrained from compaction and thermal maturity analyses. Mar. Pet. Geol. 73, 105–130.

Baldwin, B., Butler, C.O., 1985. Compaction curves. AAPG Bull. 69, 622–626.

Bell, J., 1990. Investigating stress regimes in sedimentary basins using information from oil industry wireline logs and drilling records. Geol. Soc. Lond. Spec. Publ. 48, 305–325.

Berglund, L., Augustson, J., Færseth, R., Gjelberg, J., Ramberg-Moe, H., 1986. The evolution of the Hammerfest Basin. Habitat Hydrocarb. Nor. Cont. Shelf 319–338.

Bjørkum, P.A., Oelkers, E.H., Nadeau, P.H., Walderhaug, O., Murphy, W.M., 1998. Porosity prediction in quartzose sandstones as a function of time, temperature, depth, stylolite frequency, and hydrocarbon saturation. AAPG Bull. 82, 637–648.

Bjørlykke, K., 1999. Principal aspects of compaction and fluid flow in mudstones. Geol. Soc. Lond. Spec. Publ. 158, 73–78.

Bjørlykke, K., Høeg, K., 1997. Effects of burial diagenesis on stresses, compaction and fluid flow in sedimentary basins. Mar. Pet. Geol. 14, 267–276.

Bjørlykke, K., Jahren, J., 2010. Sandstones and sandstone reservoirs. Springer.

Bolås, H.M.N., Hermanrud, C., 2003. Hydrocarbon leakage processes and trap retention capacities offshore Norway. Pet. Geosci. 9, 321–332.

Borge, H., 2002. Modelling generation and dissipation of overpressure in sedimentary basins: an example from the Halten Terrace, offshore Norway. Mar. Pet. Geol. 19, 377–388.

Borge, H., 2000. Fault controlled pressure modelling in sedimentary basins.

Borge, H., Sylta, Ø., 1998. 3D modelling of fault bounded pressure compartments in the North Viking Graben. Energy Explor. Exploit. 16, 301–323.

Caine, J.S., Evans, J.P., Forster, C.B., 1996. Fault zone architecture and permeability structure. Geology 24, 1025–1028.

Cavanagh, A.J., Di Primio, R., Scheck-Wenderoth, M., Horsfield, B., 2006. Severity and timing of Cenozoic exhumation in the southwestern Barents Sea. J. Geol. Soc. 163, 761–774.

Clark, S.A., Faleide, J.I., Hauser, J., Ritzmann, O., Mjelde, R., Ebbing, J., Thybo, H., Flüh, E., 2013. Stochastic velocity inversion of seismic reflection/refraction traveltime data for rift structure of the southwest Barents Sea. Tectonophysics 593, 135–150.

Cloetingh, S., Gradstein, F., Kooi, H., Grant, A., Kaminski, M., 1990. Plate reorganization: a cause of rapid late Neogene subsidence and sedimentation around the North Atlantic? J. Geol. Soc. 147, 495–506.

Dalland, A., Worsley, D., Ofstad, K., 1988. A Lithostratigraphic Scheme for the Mesozoic and Cenozoic and Succession Offshore Mid-and Northern Norway. Oljedirektoratet.

Deming, D., 1994. Factors necessary to define a pressure seal. AAPG Bull. 78, 1005–1009.

Dengo, C., Røssland, K., 2013. Extensional tectonic history of the western Barents Sea.

Dimakis, P., Braathen, B.I., Faleide, J.I., Elverhøi, A., Gudlaugsson, S.T., 1998. Cenozoic erosion and the preglacial uplift of the Svalbard–Barents Sea region. Tectonophysics 300, 311–327.

Doré, A., Jensen, L., 1996. The impact of late Cenozoic uplift and erosion on hydrocarbon exploration: offshore Norway and some other uplifted basins. Glob. Planet. Change 12, 415–436.

Duran, E.R., di Primio, R., Anka, Z., Stoddart, D., Horsfield, B., 2013. 3D-basin modelling of the Hammerfest Basin (southwestern Barents Sea): A quantitative assessment of petroleum generation, migration and leakage. Mar. Pet. Geol. 45, 281–303.

Faleide, J.I., Tsikalas, F., Breivik, A.J., Mjelde, R., Ritzmann, O., Engen, O., Wilson, J., Eldholm, O., 2008. Structure and evolution of the continental margin off Norway and the Barents Sea. Episodes 31, 82–91.

Faleide, J.I., Vågnes, E., Gudlaugsson, S.T., 1993. Late Mesozoic-Cenozoic evolution of the south-western Barents Sea in a regional rift-shear tectonic setting. Mar. Pet. Geol. 10, 186–214.

Fejerskov, M., Lindholm, C., 2000. Crustal stress in and around Norway: an evaluation of stress-generating mechanisms. Geol. Soc. Lond. Spec. Publ. 167, 451–467.

Gabrielsen, R., Færseth, R.B., 1989. The inner shelf of North Cape, Norway and its implications for the Barents Shelf-Finnmark Caledonide boundary. A comment. Nor. Geol. Tidsskr. 69, 57–62.

Gabrielsen, R.H., Faerseth, R.B., Jensen, L.N., 1990. Structural Elements of the Norwegian Continental Shelf. Pt. 1. The Barents Sea Region. Norwegian Petroleum Directorate.

Gabrielsen, R.H., Grunnaleite, I., Rasmussen, E., 1997. Cretaceous and tertiary inversion in the Bjørnøyrenna Fault Complex, south-western Barents Sea. Mar. Pet. Geol. 14, 165–178.

Ghazi, S., 1992. Cenozoic uplift in the Stord Basin area and its consequences for exploration. Nor. Geol. Tidsskr. 72, 285–290.

Giles, M., Indrelid, S., James, D., 1998. Compaction—the great unknown in basin modelling. Geol. Soc. Lond. Spec. Publ. 141, 15–43.

Gradstein, F.M., Ogg, J.G., Smith, A.G., Bleeker, W., Lourens, L.J., 2004. A new geologic time scale, with special reference to Precambrian and Neogene. Episodes 27, 83–100.

Grauls, D., 1999. Overpressures: causal mechanisms, conventional and hydromechanical approaches. Oil Gas Sci. Technol. 54, 667–678.

Grauls, D., 1998. Overpressure assessment using a minimum principal stress approach. Presented at the Overpressures in petroleum exploration; Proc. Workshop: Bull. Centre Rech. Elf Explor. Prod., Pau, France.

Green, P., Duddy, I., 2010. Synchronous exhumation events around the Arctic including examples from Barents Sea and Alaska North Slope. Presented at the Geological Society, London, Petroleum Geology Conference series, Geological Society of London, pp. 633–644.

Halland, E.K., Muljezinovic, J., Riis, F., 2013. CO2 storage atlas Barents Sea. Nor. Pet. Dir.

Hantschel, T., Kauerauf, A.I., 2009. Fundamentals of basin and petroleum systems modeling. Springer Science & Business Media.

He, Z., Corrigan, J., 1995. Factors necessary to define a pressure seal: discussion. AAPG Bull. 79, 1075–1078.

Hendriks, B.W., Andriessen, P.A., 2002. Pattern and timing of the post-Caledonian denudation of northern Scandinavia constrained by apatite fission-track thermochronology. Geol. Soc. Lond. Spec. Publ. 196, 117–137.

Henriksen, E., Bjørnseth, H., Hals, T., Heide, T., Kiryukhina, T., Kløvjan, O., Larssen, G., Ryseth, A., Rønning, K., Sollid, K., 2011. Uplift and erosion of the greater Barents Sea: impact on prospectivity and petroleum systems. Geol. Soc. Lond. Mem. 35, 271–281.

Jakobsson, M., Macnab, R., Mayer, L., Anderson, R., Edwards, M., Hatzky, J., Schenke, H.W., Johnson, P., 2008. An improved bathymetric portrayal of the Arctic Ocean: Implications for ocean modeling and geological, geophysical and oceanographic analyses. Geophys. Res. Lett. 35.

Jansen, E., Sjoholm, J., 1991. Reconstruction of glaciation over the past 6 Myr from ice-borne deposits in the Norwegian Sea. Nature 349, 600.

Jensen, L., Schmidt, B., 1993. Neogene uplift and erosion offshore south Norway: magnitude and consequences for hydrocarbon exploration in the Farsund Basin, in: Generation, Accumulation and Production of Europe's Hydrocarbons III. Springer, pp. 79–88.

Katsube, T., Williamson, M., 1995. Critical depth of burial of subsiding shales and its effect on abnormal pressure development. Presented at the Proceedings of the Oil and Gas Forum, pp. 283–286.

Katsube, T., Williamson, M., 1994. Effects of diagenesis on shale nano-pore structure and implications for sealing capacity. Clay Miner. 29, 451–472.

Knies, J., Matthiessen, J., Vogt, C., Laberg, J.S., Hjelstuen, B.O., Smelror, M., Larsen, E., Andreassen, K., Eidvin, T., Vorren, T.O., 2009. The Plio-Pleistocene glaciation of the Barents Sea–Svalbard region: a new model based on revised chronostratigraphy. Quat. Sci. Rev. 28, 812–829.

Linjordet, A., Olsen, R.G., 1992. The Jurassic Snohvit Gas Field, Hammerfest Basin, Offshore Northern Norway: Chapter 22.

Lothe, A., 2004. Simulations of hydraulic fracturing and leakage in sedimentary basins. Univ. Bergen.

Lothe, A.E., Tømmerås, A., Helset, H.M., 2008. Clay smear (SGR) along faults and the implications on water flow and fluid overpressures. Presented at the AAPG Conference, Cape Town.

Lothe, M., Helset, H.M., Hovland, S., 2009. New integrated approach for updating pore-pressure predictions during drilling. Presented at the SPE Annual Technical Conference and Exhibition, Society of Petroleum Engineers.

Luo, X., Vasseur, G., 1992. Contributions of Compaction and Aquathermal Pressuring to Geopressure and the Influence of Environmental Conditions (1). AAPG Bull. 76, 1550–1559.

Magoon, L.B., Dow, W.G., 1994. The Petroleum System: Chapter 1: Part I. Introduction.

Nadeau, P., 2011. Earth's energy "Golden Zone": a synthesis from mineralogical research. Clay Miner. 46, 1–24.

Neuzil, C., 1994. How permeable are clays and shales? Water Resour. Res. 30, 145–150.

Nøttvedt, A., Cecchi, M., Gjelberg, J., Kristensen, S., Rasmussen, A., 1993. Svalbard-Barents Sea correlation: a short review.

Nyland, B., Jensen, L., Skagen, J., Skarpnes, O., Vorren, T., 1992. Tertiary uplift and erosion in the Barents Sea: magnitude, timing and consequences.

O'Connor, S., Mildren, S., Kemper, M., Malaver, C., Gallop, J., Green, S., 2014. Optimising resource plays–an integrated "GeoPrediction" approach.

Ohm, S.E., Karlsen, D.A., Austin, T., 2008. Geochemically driven exploration models in uplifted areas: Examples from the Norwegian Barents Sea. AAPG Bull. 92, 1191–1223.

Okland, D., Gabrielsen, G.K., Gjerde, J., Koen, S., Williams, E.L., 2002. The importance of extended leak-off test data for combatting lost circulation. Presented at the SPE/ISRM Rock Mechanics Conference, Society of Petroleum Engineers.

Osborne, M.J., Swarbrick, R.E., 1997. Mechanisms for generating overpressure in sedimentary basins: a reevaluation. AAPG Bull. 81, 1023–1041.

Ostanin, I., Anka, Z., di Primio, R., 2017. Role of Faults in Hydrocarbon Leakage in the Hammerfest Basin, SW Barents Sea: Insights from Seismic Data and Numerical Modelling. Geosciences 7, 28.

Ostanin, I., Anka, Z., di Primio, R., Bernal, A., 2012. Identification of a large Upper Cretaceous polygonal fault network in the Hammerfest basin: Implications on the reactivation of regional faulting and gas leakage dynamics, SW Barents Sea. Mar. Geol. 332, 109–125.

Reemst, P., Cloetingh, S., Fanavoll, S., 1994. Tectonostratigraphic modelling of Cenozoic uplift and erosion in the south-western Barents Sea. Mar. Pet. Geol. 11, 478–490.

Riis, F., Fjeldskaar, W., 1992. On the magnitude of the Late Tertiary and Quaternary erosion and its significance for the uplift of Scandinavia and the Barents Sea. Struct. Tecton. Model. Its Appl. Pet. Geol. 1, 163–185.

Ryseth, A., Augustson, J.H., Charnock, M., Haugerud, O., Knutsen, S.-M., Midbøe, P.S., Opsal, J.G., Sundsbø, G., 2003. Cenozoic stratigraphy and evolution of the Sørvestsnaget Basin, southwestern Barents Sea. Nor. J. Geol. Geol. Foren. 83.

Sales, J., 1992. Uplift and subsidence do northwestern Europe: possible causes and influence on hydrocarbon productivity. Nor. Geol. Tidsskr. 72, 253–258.

Sclater, J.G., Christie, P., 1980. Continental stretching; an explanation of the post-Mid-Cretaceous subsidence of the central North Sea basin. J. Geophys. Res. 85, 3711–3739.

Skogseid, J., Planke, S., Faleide, J.I., Pedersen, T., Eldholm, O., Neverdal, F., 2000. NE Atlantic continental rifting and volcanic margin formation. Geol. Soc. Lond. Spec. Publ. 167, 295–326.

Soeder, D.J., 1988. Porosity and permeability of eastern Devonian gas shale. SPE Form. Eval. 3, 116–124.

Sund, T., Skarpnes, O., Jensen, L.N., Larsen, R., 1986. Tectonic development and hydrocarbon potential offshore Troms, northern Norway.

Swarbrick, R., Osborne, M., Yardley, G., 2002. The magnitude of overpressure from generating mechanisms under realistic basin conditions. AAPG Mem. 76, 1–12.

Swarbrick, R.E., Osborne, M.J., Yardley, G.S., 2001. AAPG Memoir 76, Chapter 1: Comparision of Overpressure Magnitude Resulting from the Main Generating Mechanisms.

Swarbrick, R.E., Schneider, F., 1999. Introduction to special issue on overpressure research. Mar. Pet. Geol. 16, 301–302.

Sylta, Ø., Krokstad, W., 2003. Estimation of oil and gas column heights in prospects using probabilistic basin modelling methods. Pet. Geosci. 9, 243–254.

Talleraas, E., 1979. The Hammerfest basin—an aulacogen. Presented at the Norwegian Sea Symposium, Norwegian Petroleum Society, Tromso, pp. 1–13.

Terzaghi, K. von, 1923. Die berechnung der durchlassigkeitsziffer des tones aus dem verlauf der hydrodynamischen spannungserscheinungen. Sitzungsberichte Akad. Wiss. Wien Math.-Naturwissenschaftliche Kl. Abt. IIa 132, 125–138.

Torske, T., 1972. Tertiary oblique uplift of Western Fennoscandia; crustal warping in connection with rifting and break-up of the Laurasian continent. Nor. Geol. Unders. Bull. 273, 43–48.

Vadakkepuliyambatta, S., Bünz, S., Mienert, J., Chand, S., 2013. Distribution of subsurface fluid-flow systems in the SW Barents Sea. Mar. Pet. Geol. 43, 208–221.

Vorren, T.O., Richardsen, G., Knutsen, S.-M., Henriksen, E., 1991. Cenozoic erosion and sedimentation in the western Barents Sea. Mar. Pet. Geol. 8, 317–340.

Walderhaug, O., 1996. Kinetic modeling of quartz cementation and porosity loss in deeply buried sandstone reservoirs. AAPG Bull. 80, 731–745.

Walderhaug, O., 1994. Precipitation rates for quartz cement in sandstones determined by fluid-inclusion microthermometry and temperature-history modeling. J. Sediment. Res. 64.

Walderhaug, O., Bjørkum, P.A., 2003. The effect of stylolite spacing on quartz cementation in the Lower Jurassic Stø Formation, southern Barents Sea. J. Sediment. Res. 73, 146–156.

Wangen, M., 2001. A quantitative comparison of some mechanisms generating overpressure in sedimentary basins. Tectonophysics 334, 211–234.

Wangen, M., 2000. Generation of overpressure by cementation of pore space in sedimentary rocks. Geophys. J. Int. 143, 608–620.

Waples, D., 1998. Basin modelling: how well have we done? Geol. Soc. Lond. Spec. Publ. 141, 1–14.

White, A.J., Traugott, M.O., Swarbrick, R.E., 2002. The use of leak-off tests as means of predicting minimum in-situ stress. Pet. Geosci. 8, 189–193.

Worden, R., Morad, S., 2000. Quartz cementation in oil field sandstones: a review of the key controversies.

Worsley, D., 2008. The post-Caledonian development of Svalbard and the western Barents Sea. Polar Res. 27, 298–317.

Yang, Y., Aplin, A.C., 2010. A permeability–porosity relationship for mudstones. Mar. Pet. Geol. 27, 1692–1697.

Yassir, N., Addis, M.A., 2002. Relationships between pore pressure and stress in different tectonic settings.

Zhang, J., 2011. Pore pressure prediction from well logs: Methods, modifications, and new approaches. Earth-Sci. Rev. 108, 50–63.

Zhang, J., Wieseneck, J., 2011. Challenges and surprises of abnormal pore pressures in the shale gas formations. Presented at the SPE Annual Technical Conference and Exhibition, Society of Petroleum Engineers.

Zieba, K.J., Daszinnies, M., Emmel, B., Lothe, A., Grøver, A., Lippard, S., 2014. Assessment of the Cenozoic Erosion Amount Using Monte Carlo Type-Petroleum Systems Modeling of the Hammerfest Basin, Western Barents Sea. Am. J. Geosci. 4, 40–53.

Zoback, M.D., 2010. Reservoir geomechanics. Cambridge University Press.

# Appendix A

Values of parameters used in the Pressim 2D model (Borge, 2000) for explanation of parameters and nomenclature)

| Description | Symbol | Value | Unit |
|---|---|---|---|
| **Pressure generation and accumulation** | | | |
| Accumulating depth | zA | 1000 | m |
| Generating depth | zS | 4000.0 | m |
| Salinity | s | 50 000 | ppm |
| Accumulating exponent | A | 1 | |
| Shale drainage thickness | Y | 250.0 | m |
| Minimum reservoir thickness | zmin | 20 | m |
| Minimum net/gross ratio | N/Gmin | 0.080 | |
| Maximum shale compaction depth | zshale | 10 000.0 | m |
| Hydrostatic gradient | ρwg | 0.1030 | bar m1 bar |
| Lithostatic gradient | ρ¯g | 0.226 | m1 |
| Time step | Δt | 10 000 | years |
| Diameter of quartz grain size | D | 0.0003 | m |
| Fraction of detrital quartz | f | 0.65 | |
| Molar mass of quartz | M | 0.06009 | kg mole1 |
| Density of quartz | ρ quartz | 2650.0 | kg⋅m3 |
| Temperature at which quartz cementation starts | TC0 | 80.0 | C |
| Temperature at which quartz cementation is completed | TC1 | 175.0 | C |
| Quartz precipitation rate factor | r1 | 1.98e-018 | mole/m2s |
| Quartz precipitation rate exponent | r2 | 0.022 | C1 |
| Sand porosity at seabed | φS0 | 0.45 | |
| Sand porosity constant 1 | η1 | 2400 | m |
| Sand porosity constant 2 | η2 | 0.50 | |
| Temperature at seabed | ∂T/∂z | 4.0 | C C |
| Temperature gradient | | 0.035 | m1 |
| Irreducible water saturation (Stø Formation) | φC1 | 0.020 | |
| Clay coating factor (Stø Formation) | C | 0.20 | |
| Minimum dissipation volume | Vmin | 1.0e+006 | m3 |
| **Hydraulic leakage** | | | |
| Poisson's ratio (shales) at surface | Vz0 | 800 | |
| Poisson's ratio (shales) at accumulating depth | VzA | 38 000 | |
| Poisson's ratio (shales) at sealing depth | VzS | 60 000 | |
| Poisson's ratio (shales) at max. shale comp. depth | Vzshale | 117 000 | |
| Young's modulus (shales) at surface | Ez0 | 800 | bar |
| Young's modulus (shales) at accumulating depth | EzA | 38 000 | bar |
| Young's modulus (shales) at sealing depth | EzS | 60 000 | bar |
| Young's modulus (shales) at max. shale comp. depth | EzshaleT | 117 000 | bar |
| Coefficient of thermal expansion | αT | 1.00e-005 | |

| | | | |
|---|---|---|---|
| Bulk modulus (shale) (bar) | $K_s$ | 170000.0 | bar |
| Coefficient of internal friction | $\mu$ | 0.6 | |
| Coefficient of sliding friction | $\mu$ | 0.7 | |
| **Lateral transmissibility** | | | |
| Lateral transmissibility | | 0.00069 | |
| Percent transmissibility remaining at no overlap | p | 0.05 | |
| Width of fault blocks | b | 20.0 | m |
| Porosity at seabed | $\varphi_0$ | 0.449 | |
| Rate of change in porosity versus depth | | 0.00039 | m1 |
| Porosity where the *K* curve changes between deep and shallow relationships | $\varphi b$ | 0.1 | |
| Permeability where the *K* curve changes between deep and shallow relationships | Kb | 9.99999997e-0077.0 | mD mD m1 mD |
| Rate of change in fault zone permeability (log) versus depth (log) for shallow faults | $\delta sh$ | 5.0 | m1 |
| Rate of change in fault zone permeability (log) versus depth (log) for deep faults | $\delta de$ | 6.0 | |